POLYTECHNIQUE MONTRÉAL

affiliée à l'Université de Montréal

Accurate and efficient simulation of electromagnetic transients using frequency dependent line and cable models

MIGUEL CERVANTES MARTINEZ

Département de génie électrique

Thèse présentée en vue de l'obtention du diplôme de *Philosophiæ Doctor*

Génie électrique

Août 2019

POLYTECHNIQUE MONTRÉAL

affiliée à l'Université de Montréal

Cette thèse intitulée:

Accurate and efficient simulation of electromagnetic transients using frequency dependent line and cable models

présentée par **Miguel CERVANTES MARTINEZ**

en vue de l'obtention du diplôme de *Philosophiæ Doctor*

a été dûment acceptée par le jury d'examen constitué de :

Houshang KARIMI, président
Ilhan KOCAR, membre et directeur de recherche
Jean MAHSEREDJIAN, membre et codirecteur de recherche
Abner RAMIREZ VASQUEZ, membre et codirecteur de recherche
Keyhan SHESHYEKANI, membre
Geneviève LIETZ, membre externe

DEDICATION

To my wife and my family

ACKNOWLEDGEMENTS

My best acknowledgments and gratefulness to…

- My co-supervisor Dr. Jean Mahseredjian for giving me the opportunity to pursue this PhD project and the continuous support

- My supervisor Dr. Ilhan Kocar for the proper advice, support and discussions

- My co-supervisor, Dr. Abner, who made the contact that allowed me to come to Montreal for this PhD, and who continued to support me despite the distance

- To Dr. Akihiro Ametani for his valuable advices, his friendship, and all the coffee breaks

- My friends and colleagues from the department: Isabel, Baki, Fidji, Thomas, Haoyan, Masashi, Ming, Anton, Jesus, Reza, Aramis, David, Diane. Also, to all the people who have helped me and have made my life pleasant in Montreal

- My family, my parents and sisters, who always support me, regardless of the situation or the distance

Finally, special thanks to my wife Xitlali for her love, friendship, support and encouragement regardless of the distance or adversities.

Miguel Cervantes Martinez, 2019.

RÉSUMÉ

La conception et le fonctionnement efficace des lignes de transmission dépendent fortement des simulations précises des transitoires électromagnétiques, qui nécessitent de couvrir une large gamme de fréquences, comprenant celles très proches du courant continu (CC). Plusieurs approches de modélisation des lignes de transmission et des câbles ont été développées au cours des dernières décennies. Les modèles les plus sophistiqués souffrent de problèmes de performances de calcul et les modèles simplifiés ne sont pas suffisamment précis lorsqu'ils sont utilisés dans une large gamme de transitoires.

Cette thèse passe en revue les modèles prédominants à l'heure actuelle et démontre leurs inconvénients au moyen de simulations. Ensuite, elle étudie les pratiques de modélisation requises pour obtenir des simulations plus précises et plus rapides dans le domaine temporel en utilisant de modèles de lignes/câbles dépendant de la fréquence.

Dans la première partie, cette thèse contribue à une procédure d'ajustement améliorée pour l'identification de la fonction de propagation $\mathbf{H}$ dans les câbles. La procédure d'ajustement proposée repose sur des techniques de pondération adaptative et de partitionnement de fréquence afin d'assurer la précision de l'ajustement pour toutes les entrées de la matrice $\mathbf{H}$, comprenant des éléments hors diagonaux de faible magnitude. En outre, une technique de réduction d'ordre de modèle via une réalisation équilibrée est appliquée pour obtenir un ordre d'approximation réduit. Les résultats numériques montrent que la méthodologie proposée permet d'obtenir un ajustement plus précis et qu'elle, combinée à des schémas d'intégration précis, fournit des simulations stables et plus précises.

L'analyse transitoire des lignes de transmission en capturant avec précision la réponse du courant continu est devenue un intérêt particulier avec le nombre croissant de systèmes HVDC planifiés et installés. Une pratique pour capturer la réponse CC consiste à démarrer la gamme de fréquences dans le modèle à partir d'un échantillon de très basse fréquence dans l'ajustement des fonctions de ligne de transmission. Toutefois, cela peut rigidifier l'ajustement en raison de l'augmentation de la gamme de fréquences, et les valeurs calculées de tension/courant de ligne de régime permanent à courant continu peuvent s'écarter de la solution correcte. Pour résoudre ce problème, cette thèse propose une méthode d'ajustement en deux étapes dans laquelle les échantillons de basse fréquence sont exclusivement pris en compte. Dans une première étape,

l'ajustement est réalisé en excluant les échantillons de très basse fréquence tels que ceux inférieurs à 1 Hz. Dans une deuxième étape, une fonction de correction est trouvée pour les échantillons basse fréquence uniquement. Il est proposé d'utiliser cette approche pour éviter les instabilités numériques dues à un ajustement déséquilibré et pour améliorer la précision de la réponse CC.

D'autre part, cette thèse propose une méthode de relaxation permettant de surveiller le contenu fréquentiel d'un transitoire et d'ajuster les calculs de modélisation convenablement, afin d'obtenir de meilleures performances sans perte de précision significative. Il est proposé de basculer entre les modèles WB et PI pendant la simulation. Fondamentalement, l'idée est de relaxer les équations de ligne pendant le régime permanent dans la simulation pour augmenter la vitesse des calculs de type EMT. La commutation entre les deux modèles est effectuée en modifiant les termes du courant d'histoire et leurs éléments correspondants dans la matrice d'admittance nodale au cours de la simulation.

Les travaux de recherche présentés dans cette thèse sont également accompagnés des résultats d'essais disponibles via un groupe IEEE de Bonneville Power Administration (BPA). Les résultats d'essais disponibles permettent de valider les modèles de ligne de transmission. Les principaux objectifs sont de comprendre les facteurs dominants de la reproduction des résultats d'essais sur le terrain à l'aide de simulations et d'étudier la sensibilité des simulations à divers paramètres électriques de modélisation. Il comprend également des recherches sur la solution de problèmes complexes, tels que l'effet couronne distribué. Il est démontré que les résultats des simulations sont considérablement surestimés, sauf si l'effet couronne est inclus.

Enfin, cette thèse contribue à une recherche sur des simulations statistiques de surtensions de commutation pour déterminer la pire surtension à la réception d'une ligne de transmission à charge piégée lors d'une refermeture à grande vitesse. La surtension maximale estimée obtenue à partir des simulations statistiques montre un bon accord avec celle enregistrée lors des tests sur le terrain.

ABSTRACT

The design and effective operation of transmission lines strongly depend on accurate electromagnetic transients (EMT) simulations, which require covering a wide range of frequencies including those very close to DC. Several approaches for transmission line and cable modeling have been developed during the last decades. The more sophisticated models suffer from computational performance issues, and the simplified models are not sufficiently accurate when they are used in a wide range of transients.

This thesis first reviews the most currently predominant models and demonstrates their drawbacks through simulations. Then, it investigates the modeling practice required to obtain more accurate and faster time-domain simulations using frequency-dependent line/cable models.

In the first part, this thesis contributes with an improved fitting procedure for the identification of the propagation function $\mathbf{H}$ in cables. The proposed fitting procedure relies on adaptive weighting and frequency partitioning techniques to ensure the precision of fitting for all the entries of $\mathbf{H}$ including the low-magnitude off-diagonal elements. In addition, a model order reduction technique via balanced realization is applied to obtain a reduced order of approximation. Numerical results show that the proposed methodology allows obtaining more accurate fitting, and when combined with more precise integration schemes, it yields stable and more accurate time-domain simulations.

Transient analysis of transmission lines while accurately capturing the DC response has become of special interest with the increasing number of planned and installed HVDC systems. One practice to capture the DC response is to start the frequency range in the model from a very low frequency sample in the fitting of transmission line functions. However, this may stiffen the fitting due to increased range of frequencies, and the calculated DC steady-state line voltage/current values may deviate from the correct solution. To address this problem, this thesis proposes a two-stage fitting method in which low frequency samples are exclusively considered. In the first step, the fitting is performed by excluding very low frequency samples such as those below 1 Hz. In the second step, a correction function is found for the excluded low frequency samples. It is proposed to use this approach for avoiding numerical instabilities due to unbalanced fitting, and for improving the precision of the DC response.

In the other part, this thesis proposes a relaxation method that can monitor the frequency content of a transient and adjust model mathematics accordingly to achieve better performance without significant loss of accuracy. It is proposed to switch between WB and PI models during the simulation. Basically, the idea is relaxing the line equations during the steady state in the simulation to increase the speed of the EMT-type computations. The switching between the two models is performed by modifying the terms of the history current and their corresponding elements in the nodal admittance matrix during the simulation.

The research work presented in this thesis is also accompanied by test data available through an IEEE group from Bonneville Power Administration (BPA). The available test data allows to validate the transmission line models. The main objectives are to understand the major factors in the reproduction of field measurements using simulations and to investigate the sensitivity of simulations to various modeling electrical parameters. It also includes research on the solution of complicated problems, such as distributed corona effect. It is demonstrated that simulation results are significantly overestimated unless the effect of corona is included.

Finally, this thesis contributes with an investigation on statistical simulations of switching overvoltages to determine the worst overvoltage at the receiving end of a transmission line with trapped charge during a high-speed reclosing. The estimated maximum overvoltage obtained from the statistical simulations shows a good agreement with the one recorded in the field tests.

TABLE OF CONTENTS

LIST OF TABLES

LIST OF FIGURES

LIST OF SYMBOLS AND ABBREVIATIONS

AC   Alternating current

BPA   Bonneville Power Administration

BR   Balanced realization

CP   Constant Parameter

DC   Direct current

EMT   Electromagnetic transients

EMTP   Electromagnetic Transients Program

FD   Frequency dependent

FDBR   Frequency-domain balance realization

FDCM   Frequency-dependent cable model in phase domain

FDM   Frequency dependent model

FDM/DC   FDM with DC correction

FDQ   Frequency-dependent cable model based on modal domain

FFT   Fast Fourier transform

$\mathbf{H}$ Propagation function matrix

HF   High frequency

HVDC   High voltage direct current

IEEE   Institute of Electrical and Electronic Engineering

LF   Low frequency

MPM   Matrix pencil method

MOR   Model order reduction

NLT   Numerical Laplace transform

ω Angular frequency

PI	Lumped PI circuit
$\mathbf{Q}$	Transformation matrix
ρ_g	Ground resistivity
r	Radius of a conductor
$\mathbf{R}$	Per unit length series resistance matrix
RC	Parallel resistive-capacitive lumped circuit
R_{dc}	Resistance of DC
RWB	Reduced-order WB
s	Complex frequency
τ	Propagation time delay
$\mathbf{T}$	Matrix of eigenvectors of the product $\mathbf{YZ}$
ULM	Universal line model
VF	Vector fitting
WB	Wideband
WB-CP	Adaptive line model: switching between WB and CP
WB-PI	Adaptive line model: switching between WB and PI
WB-RWB	Adaptive line model: switching between WB and RWB
WF	Weighting fitting technique
WFP	WF technique combined with frequency partitioning
WFP-MOR	WFP technique combined with MOR
$\mathbf{Y}$	Per unit length shunt admittance matrix
$\mathbf{Y_c}$	Characteristic admittance matrix
$\mathbf{Z}$	Per unit length series impedance matrix

LIST OF APPENDICES

CHAPTER 1   INTRODUCTION

1.1 Motivation

The transmission line is one of the most important devices in the electrical power system, its primary function is to transfer electrical power from generating stations to consumers. Typically, aerial lines are used for long distances in rural zones, while underground cables are used in urban areas.

The design and effective operation of transmission lines strongly depends on accurate electromagnetic transients (EMT) simulations, which are obtained using precise line models. Line modeling is much easier when the line equations are formulated directly in the frequency domain [1], [2]. However, for transient analysis of large systems, the step-by-step time-domain solution [3] is more flexible than frequency-domain formulations, especially with the presence of nonlinear elements and switching events in the network. Thus, time-domain based models are preferred and widely used in practice.

Transmission lines are characterized by two electrical parameters, i.e., series impedance $\mathbf{Z}$ (longitudinal field effects), and shunt admittance $\mathbf{Y}$ (transversal field effects) matrices. Considering the nature of these parameters, time-domain line models can be divided into two groups: lumped- and distributed-parameters models. In the lumped-parameter models, both $\mathbf{Z}$ and $\mathbf{Y}$ are calculated at a single frequency. These models, also called PI models, are adequate for steady-state studies when calculating parameters at fundamental power frequency. For transient studies, the most appropriate models are those that consider line parameters distributed along the distance. These models are formulated based on the traveling-wave theory [3]-[5], and can be classified into two categories: a) constant parameters and b) frequency-dependent parameters models.

The constant parameter (CP) model considers that $\mathbf{Z}$ and $\mathbf{Y}$ are independent of the frequency effects caused by the skin effect on phase conductors and on the ground [5]. The CP model implementation requires a small computational burden [5]. However, since a transient typically involves a wide range of frequencies, the CP model is only recommended for modeling lines located on zones distant to the area where the transient event occurs.

The implementation of frequency-dependent models requires rational function-based approximations of two coefficients: the characteristic admittance $\mathbf{Y_c}$, which relates current waves to voltage waves, and the propagation function $\mathbf{H}$, which defines the delay and distortion of a wave traveling along the line. Rational functions allow efficient computation of convolution integrals in the time-domain through recursive schemes.

Early attempts to include frequency dependence in traveling-waves based models for transient simulations relied on performing direct numerical convolutions [6]-[8]. The major drawbacks encountered in those convolution methods are the excessive computation time and large accumulation errors. These problems were first addressed with the introduction of the recursive convolution scheme [9]-[11]. Afterwards, several models have been developed during the last decades, which can be classified into two groups: a) modal-domain, and b) phase-domain based models.

Modal-domain models

Modal-domain based models typically assume a constant transformation matrix [6]-[13]. In general, these models provide accurate representations for a large class of lines. However, when the frequency dependence of modal transformation matrices is very strong, the assumption of constant transformation matrices causes inaccuracies [14]. Therefore, their accuracy is restricted to aerial lines with symmetric or nearly-symmetric configurations.

The consideration of the frequency-dependent modal transformation can be achieved by applying a convolution to the matrix columns, as proposed in [14]. However, it has been encountered that transformation matrices cannot be synthesized with sufficient accuracy in many cases, yielding to imprecisions and numerical instabilities in time-domain simulations [15].

Phase-domain models

The issues associated with the constant transformation matrices mentioned above can be avoided by fitting the line functions directly in the phase domain [16]-[27]. However, this conveys complexities because the elements of $\mathbf{H}$ contain modal contributions with multiple time delays. Some models suggest extracting a single time-delay from each entry of $\mathbf{H}$ [18], [19]. However, this may stiffen the fitting procedure, requiring a high order fitting. This problem is addressed in other models by including modal time delays in the phase-domain formulation [21]-[27].

One of the most accepted phase-domain models is the universal line model (ULM) [27], which has been implemented in many EMTP-type programs. The ULM has a two-step fitting approach in which the poles of $\mathbf{H}$ are identified in the modal domain together with time delays, and the residues in the phase domain. Repetitive or close modal delays are grouped. The criterion for grouping is the difference in angle and magnitude at a high frequency [28]-[30]. Since its proposal, ULM has received several improvements related to fitting accuracy [31], out-of-band passivity violations [32]-[33], matrix symmetry issues [34], and real-time implementation [35].

Although the ULM is considered an accurate model for both transmission lines and cables, it has been associated with numerical stability problems [36]-[39]. These problems potentially arise when the propagation function $\mathbf{H}$ is fitted with poles and delays coming from different but close delay groups. This is denoted as unbalanced modal contributions and it results in magnification of integration errors in time-domain simulations. Adapting more accurate integration methods and a two-step interpolation scheme, as proposed in [37], reduces integration errors and helps maintaining numerical stability in the time domain. However, the unbalanced modal contributions in $\mathbf{H}$ cannot be removed by changing the integration method, and inaccurate simulation results with spurious oscillations can still be observed in cases with high residue/pole ratios.

Fitting modal contribution groups of $\mathbf{H}$ directly in the phase-domain, as proposed in [39], avoids high residue/pole ratios. However, if the fitting of $\mathbf{H}$ is performed directly in the phase domain and per modal contribution, more poles are required compared to ULM approach to maintain similar precisions. Moreover, since a single set of poles is used per modal contribution group to accelerate time domain simulations, the overall system of equations becomes large, and off-diagonal low-magnitude entries of $\mathbf{H}$ may not be accurately fitted. Even though off-diagonal entries of $\mathbf{H}$ are of very small magnitude, their poor fitting may have an observable impact on induced transient voltages.

Curve fitting techniques

The basic idea of frequency-dependent line models in EMT-type programs is to use rational approximations for $\mathbf{Y_c}$ and $\mathbf{H}$, calculated by using different methodologies. Among existing methodologies, the vector fitting (VF) method has been widely used for the fitting of measured or calculated frequency-domain functions with rational function approximations [40]. Alternatively,

the matrix pencil method (MPM) [46] has also been applied to rational fitting of frequency responses [47], [48]. However, the MPM is not as direct as VF method, since it requires additional numerical operations from and to the time-domain and the frequency-domain, involving a set of closed-form formulas based on the Fourier transform [49].

After its original proposal, the VF method has been modified to improve its numerical performance [41]-[43]. However, its equations may become ill-conditioned for wide frequency ranges, creating problems for low order rational fitting. To address this problem, the orthonormal vector fitting, and the weighted vector fitting have been proposed in [44], and [45], respectively.

Partitioning of frequency responses improves fitting precision. This idea has been applied for the modeling of frequency dependent network equivalents [50]-[52], transmission lines [53], and underground cables [54]. The downside is the increasing number of poles. Recently, the application of a model order reduction [52] via a balance-realization (BR)-based technique [55], [56] has been proposed to remove the redundant poles.

Corona effect

It has been mentioned the importance of including the frequency dependence of line parameters in the line modeling. However, even though frequency dependent line models provide accurate time-domain simulations, conservative results can be obtained unless the corona effect is considered [57]. The corona effect has a strong influence on the propagation of waves [57]-[63].

The corona discharge is produced by the ionization of the air surrounding a conductor that is electrically charged. This occurs when the voltage of a conductor reaches a critical value, i.e. corona inception voltage [59]. The storage and movement of charges in the ionized region can be viewed as an increase of the conductor radius and consequently of the capacitance to ground [58]. The effect of corona is characterized by the charge-voltage (q-v) response of the conductors of the transmission line [59].

The representation of corona involves a distributed nonlinear hysteresis behavior which becomes difficult to combine with the EMTP-type transmission line formulations. Most of the methods proposed in the literature rely on the two following techniques: i) subdividing lines in linear subsections with non-linear shunt branches at each junction [58], and ii) applying finite differences methods to line equations [60]. The latter presents less numerical oscillations than the former; however, it requires a significant computational burden [60].

Existing corona models can be classified into two groups: static and dynamic. In general, all the models need to calculate beforehand the corona inception voltage [59]. Static models are those in which the corona capacitance is only a function of the voltage. In this type of models, a fixed nonlinear q-v characteristic is assumed, and can be either simulated directly by using RC circuits and diodes [61], or described by analytical expressions [62]. Dynamic models consider the fact that the charge depends on the voltage and on the rate of change of the voltage [63].

1.2 Contributions

EMT simulations require covering a wide range of frequencies including those very close to DC. As mentioned before, several line and cable models have been developed during the last decades [3]-[27]. It is concluded that the more sophisticated models suffer from computational performance issues, and the simplified models are not sufficiently accurate when they are used in a wide range of transients.

This thesis first reviews the most predominant models in the literature and demonstrates their drawbacks through simulations. Then, it investigates the modeling practice required to obtain more accurate and faster time-domain simulations using frequency-dependent line/cable models.

The contributions of this thesis are detailed as follows.

A) Identification procedure of the propagation function

This thesis contributes with precise fitting procedures for the identification of **H** in the phase domain while maintaining reduced order of approximation. In the proposed fitting approach, poles and residues of **H** are identified simultaneously in the phase domain. The procedure encapsulates the following proposed features. An adaptive weighting technique is applied to normalize all the entries of **H** prior to fitting. This allows ensuring the precision of fitting for all the entries including the low-magnitude off-diagonal elements. The frequency band of fitting is partitioned so that the fitting problem is simplified, and the accuracy is improved compared to the standard application of vector fitting. Finally, a model order reduction (MOR) technique via balanced realization (BR) is applied to obtain a reduced order of approximation.

The proposed methodology allows obtaining more accurate fitting, and when combined with more precise integration schemes, it yields more stable and more accurate time-domain simulations.

B) DC correction in wideband models

Transient analysis of transmission lines with accurate capturing of the DC response, has become of special interest with the increasing number of planned and installed HVDC systems [65]-[68]. One practice to capture the DC response in the ULM is to specify a very low frequency for fitting $\mathbf{H}$ and $\mathbf{Y_c}$. However, this approach often leads to incorrect solutions for the DC steady-state voltages and currents due to generally poor DC fitting [69]-[70]. To address this problem, this thesis contributes with a two-stage fitting method in which low frequency samples are given priority. In the first stage, the fitting is performed by excluding very low frequency samples such as those below 1 Hz. In the second stage, a correction function is found for the excluded low frequency samples. It is proposed to use this approach for avoiding numerical instabilities due to unbalanced fitting, and for improving the precision of DC response.

C) Adaptive line modeling

Another contribution of this thesis is a relaxation method that can monitor the frequency content of a transient and adjust model mathematics accordingly to achieve better performance without significant loss of accuracy. Simulation of EMT using relaxing models have been proposed through the shift frequency concept [71]-[74]. In this thesis, it is proposed to switch between wideband (WB) and PI models during the simulation. Basically, the idea is to relax the line equations during the steady state to increase the speed of the EMT-type computations. The switching between the two models is performed by modifying the terms of the history current vectors and their corresponding elements in the nodal admittance matrix during the simulation.

D) Validation of line models with field measurements

One more contribution of this thesis is to validate transmission lines model with field tests and to identify the required simulation practices in reproducing field measured overvoltages in EMT simulations. The test data are available through an IEEE working group from Bonneville Power Administration (BPA). It is demonstrated that even though the pattern of the transient voltage waveforms can be reproduced very well using frequency-dependent line models, simulations results are significantly overestimated unless the effect of corona is included. Two types of corona models are tested; both models demonstrate that corona is the primary factor that allows the simulations to correctly reproduce field measurements.

E) Statistical study of switching overvoltages

This thesis also contributes with an investigation on statistical simulations of switching overvoltages to determine the worst overvoltage at the receiving end of a transmission line with trapped charge.

1.3 Thesis outline

This thesis is composed of eight chapters and two appendices.

CHAPTER 1 – INTRODUCTION, explains the background motivating this PhD project, and summarizes its objectives and contributions.

CHAPTER 2 – REVIEW OF LINE/CABLE MODELS, contains the basic theory essential for a better understanding of the content of this thesis. This includes main equations and a general classification of line and cable models. In addition, it demonstrates the drawback of current models through time-domain simulations.

CHAPTER 3 – ENHANCED FITTING TECHNIQUES FOR THE IDENTIFICATION OF THE PROPAGATION FUNCTION, presents fitting procedures for the identification of the propagation function in the phase domain. The proposed procedure encapsulates: Frequency partition and adaptive weighting techniques to ensure the precision of fitting, and a model order reduction method via balanced realization to obtain a reduced order of approximation. It also includes an additional two-stage fitting procedure for improving the precision of DC response.

CHAPTER 4 – TIME DOMAIN SIMULATIONS, analyses the impact of improving the fitting of the propagation function in time-domain simulations via transient studies. The proposed fitting procedures are combined with more precise integration schemes to obtain stable and more accurate simulation results.

CHAPTER 5 – ADAPTIVE LINE MODEL, presents a relaxation method to increase the speed of time-domain simulations. It is proposed to switch between WB and PI models during the simulation. The idea is illustrated via a simple case of study.

CHAPTER 6 – SIMULATION OF SWITCHING OVERVOLTAGES AND VALIDATION WITH FIELD TEST, presents the analysis of other important factors in line modeling, such the consideration of corona. It includes validation of transmission lines with field test.

CHAPTER 7 – STATISTICAL SIMULATIONS OF SWITCHING OVERVOLTAGES, presents a statistical simulation study to determine the worst overvoltage at the receiving end of a transmission line during high-speed reclosing with a trapped charge on the line.

CHAPTER 8 – CONCLUSION, presents the main conclusions of this thesis, the list of publications derived from its contributions and possible future work.

APPENDIX A – CONSTANT PARAMETER LINE MODEL DETAILS, presents the time-domain implementation details of the constant parameter line model.

APPENDIX B – CORONA MODEL DETAILS, summarizes the equations and parameters of the corona models used in Chapter 6.

CHAPTER 2   REVIEW OF LINE/CABLE MODELS

This chapter presents the basic theory related to line/cable modeling, including main equations and a general classification of time-domain models. In addition, it demonstrates the drawback of current models used for EMT through time-domain simulations.

2.1 Main equations

2.1.1 Equations in the frequency domain

Most of existing transmission line models for EMT simulations are based on the traveling-wave theory [3]. Figure 2.1 illustrates reference directions of a transmission line of length L assuming N conductors parallel to the ground.
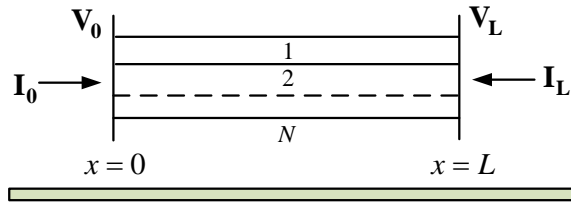
Figure 2.1 Multiconductor line segment of length L

At each point of the line depicted in Figure 2.1, the frequency domain line equations are expressed as:

$$\frac{d\mathbf{V}}{dx} = -\mathbf{ZI} \tag{2.1}$$

$$\frac{d\mathbf{I}}{dx} = -\mathbf{YV} \tag{2.2}$$

where $\mathbf{Z}$ and $\mathbf{Y}$ are the per unit length series impedance (longitudinal field effects) and shunt admittance (transversal field effects) matrices, respectively. Both $\mathbf{Z}$ and $\mathbf{Y}$ can be numerically obtained from the geometry and the electrical parameters of the line [75].

The general solution of (2.1) and (2.2) can be expressed as [4]:

$$\mathbf{I}(x) = e^{-\mathbf{\Gamma}x}\mathbf{I_F} + e^{\mathbf{\Gamma}x}\mathbf{I_B} \tag{2.3}$$

$$\mathbf{V}(x) = \mathbf{Y_c}^{-1}\left(e^{-\mathbf{\Gamma}x}\mathbf{I_F} - e^{\mathbf{\Gamma}x}\mathbf{I_B}\right) \tag{2.4}$$

where $\mathbf{\Gamma} = \sqrt{\mathbf{YZ}}$; the forward and backward currents, $\mathbf{I_F}$ and $\mathbf{I_B}$, can be obtained from the boundary conditions of the line. The characteristic admittance matrix $\mathbf{Y_c}$ is given by:

$$\mathbf{Y_c} = \mathbf{\Gamma Z}^{-1} \tag{2.5}$$

In EMTP-type models, the transmission line/cable is represented by decomposing the current waves into incident and reflected waves as depicted in Figure 2.2.
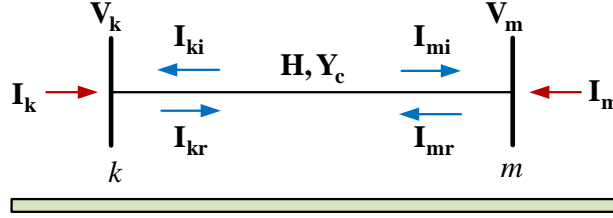
Figure 2.2 Traveling-wave multiconductor line/cable segment

Based on (2.3) and (2.4), and the reference directions given in Figure 2.2, the frequency-domain voltages and currents at both ends are related by:

$$\mathbf{I_k} = \mathbf{Y_c V_k} - \mathbf{H}\left(\mathbf{I_m} + \mathbf{Y_c V_m}\right) = \mathbf{I_{sh_k}} - \mathbf{I_{ki}} \tag{2.6}$$

$$\mathbf{I_m} = \mathbf{Y_c V_m} - \mathbf{H}\left(\mathbf{I_k} + \mathbf{Y_c V_k}\right) = \mathbf{I_{sh_m}} - \mathbf{I_{mi}} \tag{2.7}$$

where $\mathbf{I_k}$ and $\mathbf{I_m}$ are the vectors of injected currents, and $\mathbf{V_k}$ and $\mathbf{V_m}$ correspond to nodal voltage vectors. Also, subscripts $\mathbf{i}$ and $\mathbf{r}$ refer to incident and reflected waves, respectively. $\mathbf{H}$ is the propagation function matrix defined by:

$$\mathbf{H} = e^{-\mathbf{\Gamma} L} \tag{2.8}$$

Equivalently, the model defined by (2.6) and (2.7) can be expressed in terms of a two-port network. Combining (2.6) and (2.7), and defining $\mathbf{U}$ as the identity matrix, the two-port model is given by:

$$\begin{bmatrix} \mathbf{I_k} \\ \mathbf{I_m} \end{bmatrix} = \left\{ \left(\mathbf{U} - \mathbf{H}^2\right)^{-1} \begin{bmatrix} \mathbf{H}^2 + \mathbf{U} & -2\mathbf{H} \\ -2\mathbf{H} & \mathbf{H}^2 + \mathbf{U} \end{bmatrix} \mathbf{Y_c} \right\} \begin{bmatrix} \mathbf{V_k} \\ \mathbf{V_m} \end{bmatrix} \tag{2.9}$$

2.1.2 Equations in the time domain

To obtain the time-domain counterparts of (2.6) and (2.7), convolution operations (denoted by $*$) at line/cable terminals must be performed, as indicated in (2.10) to (2.13) (time-domain variables indicated with lowercase letters).

$$\mathbf{i}_{sh_k} = \mathbf{y}_c * \mathbf{v}_k \tag{2.10}$$

$$\mathbf{i}_{sh_m} = \mathbf{y}_c * \mathbf{v}_m \tag{2.11}$$

$$\mathbf{i}_{ki} = \mathbf{h} * \left(\mathbf{i}_m + \mathbf{i}_{sh_m}\right) = \mathbf{h} * \mathbf{i}_{mr} \tag{2.12}$$

$$\mathbf{i}_{mi} = \mathbf{h} * \left(\mathbf{i}_k + \mathbf{i}_{sh_k}\right) = \mathbf{h} * \mathbf{i}_{kr} \tag{2.13}$$

The objective is to obtain the Norton equivalent shown in Figure 2.3 by solving the time-domain versions of (2.6) and (2.7). The history current sources in Figure 2.3 are obtained using the convolutions involved in (2.10) to (2.13). The $\mathbf{G}_{Y_c}$ term is calculated from the convolution of the characteristic admittance with a terminal voltage.
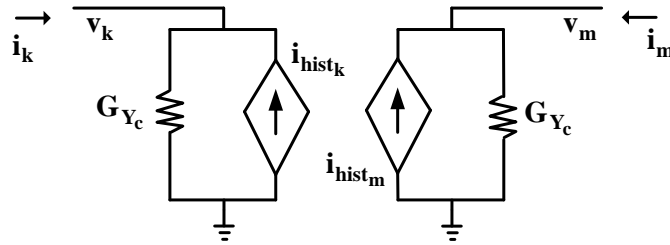
Figure 2.3 Equivalent Norton circuit

The time-domain implementation of this type of model requires the synthesis of $\mathbf{H}$ and $\mathbf{Y}_c$. The identification of rational functions for these two matrices is not straightforward, particularly in the case of $\mathbf{H}$ due to multiple time delays [27].

2.2 Classification of line/cable models

Figure 2.4 presents a general classification of the most commonly used transmission line/cable models for EMT simulations. Considering the nature of $\mathbf{Z}$ and $\mathbf{Y}$, the line models can be divided into two groups: 1) lumped- and 2) distributed-parameters models.
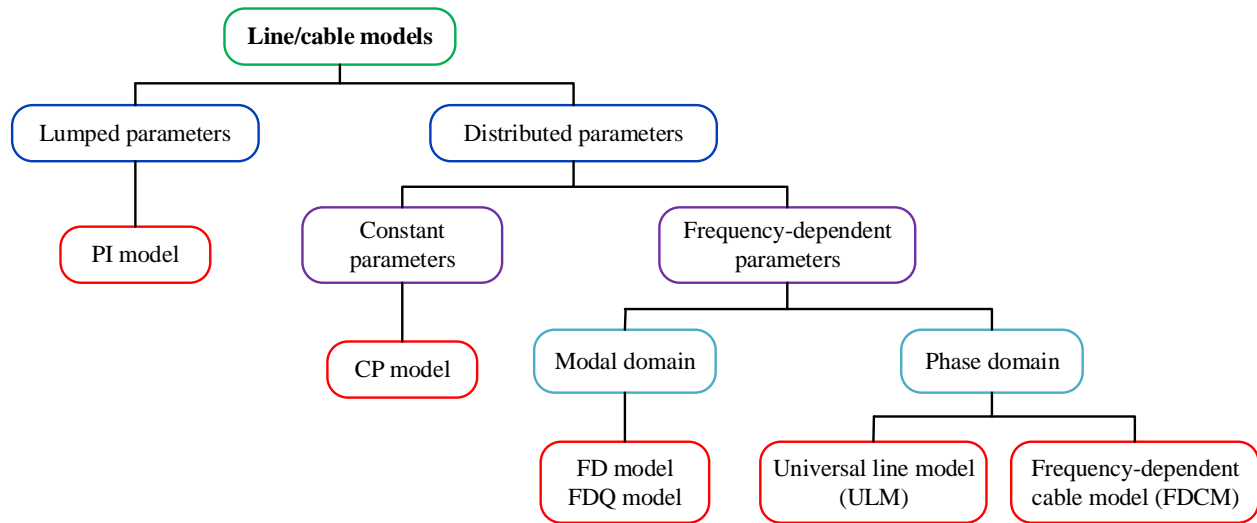
Figure 2.4 Classification of the currently most predominant line/cable models

2.2.1 Lumped parameter models

In the lumped parameter models, or PI models, the coefficients $\mathbf{Z}$ and $\mathbf{Y}$ are calculated at a single frequency; thus, (2.9) can be directly used for modeling a line segment. For a time-domain simulation, the model of (2.9) can be discretized according to the integration time-step and solved at each simulation time-point [4]. However, since this model is only capable to simulate one frequency, its application is only adequate for steady-state purposes. For instance, harmonic initialization and frequency scan solutions.

2.2.2 Distributed parameter models

For EMT simulations, the most appropriate models are those that consider the parameters distributed along the distance. These models use (2.6) and (2.7) to represent the line at each end by a Norton equivalent circuit [4], as shown in Figure 2.3. This group of models may consider the parameters $\mathbf{Z}$ and $\mathbf{Y}$ as: a) constant- or, b) frequency-dependent.

The constant parameter (CP) model considers that (2.6) and (2.7) are resolved independently of the frequency effects, avoiding numerical convolution operations and consequently requiring a small computational burden [5]. However, since the propagation modes cannot be represented at high frequencies, the CP model is only recommended for modeling lines in analysis of problems with limited frequency dispersion.

The basic idea of frequency-dependent line models in EMT-type programs is to use rational approximations for $\mathbf{Y_c}$ and $\mathbf{H}$, calculated by using different methodologies [40]-[46]. Rational functions allow efficient computation of convolution integrals through recursive schemes. The identification of $\mathbf{Y_c}$ and $\mathbf{H}$ is not straightforward, particularly in the case of $\mathbf{H}$, due to multiple time delays [30]. Several frequency-dependent line models have been proposed during the last decades [6]-[27], the most predominant ones are reviewed in the next section.

2.3 Frequency-dependent models

Frequency-dependent line and cable models used for EMT simulations can be divided into two groups: a) modal-domain, and b) phase-domain based models.

2.3.1 FD model (modal domain)

In the frequency-dependent line model proposed in [12], named in this thesis as FD model, the multiphase line functions are decoupled via modal transformation. The transformation matrix used to relate modal and phase quantities is assumed to be constant and real. The line functions, i.e., the characteristic impedance $\mathbf{Z_c}$ and the propagation function $\mathbf{H}$, in the modal domain are calculated as:

$$\mathbf{Z_c^m} = \mathbf{Q}^T \mathbf{Z_c} \mathbf{Q} \tag{2.14}$$

$$\mathbf{H}^m = \mathbf{Q}^{-1} \mathbf{H} \mathbf{Q} \tag{2.15}$$

where $\mathbf{Q}$ is the eigenvector matrix which diagonalizes the product $\mathbf{YZ}$ and superscript m indicates modal quantity. The FD model represents frequency dependence by fitting $\mathbf{Z_c}$ and $\mathbf{H}$ for each mode using a Bode approximation [12]. Then, each mode is solved separately as a single-phase circuit. For time-domain implementation details see [12].

Synthesis of the characteristic impedance

In the fitting procedure presented in [12], the characteristic impedance $\mathbf{Z_c}$ is formulated by a series of RC parallel blocks. The rational function of each mode m of $\mathbf{Z_c^m}$ is of the form

$$Z_c^m = K \frac{(s+z_1)(s+z_2)\cdots(s+z_M)}{(s+p_1)(s+p_2)\cdots(s+p_M)} \qquad (2.16)$$

where z_i and p_i are real and positive zeros and poles, respectively, and K is a constant value. Equivalently, (2.16) can be expressed as a partial fraction expansion as follows

$$Z_c^m = k_0 + \sum_{i=1}^{M} \frac{k_i}{s+p_i} \qquad (2.17)$$

where M is the order of approximation, k_0 is a constant value, and k_i and p_i represents its ith pole and its ith residue, respectively.

Synthesis of the propagation function

The modes of the propagation function **H** are normalized as minimum-phase-shift functions prior to fitting [12]. The propagation modes are represented by the rational approximation of the form

$$H^m \cong \sum_{i=1}^{M} \frac{k_i}{s-p_i} e^{(-s\tau_m)} \qquad (2.18)$$

where τ is a real constant value associated with a modal time delay.

Frequency-dependent transformation matrix

The FD model provides accurate representations for a large class of line configurations. However, their accuracy is restricted to cases where the frequency dependence of the transformation matrix **Q** is not very strong, i.e., aerial lines with symmetric or nearly symmetric configuration; thus, it is not applicable to cables.

The consideration of the frequency-dependent modal transformation in the model can be achieved by applying additional convolution operations to the transformation matrix elements, as proposed in the cable model presented in [14]. In this model, named in this thesis as FDQ model, each entry of the full transformation matrix **Q** is approximated with

$$Q = k_0 + \sum_{i=1}^{M} \frac{k_i}{s+p_i} \qquad (2.19)$$

To obtain the rational approximation of the entries of $\mathbf{Q}$, its eigenvectors are normalized prior to fitting, so that one of its elements becomes real and constant along the entire frequency range. This procedure allows that all the entries of $\mathbf{Q}$ become minimum-phase-shift functions. It is noted that $\mathbf{Q}$ can be fitted only when its elements are continuous function of frequency [14].

2.3.2 ULM (phase domain)

The ULM [27] accounts for frequency-dependent parameters and constitutes a wideband model. Although ULM has its bases on modal factorization, it resolves the multiconductor propagation relations in the phase domain. Thus, it provides highly accurate results for the simulation of coupling effects between parallel conductors, compared to the modal-domain based models.

Fitting of the characteristic admittance

The fitting of the characteristic admittance $\mathbf{Y_c}$ is not stringent as it exhibits smooth behavior in the frequency-domain. The following form is used [27]:

$$\mathbf{Y_c} \cong \mathbf{G_0} + \sum_{i=1}^{N_y} \frac{\mathbf{G}_i}{s - q_i} \tag{2.20}$$

where N_y is the order of approximation, q_i represents the ith fitting pole, $\mathbf{G}_i$ is the matrix of residues, and $\mathbf{G_0}$ is a constant matrix representing the limit of $\mathbf{Y_c}$ when $s \to \infty$.

Fitting of the propagation function

In ULM, $\mathbf{H}$ is first decoupled into single-delay terms through modal decomposition

$$\mathbf{H} = \mathbf{TH}^{\mathrm{m}}\mathbf{T}^{-1} \tag{2.21}$$

where $\mathbf{T}$ is the matrix of eigenvectors of the product $\mathbf{YZ}$, and $\mathbf{H}^{\mathrm{m}}$ is a matrix of the form

$$\mathbf{H}^{\mathrm{m}} = diag\left(e^{\lambda_1}, e^{\lambda_2}, \cdots, e^{\lambda_N}\right) \tag{2.22}$$

where the terms e^{λ_i} are the eigenvalues of $\mathbf{H}$, representing the propagation modes H_i. To compensate excessive phase lag and achieve a low-order rational approximation, a constant time delay is removed prior to fitting. Therefore, poles and delays are identified by fitting each modal propagation function with

$$H_i \cong \sum_{j=1}^{M_i} \frac{c_j}{s - p_{i,j}} e^{(-s\tau_i)} \tag{2.23}$$

where M_i is the order of the approximation for the ith mode, $p_{i,j}$ represents the jth pole, c_j represents its jth residue, and τ_i is the time associated to the ith mode. Repetitive or close modal delays are grouped. The criterion for grouping is the difference in angle and magnitude at a high frequency [27]. Once the poles and delays are known, the matrix of residues is found by solving the following overdetermined problem:

$$\mathbf{H} \cong \sum_{i=1}^{N_{gr}} \left(\sum_{j=1}^{M_i} \frac{\mathbf{R}_{i,j}}{s - p_{i,j}} e^{(-s\tau_i)} \right) \tag{2.24}$$

where N_{gr} is the number of modal groups, and $\mathbf{R}_{i,j}$ corresponds to the matrix of residues.

2.3.3 FDCM (phase domain)

Although (2.24) can be used for any cable or line configuration, it has been associated with numerical stability problems due to the existence of residue pole pairs with high ratios and opposite signs coming from different but close delay groups [39]. This results in a magnification of integration and interpolation errors in time-domain simulations.

In the frequency-dependent cable model (FDCM) proposed in [39], $\mathbf{H}$ is decomposed into modal contributions groups which are individually fitted in the phase domain. In FDCM, similar eigenvalues of $\mathbf{H}$ and their corresponding eigenvectors are grouped by summing them, and a single time delay is assigned to the group. The resulting modal contribution groups are smooth functions of frequency [39]. Thus, $\mathbf{H}$ in (2.24) is expressed now with:

$$\mathbf{H} \cong \sum_{i=1}^{N_{gr}} \hat{\mathbf{H}}_i e^{-s\tau_i} \tag{2.25}$$

where N_{gr} is the number of modal contribution groups $\hat{\mathbf{H}}_i$. The fitting of $\mathbf{H}$ is directly performed on each modal contribution group to obtain poles and residues simultaneously; consequently, the high residue/pole ratios encountered in ULM are eliminated. In (2.25), a

common set of poles can be used for each modal contribution. The exponential time delay τ_i term is removed prior to fitting, i.e.

$$\hat{\mathbf{H}}_i \approx \sum_{j=1}^{M_i} \frac{\mathbf{R}_{i,j}}{s - p_{i,j}} \tag{2.26}$$

The fitting of $\mathbf{Y_c}$ in FDCM is performed using (2.20) due to its smooth behavior in the frequency domain.

2.4 Discussion on line and cable models

This section aims to evaluate and to discuss the performance of the most predominant line and cable models used for EMT analysis. The drawbacks of such models are demonstrated trough transient simulation of practical cases. The models and routines currently implemented in EMTP are adopted for the time-domain simulations. For verification purposes, the simulation results obtained with the numerical Laplace transform (NLT) technique [2], are considered as reference solution.

2.4.1 Importance of frequency dependence of line parameters

The objective of this section is to show that frequency-dependent models are required to achieve accurate results in EMT studies.

2.4.1.1 Example 1: Energization of an overhead transmission line

This example considers the three-phase transmission line system of Figure 2.5. Figure 2.6 shows the frequency response of the Thevenin impedance seen from the source side (see Figure 2.5b), when the transmission line is represented with the line models of Figure 2.4. It can be observed that the PI model is able to represent only one resonant frequency, while the CP model loses precision at high frequencies. On the contrary, the frequency-dependent models, i.e., FD and ULM, are able to provide accurate results for the entire frequency range, compared to the exact solution obtained with (2.9).

For time-domain analysis, the line of Figure 2.5a is modeled with the approaches of Figure 2.4 and energized by a three-phase voltage source of 230 kV, see Figure 2.5b. Figure 2.7 shows the voltage of phase a at the receiving end of the line when the three phases are simultaneously

closed at $t_c = 0$ s. It is observed that FD and ULM provide accurate results when compared to NLT, while both CP and PI models are not able to properly reproduce the high frequency dispersion of the transient. This phenomenon is more evident in an unbalanced energization. Figure 2.8 shows the time-domain results when the closing times t_c are 1 ms, 6 ms, and 4 ms, for the phases a, b, and c, respectively.

(a)   (b)
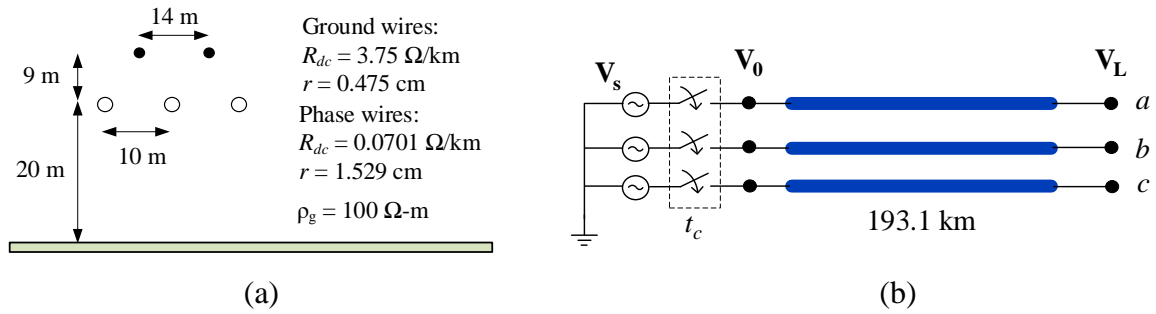
Figure 2.5 Three-phase transmission line (a) physical layout, and (b) test circuit

(a)   (b)
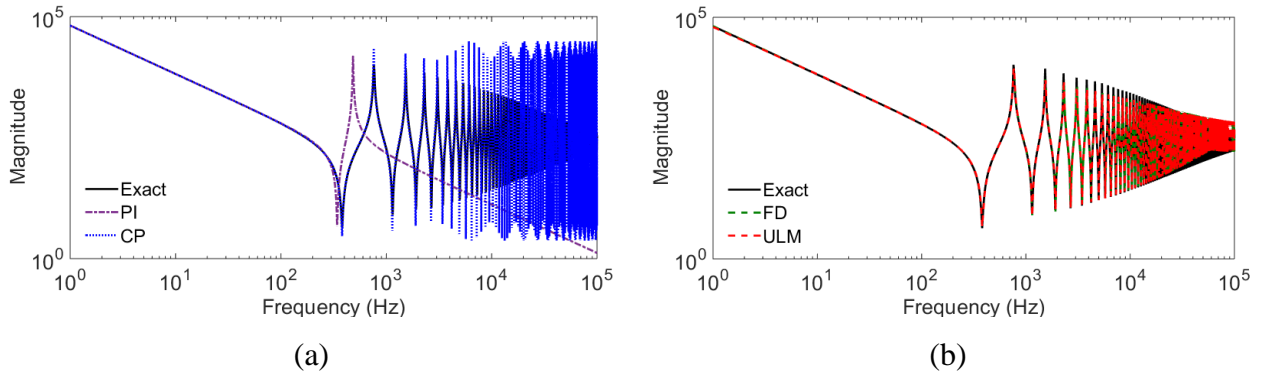
Figure 2.6 Frequency response, (a) exact versus PI and CP and (b) exact versus FD and ULM

(a)   (b)
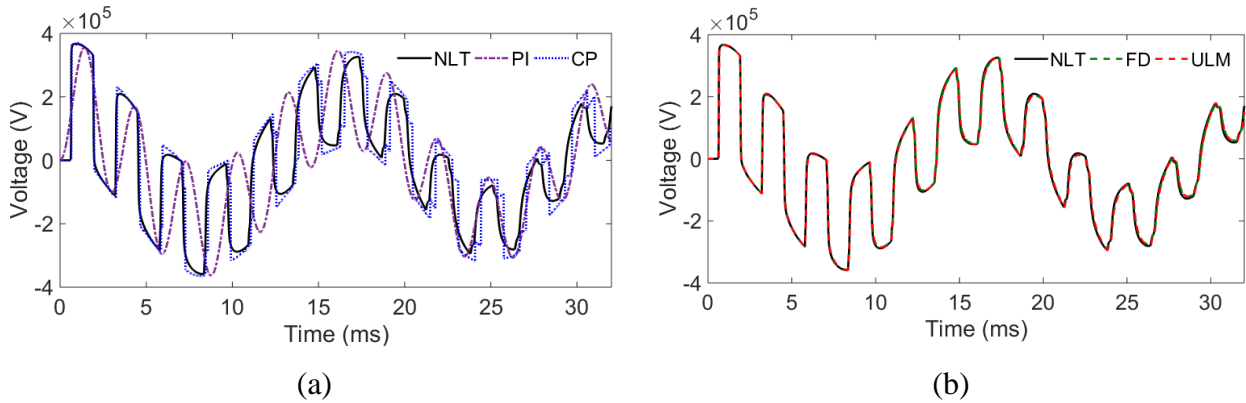
Figure 2.7 Voltage of phase a at the receiving end, balanced energization, (a) NLT versus PI and CP and (b) NLT versus FD and ULM

(a)   (b)
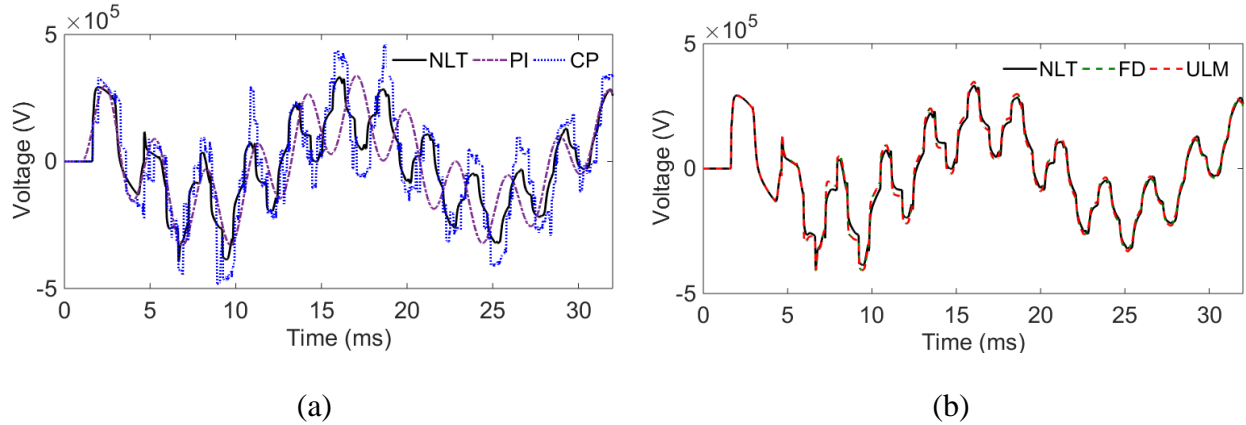
Figure 2.8 Voltage of phase a at the receiving end, unbalanced energization, (a) NLT versus PI and CP and (b) NLT versus FD and ULM

2.4.1.2 Example 2: Single-phase fault on a double circuit transmission line

This case study aims at analyzing the transient response of a faulted transmission line. For this analysis, the first circuit of the 231-kV double-circuit transmission line of Figure 2.9 is submitted to a single-phase fault. It is considered that the fault occurs at the receiving end of the first conductor (phase a), as shown in Figure 2.9b. The sending end of the second circuit is grounded by a resistor of 1 Ω while the receiving end is left open.

Figure 2.10 shows the transient response of the fault current when the line of Figure 2.9 is modeled with the CP, FD, and ULM. The frequency band considered in the fitting of line function in both FD and ULM is from 0.01 Hz to 1 MHz. As for the CP, the line parameters are calculated at 1 kHz. The simulation time-step is of 10 μs for all models. It is observed in Figure 2.10 that frequency-dependent models, i.e., FD and ULM, provide identical results, which significantly differ from the response obtained with the CP model. This is explained as follows. Although CP model considers the distributed nature of the line parameters, this model is not capable to represent the high frequency dispersion occurred during the fault. The effect of the frequency dependence is more noticeable in the transient waveform of induced voltages at the end of the line. For example, Figure 2.11 shows the induced voltage on the fourth conductor C4.

Note that the minor deviation between the simulation obtained with the FD and ULM approach is attributed to the accuracy of fitting process obtained in each model. It is remarked that the FD model is based on the modal domain, while the ULM performs the fitting in the phase domain.

(a)   (b)
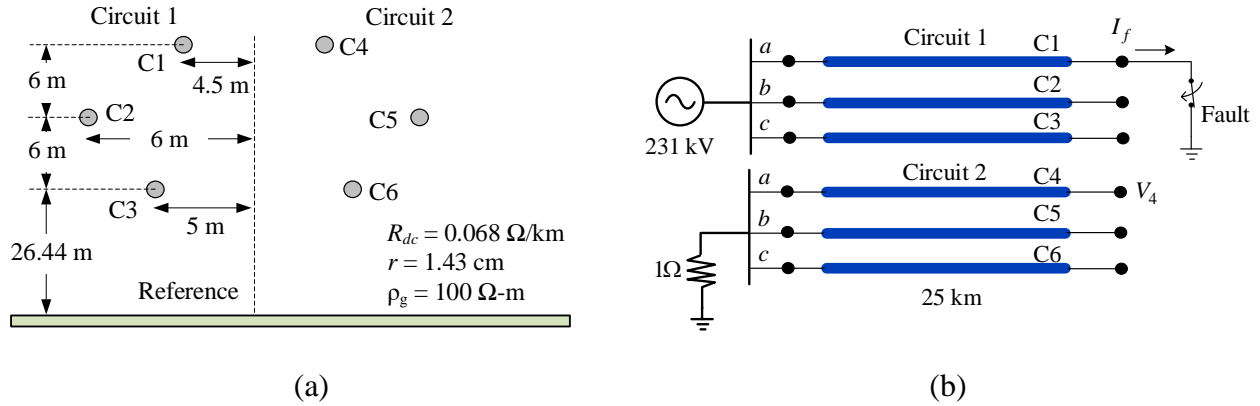
Figure 2.9 25-km double-circuit transmission lines physical (a) layout and (b) test circuit
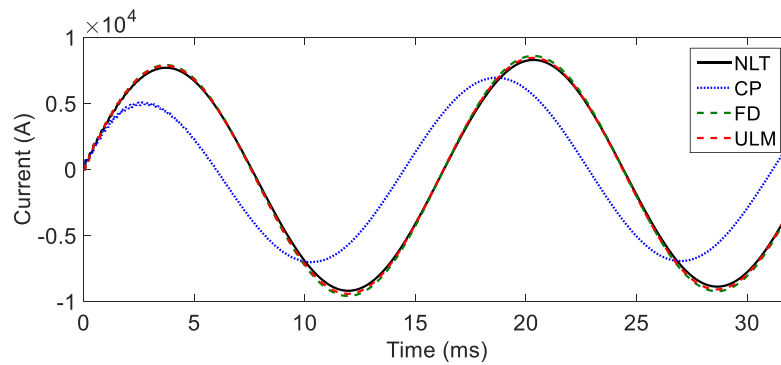
Figure 2.10 Fault current at the end of the line
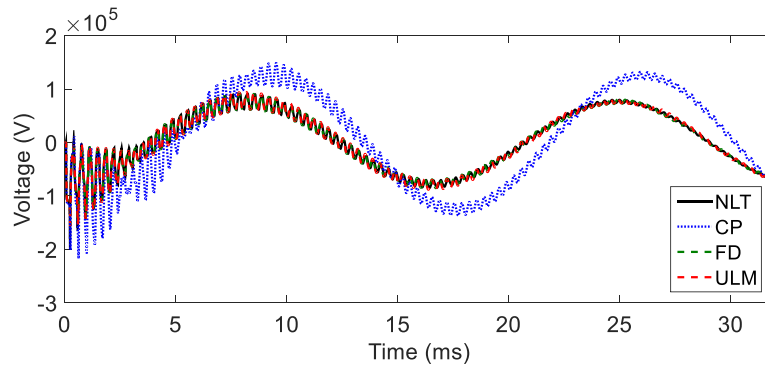
Figure 2.11 Voltage at the receiving end of conductor C4

2.4.1.3 Example 3: Three-phase underground cable

The objective of this example is to compare the CP with ULM and FDQ models, for the evaluation of sheath overvoltages by using a realistic case study. The cable system layout used in this example is shown in Figure 2.12. The corresponding electrical circuit diagram is shown in

Figure 2.13. The cable sheaths are grounded by a 1 Ω resistance at both ends. Z_s is determined by its zero- (0) and positive- (1) sequence data in ohms: $R_0 = 2$, $R_1 = 1$, $X_0 = 22$, and $X_1 = 15$. The closing times t_c are 0 ms, 0.63 ms, and 0.4 ms, for phases a, b, and c, respectively.

The transient scenario considers the energization of the cable system by a 169-kV three-phase source V_s. Figure 2.14 shows the sheath voltage of phase a at the receiving end when the cable system is modeled by the CP, FDQ and ULM approaches. It is observed that FDQ and ULM, provide identical results and accurately reproduce the high frequencies of the transient waveform, which significantly differ from the response obtained with the CP model.

	Outer Radius (m)	Resistivity (Ohm-m)	Relative Permittivity
Core	0.01254	17×10^{-7}	-
Insulator 1	0.022735	-	3.5
Sheath	0.02622	21×10^{-6}	-
Insulator 2	0.029335	-	2.0
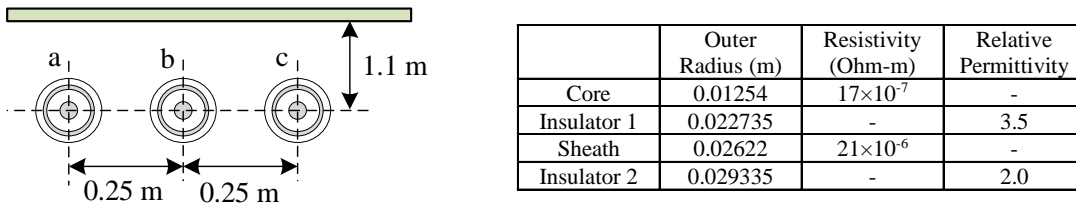
Figure 2.12 Layout and parameters details of the 15-km cable system
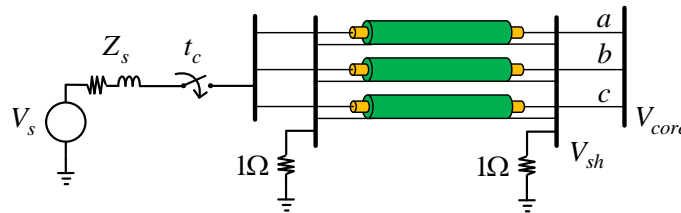
Figure 2.13 Test circuit used in the example 2
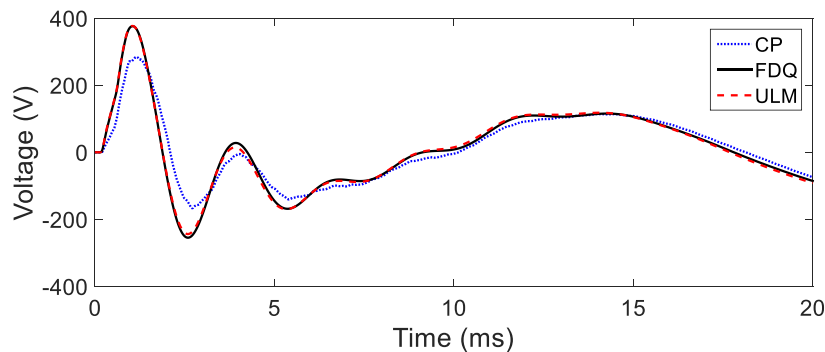
Figure 2.14 Sheath voltage of phase a at the receiving end

2.4.2 Inaccuracies of modal-domain based models

This section aims at verifying high accuracy of phase-domain based models for the simulation of induced voltages compared to modal-domain based models.

2.4.2.1 Example 4: Coupling effect between three parallel transmission lines

The FD model fits line parameters in the modal domain and accurately represents their frequency dependence in transient simulations. However, since the FD model assumes a constant transformation matrix, its precision decreases when modeling transmission line systems with highly asymmetrical configurations. On the other hand, ULM fits parameters in the phase domain. To evaluate and compare the efficiency and accuracy of FD and ULM models in asymmetrical conditions, the transmission system shown in Figure 2.15 with corresponding parameter data listed in Table 2.1 is considered as example. The system consists of two 550-kV and one 360-kV transmission lines running in parallel. For time-domain simulations, the transmission system is divided in five sections (see Figure 2.16). It is noticed that Line 3 is transposed between each section. For transient analysis, Lines 2 and 3 are energized with ideal sources of 550 kV and 360 kV, respectively. It is also noticed that Line 1 is grounded at both ends.
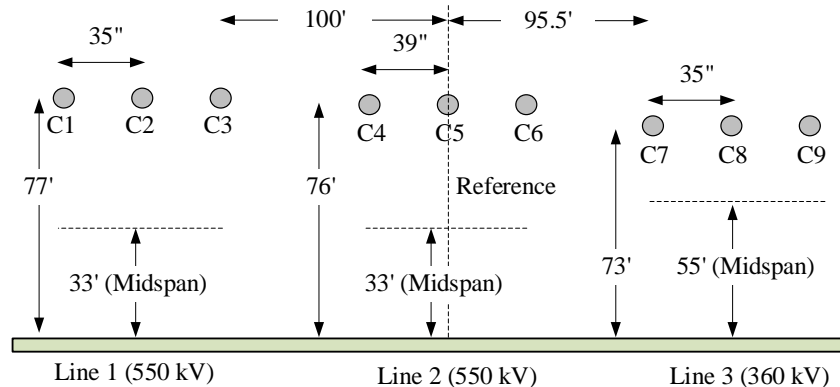
Figure 2.15 Three transmission lines in parallel

Table 2.1 Conductor data of the transmission system of Figure 2.15

Cond.	R_{dc} (Ω/mi)	r (in)	Thick/Diam	Cond. in the bundle	Spacing (in)
C1-C3	0.1510	0.500	0.4260	4	18
C4-C6	0.1600	0.475	0.3870	4	18
C7-C9	0.1288	0.554	0.4476	2	18
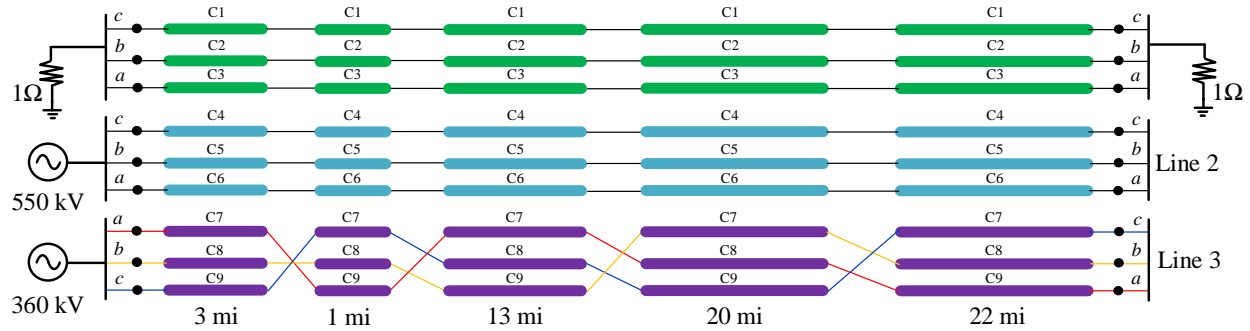
Figure 2.16 Network configuration for example 4

Figure 2.17 and Figure 2.18 show the transient voltages of phase b at the receiving ends of Line 2, and Line 3, respectively. The frequency band considered in the fitting of line function in both FD and ULM models is from 0.01 Hz to 1 MHz. The simulation time-step for both is of 1 μs. It is observed in Figure 2.17 and Figure 2.18 that there is a noticeable difference between the results obtained with FD model, the ULM, and NLT. The reason of this deviation can be explained as follows. High frequency dispersion is presented during the transient. The FD model includes frequency dependence in the model by fitting the line parameters in the modal domain and assuming a constant and real transformation matrix to relate modal and phase quantities. However, when the frequency dependence of modal transformation matrices is very strong, such as the case of the asymmetrical line system of Figure 2.15 (see the results of Figure 2.19), the assumption of constant transformation matrices causes inaccuracies in the model. On the other hand, since the ULM fits the parameters in the phase domain, it can be applicable to any line configuration, and consequently, the coupling effects between the parallel lines of Figure 2.15 are accurately represented during the simulation.
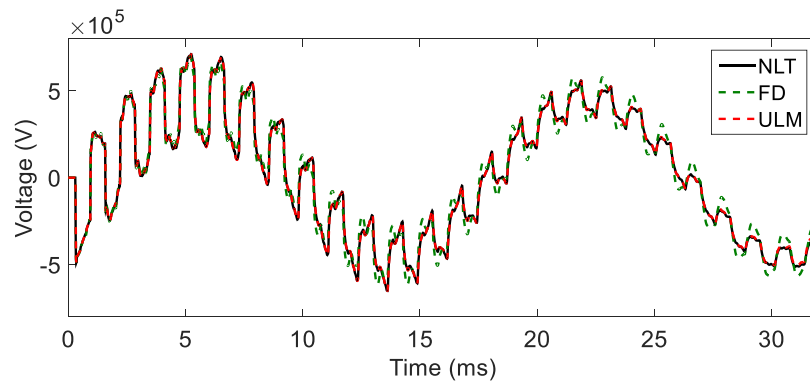
Figure 2.17 Voltage of phase b at the receiving end of Line 2
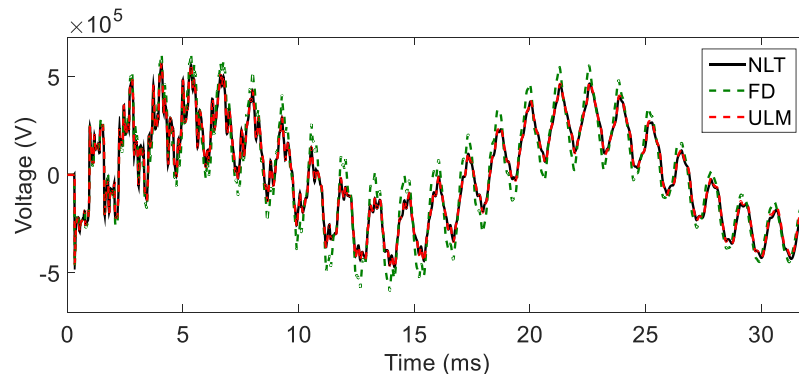
Figure 2.18 Voltage of phase b at the receiving end of Line 3

(a) (b) (c)
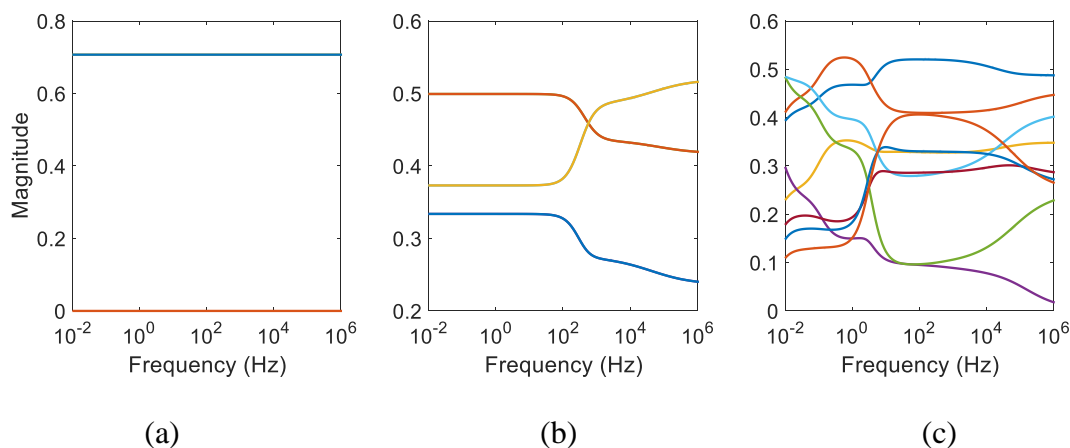
Figure 2.19 Magnitude of entries of the second column of the transformation matrix of the lines shown in: (a) Figure 2.5a, (b) Figure 2.9a and (c) Figure 2.15

2.4.2.2 Example 5: Fitting precision of the FDQ on short underground cables

As mentioned, the accuracy of the FD model is restricted to aerial lines with symmetric or nearly symmetric configuration. The basic idea of the FD model is extended in the FDQ for cable modeling purposes. The consideration of the frequency-dependent modal transformation in the FDQ is achieved by fitting each element of the transformation matrix $\mathbf{Q}$ with a rational approximation of the same form as the characteristic admittance. However, this results in additional recursive convolutions in the time domain, and consequently, additional computational burden. In addition, since eigenvectors corresponding to similar eigenvalues may exhibit a non-smooth behavior, is not always possible to fit the entries of $\mathbf{Q}$ with stable poles, as demonstrated in [15]. Moreover, since the fitting of $\mathbf{H}$ and $\mathbf{Y_c}$ is performed in the modal domain, the off-diagonal elements corresponding to the $\mathbf{H}$ and $\mathbf{Y_c}$ matrices in the phase domain cannot be

properly fitted. Although the off-diagonal elements of **H** and **Y$_c$** are of very small magnitude, their poor fitting may have an observable impact in induced transient voltages. To evaluate the fitting precision of the FDQ model, the 12-conductor cable system of Figure 2.20 (data listed in Table 2.2) is considered. Figure 2.21 shows the magnitude of the diagonal entries of **H** and **Y$_c$**. Figure 2.22 shows the magnitude of two off-diagonal elements (similar results are obtained with other entries). In both Figure 2.21 and Figure 2.22 blue solid lines correspond to actual data and red dashed lines correspond to entries fitted with FDQ model. It can be observed that diagonal elements are fitted with acceptable accuracy, while off-diagonal elements are poorly fitted.
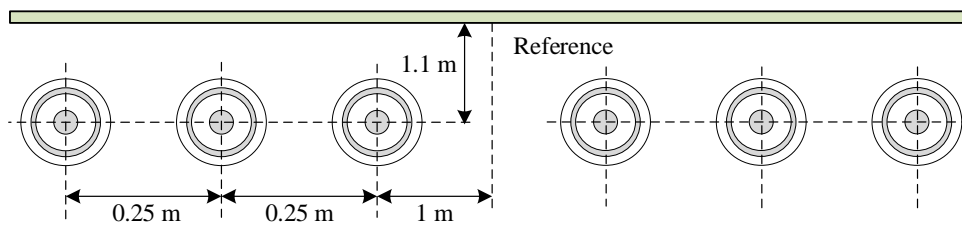
Figure 2.20 Underground cable system of 1 km, 6 phases and 12 conductors

Table 2.2 Cable data for the system of Figure 2.20

Inner-Outer Radius of the Core	3.175-12.54 mm
Inner-Outer Radius of the Sheath	22.735-26.225 mm
Outer Insulation Radius	29.335 mm
Resistivity of Sheath	2.1×10^{-7} Ohm-m
Resistivity of Core	1.7×10^{-8} Ohm-m
Core Insulator Relative Permittivity	3.5
Shield Insulator Relative Permittivity	2.0
Insulation Loss Factor	0.001
Earth Resistivity	250 Ohm-m

(a)   (b)
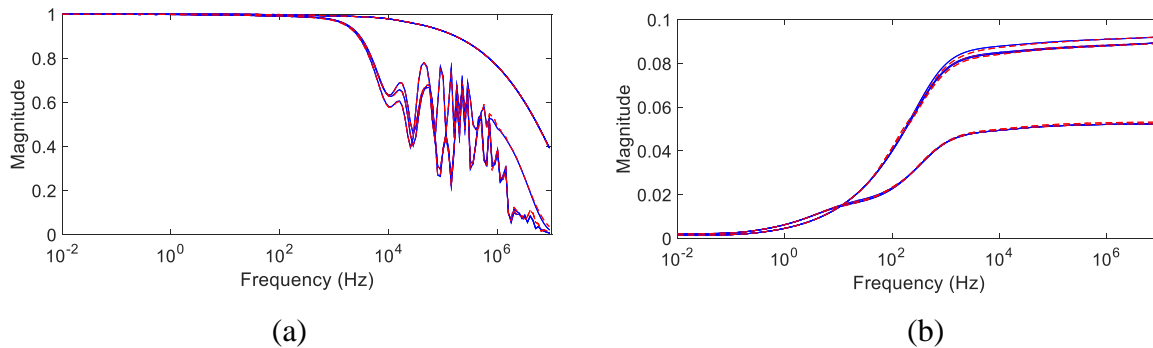
Figure 2.21 Magnitude of diagonal entries of the (a) **H**, and (b) **Y$_c$** matrices.
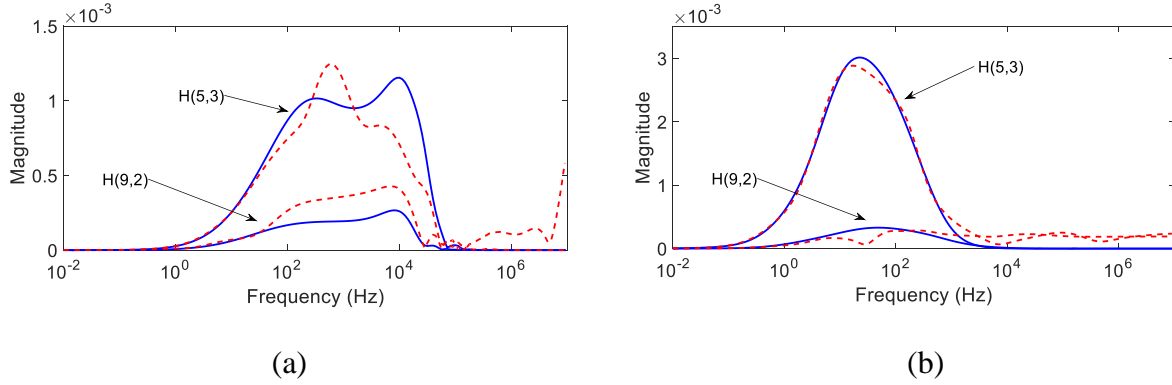
Figure 2.22 Magnitude of off-diagonal entries of the (a) $\mathbf{H}$, and (b) $\mathbf{Y_c}$ matrices.

For a time-domain simulation, the configuration of Figure 2.23 is considered. The cores of the first three conductors of the cable system of Figure 2.20 are excited with a step unit voltage at $t = 0$. Figure 2.24 compares the transient voltages given by FDQ, ULM using a two-step interpolation scheme [37], and NLT methods at the receiving end of the first core, i.e. V_1. Figure 2.25 shows the induced voltage at the receiving end of the fourth conductor V_7. Regarding the induced voltage, Figure 2.25 shows a significant deviation between FDQ model compared to the NLT and ULM solutions.
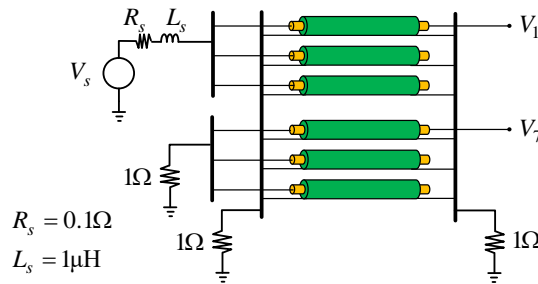
Figure 2.23 Network configuration for example 5
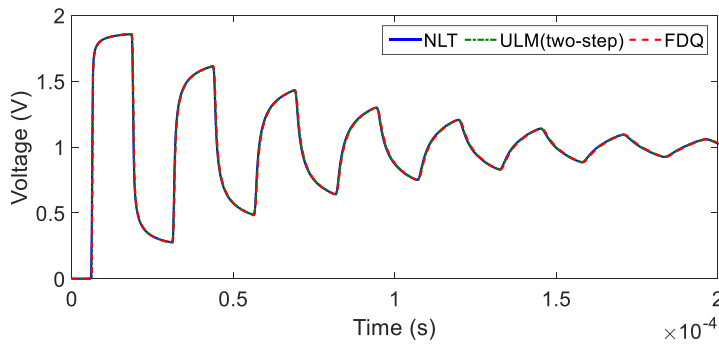
Figure 2.24 Voltage at the receiving end of the first core, V_1
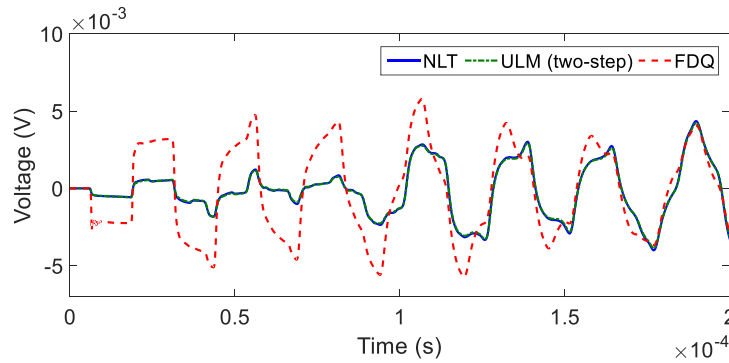
Figure 2.25 Voltage at the receiving end of the fourth core, V_7

2.4.3 Instabilities in the ULM

The ULM involves a two-step fitting approach. In the first step, the poles of $\mathbf{H}$ are identified in the modal domain together with time delays; in the second step, the residues are calculated in the phase domain. The ULM has been implemented in EMT-type programs and considered an accurate model for both transmission lines and cables. However, it has been associated with numerical stability problems [36]-[39] due to the existence of residue/pole pairs with large ratios and opposite signs coming from different but close delay groups. This is denoted as unbalanced modal contributions and it results in magnification of integration errors in time-domain simulations. The simulation of Figure 2.23 is now performed with ULM using the classic single-step integration scheme. The result corresponding to V_1 is shown in Figure 2.26. It can be observed that the simulation obtained with ULM numerically explodes due to roundoff errors. The maximum residue/pole ratio in the approximation of $\mathbf{H}$ is 9128.4.
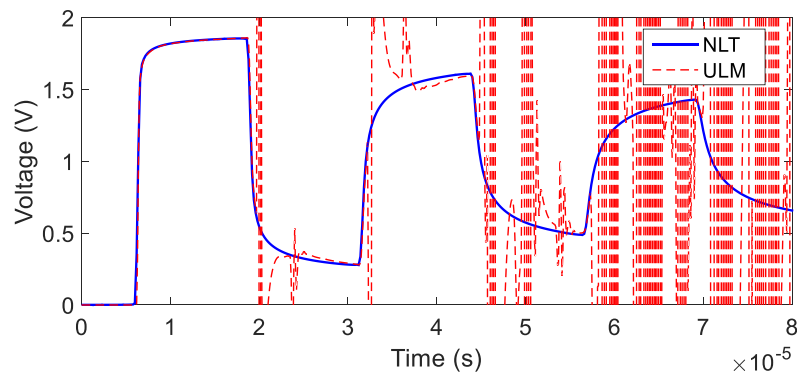
Figure 2.26 Voltage at the receiving end of the fourth core, V_1, using the ULM approach

Adapting more accurate integration schemes and a two-step interpolation technique, as proposed in [37], reduces integration errors and helps maintaining numerical stability in the time domain, as observed in Figure 2.24 and Figure 2.25. However, the unbalanced modal contributions in **H** cannot be removed by changing the integration method, and as it will be demonstrated in Chapter 4, inaccurate simulation results with spurious oscillations can still be observed in cases with very large residue/pole ratios.

2.4.4 Inaccuracies when fitting H in the phase domain

When fitting the modal contributions of **H** individually in the phase domain, as in (2.25), some off-diagonal entries of **H** may not be accurately fitted with a regular VF procedure. This is basically due to the significant difference in magnitude between the diagonal and off-diagonal elements of **H**, as demonstrated in the following example.

For the cable system of Figure 2.20, there are 7 distinct modal contribution functions after grouping. Each one is fitted with 25 poles. According to Figure 2.27, the diagonal elements of **H** are accurately fitted (Figure 2.27a); however, the fitting of the off-diagonal entries (5,7) and (7,9) is oscillatory (Figure 2.27b). This is due to significant difference in magnitude between the entries of **H**, which are attempted to be fitted simultaneously using the same set of poles to accelerate time domain simulations. Although, the off-diagonal elements of **H** are smaller, their poor fitting may have an observable impact on induced voltages, as will be shown in Chapter 4.
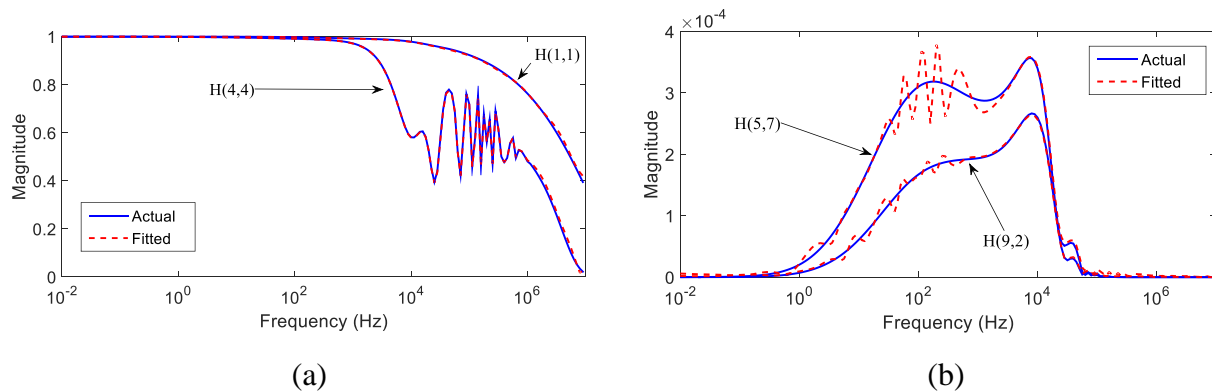
Figure 2.27 Magnitude of (a) two diagonal and (b) two off-diagonal entries of **H**

Idempotent models also perform fitting through decomposition [24] but the non-smooth behavior associated with similar eigenvalues was overlooked. Moreover, it divides modal contributions

into eigenvalues and idempotent matrices which can reduce the efficiency of models due to cascaded convolutions in the time domain.

2.5 Conclusions

The chapter presented a review and a comparison of the most predominant line models used for EMT simulations. First, the basic line modeling theory, including main line equations, is provided. Then, various cases of study are used to evaluate the performance of the most common line models in time-domain simulations. It is shown that frequency-dependent models are required to achieve accurate results in transient analysis. It is verified that phase-domain based models provide highly accurate results for the simulation of coupling effects between parallel conductors, compared to modal-domain based models. In addition, the drawbacks of phase-domain models are demonstrated trough the simulation of practical cases.

The line and cable models currently implemented in EMTP are used in this chapter. For verification purposes, the simulation result obtained with the numerical Laplace transform technique, is considered as reference solution.

CHAPTER 3   ENHANCED FITTING TECHNIQUES FOR THE IDENTIFICATION OF THE PROPAGATION FUNCTION

It has been verified in Chapter 2 that phase domain models provide highly accurate results in EMT analysis. However, fitting the line/cable functions in the phase domain is not straightforward, particularly in the case of the propagation function $\mathbf{H}$, due to multiple time delays. The ULM has been associated with numerical stability problems due to the existence of residue/pole pairs with high ratios and opposite signs coming from different but close delay groups. Moreover, this approach often leads to incorrect solutions for the DC steady-state voltages and currents due to generally poor DC fitting. On the other hand, when fitting the modal contributions of $\mathbf{H}$ individually in the phase domain, some off-diagonal entries may not be accurately fitted with a regular VF procedure.

This chapter contributes with two improved identification procedures of $\mathbf{H}$ in the phase domain for wideband (WB) models. The first procedure encapsulates: Frequency partition and adaptive weighting techniques to ensure the precision of fitting, and a model order reduction method via balanced realization to obtain a reduced order of approximation. The second procedure includes a DC correction step in the fitting process for improving the precision of DC response of the model. Both methodologies are illustrated via numerical examples. The impact of improving the fitting of $\mathbf{H}$ in time-domain simulations will be analyzed via transient studies in Chapter 4.

3.1 Accurate identification of H in the phase domain

One of the main contributions of this thesis is the proposal of an improved fitting in three steps: i) normalization of all entries of $\mathbf{H}$ via a weighting technique prior to fitting, and ii) frequency partitioning. Since frequency partitioning generally increases the number of poles, iii) a model order reduction (MOR) technique via balanced realization (BR) is applied to obtain a reduced order of approximation [55].

3.1.1 Adaptive weighting technique

It is proposed to normalize all entries of $\mathbf{H}$ prior to fitting and assign a weighting value σ for the elements whose magnitude is smaller than a predefined threshold value. Therefore, the ith modal contribution group in (2.25) is normalized as:

$$\hat{\mathbf{H}}'_i(n,m) = W\hat{\mathbf{H}}_i(n,m) \tag{3.1}$$

where n and m correspond to its nth row, and its mth column, respectively, and W is the weighting function calculated as

$$W = \frac{\sigma}{\left\|\hat{\mathbf{H}}_i(n,m)\right\|} \tag{3.2}$$

where $\|\bullet\|$ denotes the 2-norm, and σ represents an adaptive weighting defined as

$$\sigma = \begin{cases} 1\times10^{+1} & \text{if} & \left|\hat{\mathbf{H}}_i(n,m)\right|_{\max} \geq 0.01 \\ 1\times10^{-2} & \text{if} & 0.001 \leq \left|\hat{\mathbf{H}}_i(n,m)\right|_{\max} < 0.01 \\ 1\times10^{-3} & \text{if} & \left|\hat{\mathbf{H}}_i(n,m)\right|_{\max} < 0.001 \end{cases} \tag{3.3}$$

Applying (3.1) to (3.3), the differences in magnitude between the elements of $\hat{\mathbf{H}}_i$ are reduced, and the residues $\mathbf{R}'_{i,j}$, and poles $p_{i,j}$ of $\hat{\mathbf{H}}'_i$ are calculated. This approach guarantees lower fitting errors for all entries. To recover the original $\hat{\mathbf{H}}_i$, the residues are compensated considering the same weighting function, i.e,

$$\mathbf{R}_{i,j}(n,m) = \frac{\mathbf{R}'_{i,j}(n,m)}{W} \tag{3.4}$$

3.1.2 Frequency partitioning approach

The fact that residues and poles are simultaneously identified in the phase domain allows to take advantage of frequency partitioning. It has been reported that partitioning of the frequency band improves fitting precision [52]-[54]. The downside is the increasing number of poles. In this thesis, a frequency partitioning approach using two sections is proposed for the fitting of $\hat{\mathbf{H}}'_i$, as seen in Figure 3.1. The fitting is followed by model order reduction. The main steps of the proposed approach are given as follows.

Step 1) A local rational approximation, $\tilde{\mathbf{H}}_{LF}$, is performed in a pre-defined low frequency (LF) range ω_{LF} (e.g. from 0.01 Hz to 100 Hz).

Step 2) A second rational approximation is performed onto an error function computed as:

$$\mathbf{E}(\omega) = \mathbf{H}(\omega) - \tilde{\mathbf{H}}_{LF}(\omega) \tag{3.5}$$

That is, $\mathbf{E}$ is given by the difference between $\tilde{\mathbf{H}}_{LF}$ and the original $\mathbf{H}$. The whole frequency range is considered for the evaluation of $\mathbf{E}$ whose fitting gives the second part of the approximation: $\tilde{\mathbf{H}}_{HF}$.

Step 3) The final approximation is obtained on $\omega_{LF} \cup \omega_{HF}$, by summing the local approximations, i.e.,

$$\hat{\mathbf{H}}'_i \approx \tilde{\mathbf{H}}_{LF} + \tilde{\mathbf{H}}_{HF} \tag{3.6}$$

where each local approximation is given by a set of partial fractions.

The final solution comprises all the poles and residues by both local approximations, i.e.,

$$\hat{\mathbf{H}}'_i \approx \sum_{j=1}^{N_T} \frac{\hat{\mathbf{R}}'_{i,j}}{s - \hat{p}_{i,j}} \tag{3.7}$$

where N_T is the number of total poles, and $\hat{\mathbf{R}}'_{i,j}$ and $\hat{p}_{i,j}$ are the combined residues and poles, respectively.
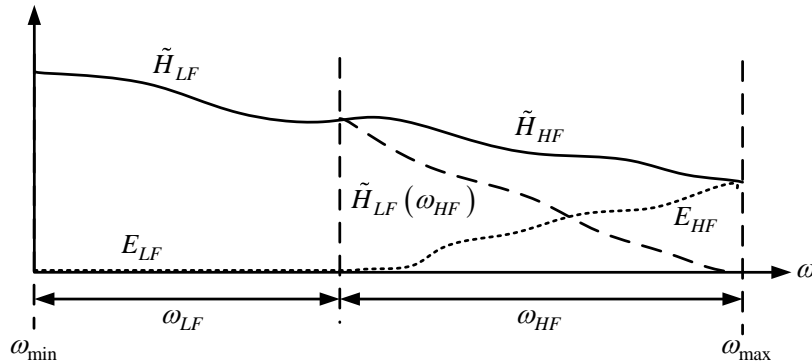
Figure 3.1 Illustration of the proposed frequency partitioning method for a given entry of $\mathbf{H}$

3.1.3 Model order reduction via balanced realization

In the proposed partitioned-based fitting approach, redundant poles are prone to appear when the local approximations are added up. To remove the redundant poles, a model order reduction

method is applied using the BR technique [55]. A state-space model with an order of N_T, (3.7) can be expressed as a linear-time-invariant system:

$$\dot{\mathbf{x}} = \mathbf{A}\mathbf{x} + \mathbf{B}\mathbf{u} \tag{3.8}$$

$$\mathbf{y} = \mathbf{C}\mathbf{x} \tag{3.9}$$

where $\mathbf{A}$ is a diagonal matrix containing the set of poles $\hat{p}$, $\mathbf{B}$ is a column vector of ones with a length equal to the number of entries of $\hat{\mathbf{H}}_i'$, and $\mathbf{C}$ corresponds to a matrix containing the residues. In (3.9), $\mathbf{C}$ is built with the entries (n,m) of $\hat{\mathbf{R}}$ sorted in a column-wise manner. Thus, $\mathbf{C}$ has the size of $(n \times m)$ by N_T. The BR transforms (3.8) and (3.9) into a *balanced* system where direct truncation can be applied to obtain the reduced rth order (with $r < N_T$) model ($\mathbf{A_r}$, $\mathbf{B_r}$, $\mathbf{C_r}$), given by

$$\dot{\mathbf{x}}_\mathbf{r} = \mathbf{A_r}\mathbf{x_r} + \mathbf{B_r}\mathbf{u} \tag{3.10}$$

$$\mathbf{y} = \mathbf{C_r}\mathbf{x_r} \tag{3.11}$$

Although BR produces a new set of poles, it is demonstrated in [55] that they are always stable. The Matlab functions of *balreal* and *modred* (from control system toolbox) are applied in this thesis for the implementation of the model order reduction (MOR) via BR. It is noted that a common set of poles is considered in each modal contribution matrix.

3.1.4 Numerical example

This section illustrates the performance of the three steps of the proposed fitting procedure through a numerical example.

Application of adaptive weighting

All the seven modal contribution groups of the cable system of Figure 2.20 are fitted either with 25 or 30 poles. Table 3.1 lists the rms errors associated with two different fitting approaches: using the vector fitting technique without weighting (labeled as VF) and using the vector fitting technique with the proposed weighting technique (labeled as WF). Figure 3.2 and Figure 3.3 show the fitting results for entries $(5,7)$ and $(9,2)$ obtained with 25 and 30 poles, respectively.

The use of the proposed WF reduces numerical oscillations observed in VF significantly. Figure 3.3 suggests that, despite increasing the number of poles, it is not possible to eliminate the oscillations by using VF.

Table 3.1 Fitting errors of the modal contribution groups of the cable system of Figure 2.20

Modal group	Rms fitting error (25 poles)		Rms fitting error (30 poles)	
	VF	WF	VF	WF
1	1.8225×10^{-5}	1.2264×10^{-5}	1.8474×10^{-5}	1.2087×10^{-5}
2	7.7694×10^{-5}	4.2056×10^{-5}	5.7211×10^{-5}	3.4560×10^{-5}
3	4.7448×10^{-4}	1.8314×10^{-5}	4.6718×10^{-4}	1.8214×10^{-4}
4	5.8099×10^{-4}	3.2009×10^{-4}	5.9657×10^{-4}	3.1869×10^{-4}
5	2.2000×10^{-3}	1.4000×10^{-3}	2.0000×10^{-3}	1.3000×10^{-3}
6	1.3000×10^{-3}	8.6142×10^{-4}	1.3000×10^{-3}	7.4263×10^{-4}
7	2.1000×10^{-3}	2.4543×10^{-4}	1.7000×10^{-3}	1.8579×10^{-4}
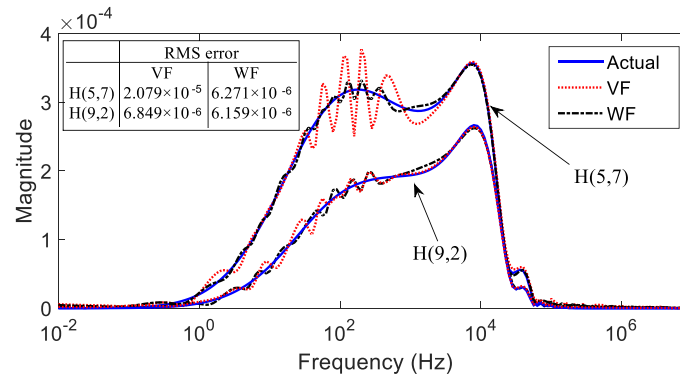
Figure 3.2 Magnitude of the $\mathbf{H}(5,7)$, and $\mathbf{H}(9,2)$ fitted with 25 poles
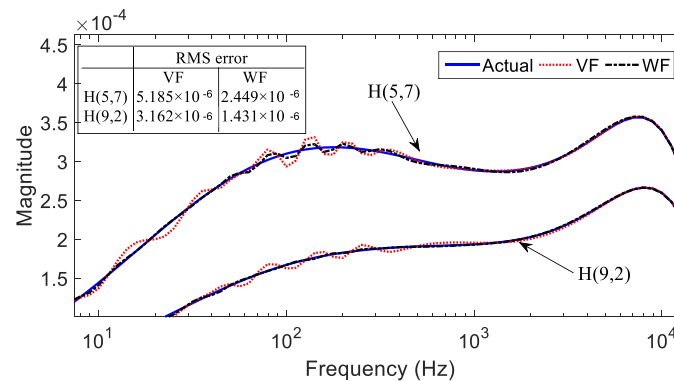
Figure 3.3 Magnitude of the $\mathbf{H}(5,7)$, and $\mathbf{H}(9,2)$ fitted with 30 poles

To further increase the fitting precision of the modal groups obtained with the WF approach, the frequency partitioning and MOR techniques are applied next.

Application of weighting, frequency partitioning, and model order reduction

Table 3.2 presents the fitting rms error of **H** for the cable system of Figure 2.20 using two different techniques a) proposed WF combined with frequency partitioning technique (labeled as WFP) and b) application of model order reduction (labeled WFP-MOR). The frequency range, predefined from 0.01 Hz to 10 MHz, is partitioned into two at 100 Hz. It is seen that the fitting errors are further reduced when frequency-partitioning technique is applied. Although this increases the number of poles due to the introduction of redundant poles (55 poles), the order of approximation is reduced without loss of accuracy by applying the proposed MOR since redundant poles are removed. The last column of Table 3.2 shows that a more accurate fitting is obtained with WFP-MOR using a smaller number of poles than VF. Figure 3.4 presents the fitting of $\mathbf{H}(5,7)$ using the VF and proposed WFP and WFP-MOR techniques. It is seen that the numerical oscillations are effectively eliminated by both proposed techniques.

Table 3.2 Fitting errors of the modal contribution groups of the cable system of Figure 2.20, considering the frequency partitioning approach

Modal group	Rms fitting error			
	WFP (55 poles)	WFP-MOR (30 poles)	WFP-MOR (25 poles)	WFP-MOR (20 poles)
1	1.2077×10^{-5}	1.2077×10^{-5}	1.2179×10^{-5}	1.4589×10^{-5}
2	3.3781×10^{-5}	3.3838×10^{-5}	3.5376×10^{-5}	1.0258×10^{-4}
3	1.8035×10^{-5}	1.8035×10^{-4}	1.8032×10^{-4}	1.8114×10^{-4}
4	3.0937×10^{-4}	3.0937×10^{-4}	3.0940×10^{-4}	3.0967×10^{-4}
5	1.1000×10^{-3}	1.1000×10^{-3}	1.1000×10^{-3}	1.1000×10^{-3}
6	7.4020×10^{-4}	7.4021×10^{-4}	7.4038×10^{-4}	7.4188×10^{-4}
7	1.5601×10^{-4}	1.5623×10^{-4}	1.5966×10^{-4}	2.0670×10^{-4}
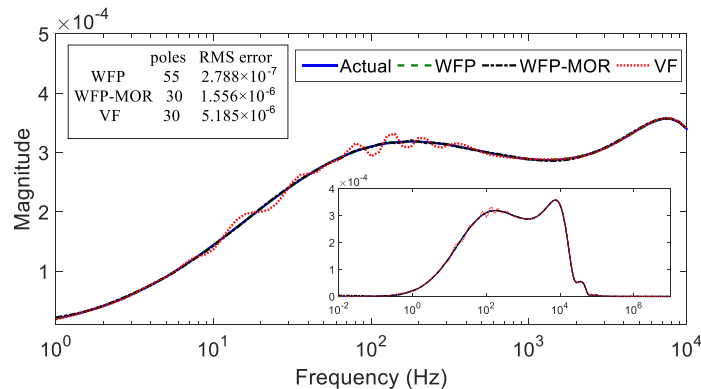
Figure 3.4 Magnitude of entry $\mathbf{H}(5,7)$ refer to Table 3.2 for rms fitting errors

3.2 DC correction

This section contributes by extending the fitting approach of FDCM to transmission lines using a two-stage fitting method in which low frequency samples are given special attention. In the first step, the fitting is performed by excluding very low frequency samples such as those below 1 Hz. In second step, a correction function is found for the excluded low frequency samples. Partitioning and reduced frequency range helps avoiding pairs with large residue pole ratios with the classic ULM approach. The proposed new approach is called FDM (Frequency Dependent Model) with DC correction, i.e., FDM/DC, and it can be also applied to cables or combined with the classic ULM to improve low frequency fitting when necessary.

3.2.1 FDM/DC approach

To increase the precision in the fitting of $\mathbf{H}$ at frequencies close to DC, a two-stage fitting method is proposed. In the proposed approach, the frequency band is partitioned to relax fitting, and a correction term is found afterward.

In the proposed FDM/DC, the propagation function $\mathbf{H}$ is fitted as follows (see Figure 3.5):

Step 1) Divide the frequency range: low frequency (LF) section (e.g., 0.001 to 1 Hz) and high frequency (HF) section (e.g., 1 Hz to 1 MHz).

Step 2) Perform fitting at the HF section to obtain $\tilde{\mathbf{H}}_{HF}$ (poles and residues). The rational approximation can be obtained by using either the FDCM or ULM approach.

$$\tilde{\mathbf{H}}_{HF} \cong \sum_{i=1}^{N_{gr}} \left(\sum_{m=1}^{M_i} \frac{\mathbf{R}_{i,m}}{s_{HF} - p_{i,m}} e^{\left(-s_{HF}\tau_i\right)} \right) \tag{3.12}$$

where $s_{HF} = j\omega_{HF}$, N_{gr} is the number of modal propagation groups, M_i is the order of the approximation for the ith modal group, $p_{i,m}$ represents its mth pole, $\mathbf{R}_{i,m}$ corresponds to a matrix of residues, and τ_i is the time delay associated with the ith modal group.

Step 3) Evaluate the fitted propagation function $\tilde{\mathbf{H}}_{HF}$ at the LF section. Then calculate the error of fitting at this section, $\Delta\mathbf{H}_{LF}$. The error function is calculated as the difference between the analytical $\mathbf{H}_{LF}$, and the fitted $\tilde{\mathbf{H}}_{LF}$ propagation function.

$$\Delta\mathbf{H}_{LF} = \mathbf{H}_{LF} - \tilde{\mathbf{H}}_{HF}\left(s_{LF}\right) = \mathbf{H}_{LF} - \tilde{\mathbf{H}}_{LF} \tag{3.13}$$

where $s_{LF} = j\omega_{LF}$.

Step 4) Obtain a rational function approximation, $\Delta\tilde{\mathbf{H}}_{LF}$, for $\Delta\mathbf{H}_{LF}$. In the LF range, the propagation function behaves flat and the impact of time delay is negligible; thus, an arbitrary time delay can be removed prior to fitting. It is proposed to use the delay associated to the first modal group, i.e., τ_1, (labelled as delay 1 assuming that delays are sorted). Then, $\Delta\tilde{\mathbf{H}}_{LF}$ is computed as follows

$$\Delta\tilde{\mathbf{H}}_{LF} \cong \sum_{k=1}^{M_{DC}} \frac{\mathbf{R}_{DC,k}}{s_{LF} - p_{DC,k}} e^{\left(-s_{LF}\tau_1\right)} \tag{3.14}$$

where M_{DC} is the order of approximation, and $\mathbf{R}_{DC}$ and p_{DC} are respectively the residues and poles obtained at the LF section, i.e. the DC correction terms.

Step 5) Obtain the final fitted function by combining the fitted functions given by (3.12) and (3.14):

$$\mathbf{H} \approx \tilde{\mathbf{H}}_{HF} + \Delta\tilde{\mathbf{H}}_{LF} \tag{3.15}$$

In this step, the DC correction terms in (3.14) are added to the first group in (3.12). Thus, the first modal group $\tilde{\mathbf{H}}_1$ is now obtained as

$$\tilde{\mathbf{H}}_1 = \left(\sum_{m=1}^{M_1} \frac{\mathbf{R}_{1,m}}{s - p_{1,m}} + \sum_{k=1}^{M_{DC}} \frac{\mathbf{R}_{DC,m}}{s - p_{DC,m}} \right) e^{\left(-s\tau_1\right)} \tag{3.16}$$

and the final propagation function is given by

$$\mathbf{H} \approx \tilde{\mathbf{H}}_1 + \sum_{i=2}^{N_{gr}} \left(\sum_{m=1}^{M_i} \frac{\mathbf{R}_{i,m}}{s - p_{i,m}} e^{\left(-s\tau_i\right)} \right) \tag{3.17}$$
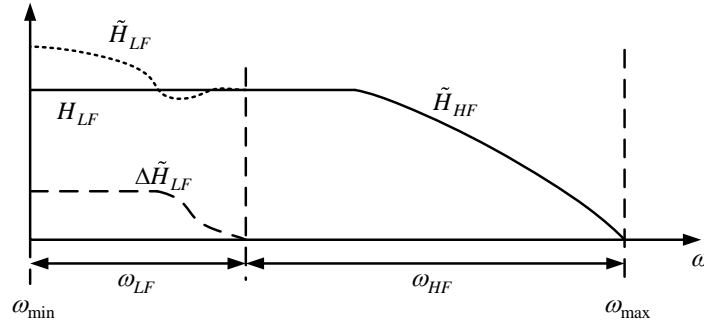
Figure 3.5 Illustration of the FDM/DC approach for one entry of **H**

The approach detailed above allows achieving more accurate fitting at low frequencies. Moreover, the partitioning and reduced frequency ranges help avoiding pairs with large residue pole ratios and consequently avoiding numerical instabilities that may occur in the classic implementation of ULM, regardless of the integration method. The FDM/DC approach is verified via a numerical example next.

3.2.2 Numerical example

This example considers a system involving 220-km AC and DC transmission lines running in parallel with 80 m separation from each other, see Figure 3.6. For this system, **H** is fitted with the proposed FDM/DC method and compared the ULM approach. Table 3.3 shows the corresponding fitting data considering 20 samples per decade and a convergence tolerance of 0.0001 in the fitting process. In the first stage of the FDM/DC, **H** is fitted from 1 Hz to either 10^5 or 10^6 Hz. Then, the error at the LF section is fitted using 8 poles from 0.001 Hz to 1 Hz. It is mentioned that fitting up to 10^6 Hz results very similar to the one up to 10^5 Hz, even with a smaller residue/pole ratio (see Table 3.3). The approximation of $\Delta\mathbf{H}_{LF}$ is shown in Figure 3.7. It is observed that deviations of magnitudes are acceptable. The magnitudes of the final approximation for the elements of the first column of **H** for the entire frequency range are shown in Figure 3.8. It is observed that all the elements are accurately fitted. In ULM, the fitting of **H** is performed in a single range of frequencies using four different ranges of frequency (see Table 3.3). It is noticed in Table 3.3 that a very large residue/pole ratio results when the frequency range is increased to 8 decades in the ULM, i.e. from 0.001 Hz to 10^5 Hz, and from 0.01 Hz to 10^6 Hz. Moreover, more poles are required with ULM compared to the FDM/DC technique.
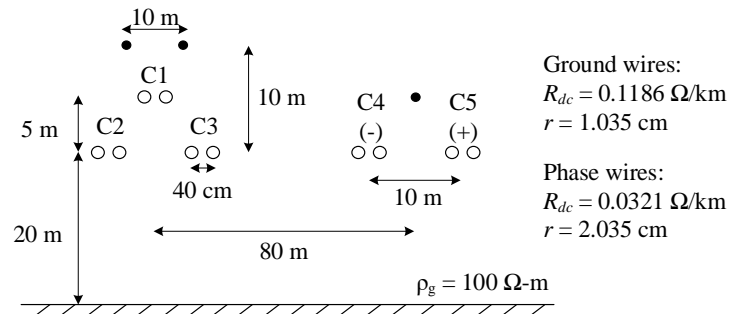
Figure 3.6 AC/DC lines geometry

Table 3.3 Fitting data of the system of Figure 3.6

Model	F_{min} (Hz)	F_{max} (Hz)	No. poles (total)	Max. r/p ratio
FDM/DC	0.001	10^5	32	25.23
	0.001	10^6	32	1.46
ULM	0.100	10^5	34	5.17
	0.010	10^5	37	3.85
	0.001	10^5	80	426226.24
	0.010	10^6	100	1633120.74
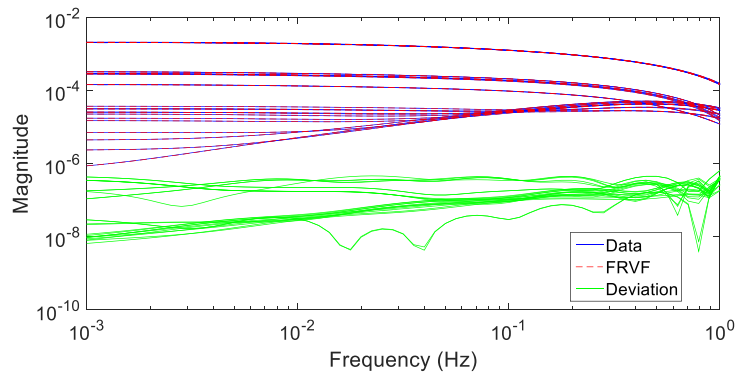
Figure 3.7 Low-frequency approximation of function error for $\Delta\mathbf{H}_{LF}$
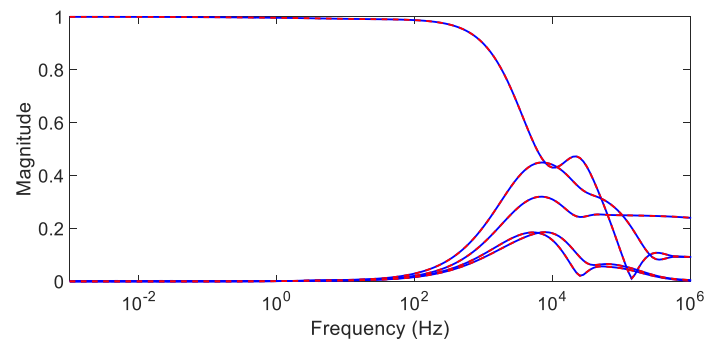
Figure 3.8 Magnitude of the first column of $\mathbf{H}$. Solid line corresponds to actual values while dashed lines corresponds to fitted values with FDM/DC

3.3 Conclusions

This chapter presented two fitting procedures to obtain an accurate identification of the propagation function of cables and lines while maintaining reduced order of approximation. In the first procedure, frequency-domain partitioning and adaptive weighting techniques are directly applied in the phase domain for the identification of poles and residues simultaneously to ensure the precision of fitting of all entries including the low-magnitude off-diagonal elements. The order of approximation is reduced by post-processing the fitting using the balanced realization technique.

In the second procedure, the fitting approach of FDCM is extended to transmission lines by using a two-stage fitting method in which low frequency samples are given special attention. The fitting is performed in a two-stage fashion ensuring precise fitting primarily at frequencies near DC. This approach complements the prevailing universal line model by avoiding pairs with large residue pole ratios, and by improving low frequency fitting when necessary.

The accuracy of the proposed methodology is demonstrated via numerical examples.

CHAPTER 4   TIME DOMAIN ANALYSIS

This chapter describes the time-domain implementation details of the wideband line/cable model used in this thesis. The impact of improving the fitting of **H** in time-domain simulations is analyzed via transient studies. The methodologies proposed in Chapter 3 lead to more accurate fitting and, when combined with precise integration schemes, provide stable and more accurate time-domain simulations. This chapter also demonstrates the advantages for accurately computing DC steady-state waveforms and preserving numerical stability.

4.1 Time domain implementation

For the implementation of wideband models in EMT-type programs, the classic one-step integration scheme using the trapezoidal method proposed in [27] remains as the most accepted. However, it has been associated with numerical stability problems [36], [37], [39], [70].

In this thesis, the discrete form of time domain convolutions is obtained by assuming that the input is piece-wise linear [76]. In addition, the method in [37] proposed to reduce integration and interpolation errors by evaluating the convolutions associated with **H** in two steps as a function of the delay, is tested.

4.1.1 Discrete convolution

For the implementation of a phase-domain based model, the frequency-domain line equations are transformed to the time domain by using the convolution principle [9], expressed here as

$$X(s) = A(s)U(s) \Leftrightarrow x(t) = a(t) * u(t) = \int_0^\infty a(T)u(t-T)dT \tag{4.1}$$

The integral of (4.1) can be efficiently evaluated using recursive convolution if $a(T)$ is an exponential of the form re^{-pt}. This is achieved by using the partial fraction expansion of a rational function to represent $A(s)$ in the frequency domain. Considering that $A = r/(s+p)$, the convolution integral in (4.1) becomes:

$$x(t) = r \int_0^\infty e^{-p(T)} u(t-T)dT \tag{4.2}$$

As shown in [9], for a single time-step Δt (4.2) yields

$$x(t+\Delta t) = e^{-p\Delta t} x(t) + r \int_0^{\Delta t} e^{-p(T)} u(t+\Delta t - T) dT \qquad (4.3)$$

Since the term $x(t+\Delta t)$ is found from $x(t)$ with a simple integration over one single time step, (4.3) becomes a recursive process. If the input in (4.3) is assumed to vary linearly during the time step [76], it can be taken outside the integral which can then be determined analytically, i.e.,

$$x(t+\Delta t) = e^{-p\Delta t} x(t) + \frac{r}{p}\left(1 - \frac{1-e^{-p\Delta t}}{p\Delta t}\right) u(t+\Delta t) + \frac{r}{p}\left(\frac{1-e^{-p\Delta t}}{p\Delta t} - e^{-p\Delta t}\right) u(t) \qquad (4.4)$$

Alternatively, applying the trapezoidal rule of integration to (4.3) yields

$$x(t+\Delta t) = \frac{(2-p\Delta t)}{(2+p\Delta t)} x(t) + r \frac{p\Delta t}{(2+p\Delta t)}\left(u(t+\Delta t) + u(t)\right) \qquad (4.5)$$

4.1.2 Discrete state-space form of the characteristic admittance convolution

Considering terminal $\mathbf{k}$ of the cable system in Figure 2.2, the frequency-domain realization, or rational representation, of the product $\mathbf{Y_c V_k}$ in (2.6) is given by

$$\mathbf{I_{sh_k}} = \mathbf{G_0 V_k} + \sum_{i=1}^{N_y} \mathbf{G}_i \mathbf{W}_i \qquad (4.6)$$

$$\mathbf{W}_i = \frac{1}{s - q_i} \mathbf{V_k} \qquad (4.7)$$

The corresponding discrete time-domain solution assuming that the input is piece-wise linear is given by [76]

$$\mathbf{w}_i(t+\Delta t) = \alpha_i \mathbf{w}_i(t) + \lambda_i \mathbf{v_k}(t+\Delta t) + \mu_i \mathbf{v_k}(t) \qquad (4.8)$$

where Δt is the integration step, and α_i, λ_i, and μ_i are the integration constants given by

$$\alpha_i = \exp(q_i \Delta t) \qquad (4.9)$$

$$\lambda_i = [\alpha_i - 1 - q_i \Delta t]\left(q_i^2 \Delta t^2\right)^{-1} \Delta t \qquad (4.10)$$

$$\mu_i = \left[\alpha_i\left(-1+q_i\Delta t\right)+1\right]\left(q_i^2\Delta t^2\right)^{-1}\Delta t \tag{4.11}$$

A change of variables is applied to reduce the number of arithmetic operations:

$$\mathbf{x}_{\mathbf{Yc_k}i}\left(t+\Delta t\right) = \alpha_i\mathbf{x}_{\mathbf{Yc_k}i}\left(t\right)+\mathbf{v_k}\left(t\right), \quad i:1\ldots N_y \tag{4.12}$$

$$\mathbf{i}_{\mathbf{sh_k}}\left(t+\Delta t\right) = \sum_{i=1}^{N_y}\mathbf{C}_i\mathbf{x}_{\mathbf{Yc_k}i}\left(t+\Delta t\right)+\mathbf{G}_{\mathbf{Yc}}\mathbf{v_k}\left(t+\Delta t\right) \tag{4.13}$$

where

$$\mathbf{C}_i = \left(\alpha_i\lambda_i+\mu_i\right)\mathbf{G}_i \tag{4.14}$$

$$\mathbf{G}_{\mathbf{Yc}} = \sum_{i=1}^{N_y}\mathbf{G}_i\lambda_i+\mathbf{G_0} \tag{4.15}$$

A similar set of equations can be obtained for terminal $\mathbf{m}$, i.e.,

$$\mathbf{x}_{\mathbf{Yc_m}i}\left(t+\Delta t\right) = \alpha_i\mathbf{x}_{\mathbf{Yc_m}i}\left(t\right)+\mathbf{v_m}\left(t\right), \quad i:1\ldots N_y \tag{4.16}$$

$$\mathbf{i}_{\mathbf{sh_m}}\left(t+\Delta t\right) = \sum_{i=1}^{N_y}\mathbf{C}_i\mathbf{x}_{\mathbf{Yc_m}i}\left(t+\Delta t\right)+\mathbf{G}_{\mathbf{Yc}}\mathbf{v_m}\left(t+\Delta t\right) \tag{4.17}$$

4.1.3 Discrete state-space form of the propagation function convolution

The frequency-domain realization, or rational representation, of the product $\mathbf{H}\left(\mathbf{I_m}+\mathbf{Y_c}\mathbf{V_m}\right)$ in (2.6) is given by

$$\mathbf{I_{ki}} = \sum_{i=1}^{N_{gr}}\sum_{j=1}^{M_i}\mathbf{R}_{i,j}\mathbf{X}_{\mathbf{k}i,j} \tag{4.18}$$

$$\mathbf{X}_{\mathbf{k}i,j} = \frac{1}{s-p_{i,j}}\mathbf{I_{mr}}e^{\left(-s\tau_i\right)} \tag{4.19}$$

Single-step integration scheme

Figure 4.1 shows the classic single-step integration path used to discretize (4.19). The integration step is defined as a function of the delay. Given that $n_i\Delta t < \tau_i < (n_i+1)\Delta t$, the time delay is

expressed as $\tau_i = n_i + \varepsilon_i \Delta t$, where n_i is an integer. Assuming that the input is piece-wise linear, the discretized form of (4.19) is given by

$$\mathbf{x_{ki,j}}(t+\Delta t) = \alpha_{i,j}\mathbf{x_{ki,j}}(t) + \lambda_{i,j}\mathbf{i_{mr}}(t+\Delta t - \tau_i) + \mu_{i,j}\mathbf{i_{mr}}(t-\tau_i) \tag{4.20}$$

where the integration constants are given by

$$\alpha_{i,j} = \exp(p_{i,j}\Delta t) \tag{4.21}$$

$$\lambda_{i,j} = \left[\alpha_{i,j} - 1 - p_{i,j}\Delta t\right]\left(p_{i,j}^2\Delta t^2\right)^{-1}\Delta t \tag{4.22}$$

$$\mu_{i,j} = \left[\alpha_{i,j}\left(-1 + p_{i,j}\Delta t\right) + 1\right]\left(p_{i,j}^2\Delta t^2\right)^{-1}\Delta t \tag{4.23}$$

In general, the time delay is not an integer multiple of the time step. Since the inputs, i.e. reflected currents $\mathbf{i_{mr}}$ in (4.20), are only available on the discrete time mesh, they need to be interpolated between the sampled points. Thus, the terms of the input $\mathbf{i_{mr}}$ are obtained with

$$\mathbf{i_{mr}}(t-\tau_i) = \mathbf{i_{mr}}(t-n_i\Delta t) + \varepsilon_i\Delta t\left[\mathbf{i_{mr}}(t-\Delta t - n_i\Delta t) - \mathbf{i_{mr}}(t-n_i\Delta t)\right] \tag{4.24}$$

$$\mathbf{i_{mr}}(t+\Delta t - \tau_i) = \mathbf{i_{mr}}(t+\Delta t - n_i\Delta t) + \varepsilon_i\Delta t\left[\mathbf{i_{mr}}(t-n_i\Delta t) - \mathbf{i_{mr}}(t+\Delta t - n_i\Delta t)\right] \tag{4.25}$$

The single integration scheme has been widely used in the classic implementation of the ULM in EMT-type programs [27]. However, this scheme has been associated with numerical stability problems in cases with the presence of high residue/pole ratios, due to the magnification of the traveling-wave interpolation errors in time domain simulations [32], [33], [35], [70].

Based on the above procedure, a similar set of equations can be obtained for terminal $\mathbf{m}$.
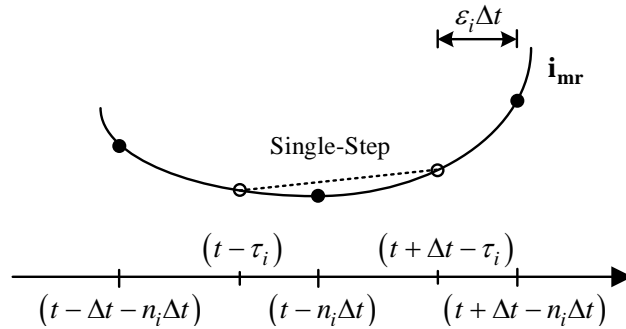
Figure 4.1 Single-step integration scheme

Two-step integration scheme

To alleviate integration and interpolation errors, a two-step integration technique [37] is applied to (4.19), see Figure 4.2. It should be noted that eliminating such errors is only possible under synthetic special conditions.
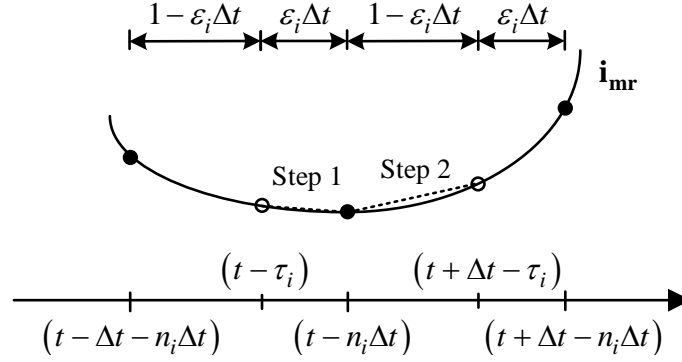
Figure 4.2 Two-step integration scheme

The integration steps depicted in Figure 4.2 are defined as a function of time delay as follows.

Step 1. Evaluate:

$$\mathbf{x}_{\mathbf{k}i,j}\left(t+\varepsilon_i\Delta t\right)=\alpha'_{i,j}\mathbf{x}_{\mathbf{k}i,j}\left(t\right)+\lambda'_{i,j}\mathbf{i}_{\mathbf{mr}}\left(t+\varepsilon_i\Delta t-\tau_i\right)+\mu'_{i,j}\mathbf{i}_{\mathbf{mr}}\left(t-\tau_i\right) \tag{4.26}$$

Step 2. Evaluate:

$$\mathbf{x}_{\mathbf{k}i,j}\left(t+\Delta t\right)=\alpha''_{i,j}\mathbf{x}_{\mathbf{k}i,j}\left(t+\varepsilon_i\Delta t\right)+\lambda''_{i,j}\mathbf{i}_{\mathbf{mr}}\left(t+\Delta t-\tau_i\right)+\mu''_{i,j}\mathbf{i}_{\mathbf{mr}}\left(t+\varepsilon_i\Delta t-\tau_i\right) \tag{4.27}$$

Finally, the solution from step 2 provides

$$\mathbf{i}_{\mathbf{ki}}\left(t+\Delta t\right)=\sum_{i=1}^{N_{gr}}\sum_{j=1}^{M_i}\mathbf{R}_{i,j}\mathbf{x}_{\mathbf{k}i,j}\left(t+\Delta t\right) \tag{4.28}$$

The discrete time-domain solution assumes that the input is piecewise linear. Defining $\hat{\varepsilon}_i=\left(n_i+1\right)\Delta t-\tau_i$, the coefficients in (4.26) and (4.27) are given as follows:

$$\alpha'_{i,j}=\exp\left(p_{i,j}\varepsilon_i\Delta t\right) \tag{4.29}$$

$$\lambda'_{i,j}=\left[\alpha'_{i,j}-1-p_{i,j}\varepsilon_i\Delta t\right]\left(p_{i,j}^2\varepsilon_i^2\Delta t^2\right)^{-1}\varepsilon_i\Delta t \tag{4.30}$$

$$\mu'_{i,j} = \left[\alpha'_{i,j}\left(-1+p_{i,j}\varepsilon_i\Delta t\right)+1\right]\left(p_{i,j}^2\varepsilon_i^2\Delta t^2\right)^{-1}\varepsilon_i\Delta t \tag{4.31}$$

$$\alpha''_{i,j} = \exp\left(p_{i,j}\hat{\varepsilon}_i\Delta t\right) \tag{4.32}$$

$$\lambda''_{i,j} = \left[\alpha''_{i,j}-1-p_{i,j}\hat{\varepsilon}_i\Delta t\right]\left(p_{i,j}^2\hat{\varepsilon}_i^2\Delta t^2\right)^{-1}\hat{\varepsilon}_i\Delta t \tag{4.33}$$

$$\mu''_{i,j} = \left[\alpha''_{i,j}\left(-1+p_{i,j}\hat{\varepsilon}_i\Delta t\right)+1\right]\left(p_{i,j}^2\hat{\varepsilon}_i^2\Delta t^2\right)^{-1}\hat{\varepsilon}_i\Delta t \tag{4.34}$$

Note that the term $\left(t+\varepsilon_i\Delta t-\tau_i\right)$ is on the time mesh while $\left(t-\tau_i\right)$ and $\left(t+\Delta t-\tau_i\right)$ are not (see Figure 4.2). Thus, these two last points are interpolated between the sampled points. The values of the input at $\left(t-\tau_i\right)$ and $\left(t+\Delta t-\tau_i\right)$ are obtained with (4.24) and (4.25), respectively.

A similar procedure is applied to obtain the set of equations for terminal **m**.

$$\mathbf{x}_{\mathbf{m}i,j}\left(t+\varepsilon_i\Delta t\right)=\alpha'_{i,j}\mathbf{x}_{\mathbf{m}i,j}\left(t\right)+\lambda'_{i,j}\mathbf{i}_{\mathbf{kr}}\left(t+\varepsilon_i\Delta t-\tau_i\right)+\mu'_{i,j}\mathbf{i}_{\mathbf{kr}}\left(t-\tau_i\right) \tag{4.35}$$

$$\mathbf{x}_{\mathbf{m}i,j}\left(t+\Delta t\right)=\alpha''_{i,j}\mathbf{x}_{\mathbf{m}i,j}\left(t+\varepsilon_i\Delta t\right)+\lambda''_{i,j}\mathbf{i}_{\mathbf{kr}}\left(t+\Delta t-\tau_i\right)+\mu''_{i,j}\mathbf{i}_{\mathbf{kr}}\left(t+\varepsilon_i\Delta t-\tau_i\right) \tag{4.36}$$

$$\mathbf{i}_{\mathbf{m}i}\left(t+\Delta t\right)=\sum_{i=1}^{N_{gr}}\sum_{j=1}^{M_i}\mathbf{R}_{i,j}\mathbf{x}_{\mathbf{m}i,j}\left(t+\Delta t\right) \tag{4.37}$$

4.1.4 Discrete line/cable model

The line/cable is represented by the Norton equivalent circuit shown in Figure 2.3, where:

$$\mathbf{i}_{\mathbf{k}}\left(t\right)=\mathbf{G}_{\mathbf{Y_c}}\mathbf{v}_{\mathbf{k}}\left(t\right)-\mathbf{i}_{\mathbf{hist_k}}\left(t\right) \tag{4.38}$$

$$\mathbf{i}_{\mathbf{m}}\left(t\right)=\mathbf{G}_{\mathbf{Y_c}}\mathbf{v}_{\mathbf{m}}\left(t\right)-\mathbf{i}_{\mathbf{hist_m}}\left(t\right) \tag{4.39}$$

where $\mathbf{G}_{\mathbf{Y_c}}$ is given by (4.15) and the history terms are computed as:

$$\mathbf{i}_{\mathbf{hist_k}}\left(t+\Delta t\right)=2\sum_{i=1}^{N_{gr}}\sum_{j=1}^{M_i}\mathbf{R}_{i,j}\mathbf{x}_{\mathbf{k}i,j}\left(t+\Delta t\right)-\sum_{i=1}^{N_y}\mathbf{C}_i\mathbf{x}_{\mathbf{Yc_k}i}\left(t+\Delta t\right) \tag{4.40}$$

$$\mathbf{i}_{\mathbf{hist_m}}\left(t+\Delta t\right)=2\sum_{i=1}^{N_{gr}}\sum_{j=1}^{M_i}\mathbf{R}_{i,j}\mathbf{x}_{\mathbf{m}i,j}\left(t+\Delta t\right)-\sum_{i=1}^{N_y}\mathbf{C}_i\mathbf{x}_{\mathbf{Yc_m}i}\left(t+\Delta t\right) \tag{4.41}$$

4.2 Case studies

This section illustrates the performance of the fitting procedures proposed in Chapter 3 through various cases. The impact of improving the fitting of **H** in time-domain simulations is analyzed via transient studies performed with different integration and interpolation schemes.

4.2.1 Case study 1: 12-Conductor Cable System

This section shows the impact of fitting precision in time domain simulations. For validation purposes, the numerical Laplace transform technique [2] is considered as the reference solution.

The transient simulations are performed using the models obtained with the fitting techniques presented in section 3.1.4. The time domain solution is obtained using the integration and two step interpolation methods mentioned in section 4.1.

This case study simulates the cable system of Figure 2.20. The first three cores are energized with a unit step voltage at $t = 0$ as seen in Figure 4.3. The simulation time step is 0.2 μs. Figure 4.4 shows the transient voltages at the receiving end, V_1, obtained with both the VF method and the proposed WFP-MOR technique. The reference Laplace solution is also provided for comparison purposes. Figure 4.5 shows the induced voltage at the receiving end of the fourth core, V_7. It is observed in Figure 4.5 that the difference between models becomes significant for induced voltage simulation. Figure 4.5 also implies that the proposed WFP-MOR approach is able to maintain accuracy with less number of poles compared to VF.
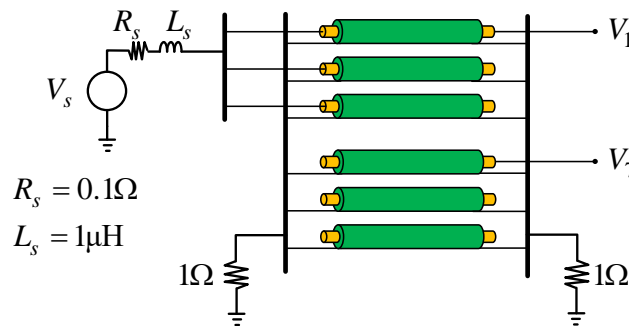
Figure 4.3 Case study 1, 12-conductor cable system
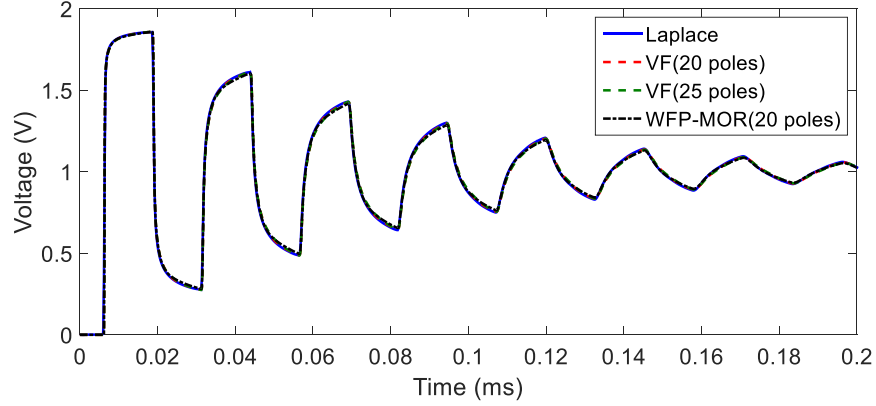
Figure 4.4 Voltage at the receiving end, V_1 in Figure 4.3
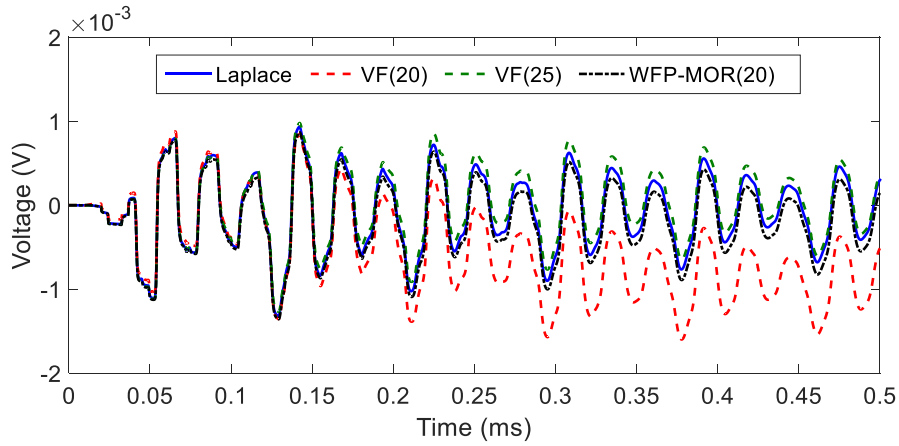
Figure 4.5 Induced voltage at the receiving end, V_7 in Figure 4.3

The simulation mentioned above is now performed by fitting **H** with the ULM approach. The time domain solution is also obtained using the integration and two-step interpolation techniques [37]. A portion of the result corresponding to V_1 is presented in Figure 4.6, together with the WFP-MOR solution. The simulation time step is 0.1 µs considering that the fastest time delay in the system is 6.24 µs. It is observed in Figure 4.6 that the proposed WFP-MOR provides a smooth simulation, while the ULM based solution shows inaccurate spurious oscillations. These inaccuracies are attributed to the amplification of integration errors due to large residue/pole ratios. The largest residue/pole ratio of **H** corresponding to the WFP-MOR and ULM models are 5.27, and 1.63×10^6, respectively.
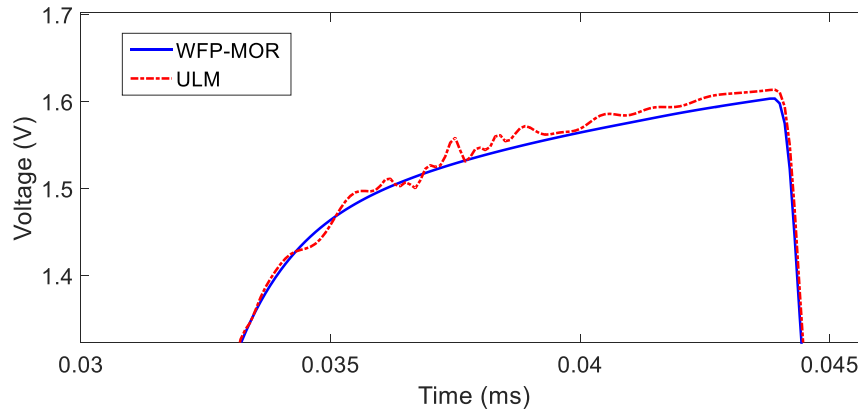
Figure 4.6 Comparison of the proposed WFP-MOR and ULM approaches

Table 4.1 lists residue-pole pairs with large ratios, associated to different but close modal groups. The existence of these pairs can potentially magnify the integration and/or interpolation errors. Figure 4.7 presents the simulation corresponding to Figure 4.6 using half time step. According to Figure 4.7, halving the time step does not decrease the numerical errors in the time domain, although the integration errors are supposed to be less. On the contrary, this suggests an increase of interpolation errors even though two-step interpolation scheme is used. Table 4.1 shows that, reflected currents associated with modal groups 5 and 6 arrive at the same time step, and opposing residue pole pairs compensate each other if the time step is 0.1 microseconds. However, if the step is halved, they arrive at different steps resulting in magnification of interpolation errors.

Table 4.1 Residue-pole pairs with large ratios obtained with ULM

Modal group	Time delay	Residue	Pole	Residue/Pole
3	23.52μs	2.2647×10^8	-1.5213×10^5	-1.4886×10^3
		8.3060×10^7	-3.8525×10^5	-2.1560×10^2
4	23.43μs	-2.1923×10^8	-1.6348×10^5	1.3410×10^3
		-1.6361×10^8	-4.7014×10^5	3.4801×10^2
5	19.72μs	1.1474×10^{12}	-7.1618×10^5	-1.6021×10^6
		-1.1680×10^{12}	-7.1774×10^5	1.6274×10^6
		3.6579×10^{10}	-2.7799×10^6	-1.3158×10^4
6	19.77μs	-1.3858×10^{10}	-7.2510×10^5	1.9112×10^4
		3.4060×10^{10}	-7.7837×10^5	-4.3758×10^4
		-2.9448×10^{10}	-2.6960×10^6	1.0923×10^4
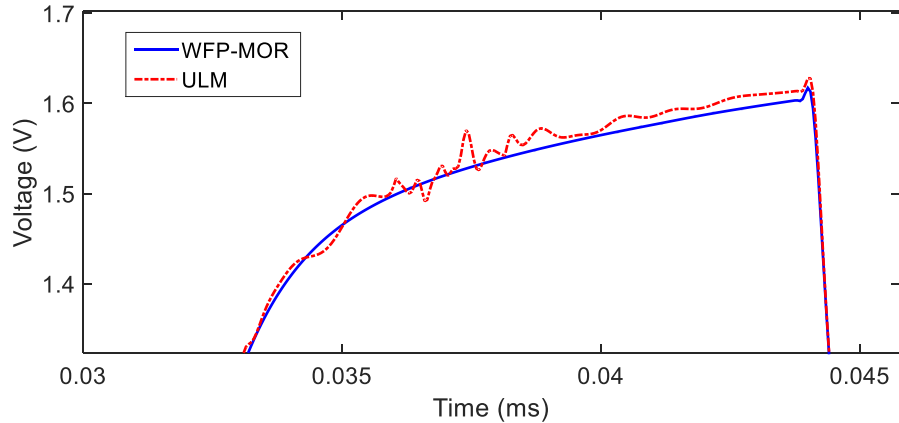
Figure 4.7 Comparison of the proposed WFP-MOR and ULM approaches, halved time step

4.2.2 Case study 2: A cable system running in parallel with a three-phase overhead transmission line

To see the impact of the fitting precision on the simulation of coupling effects between different conductors, the transmission system shown in Figure 4.8 is studied. The system consists of an underground cable system (data listed in Table 2.2) running in parallel with a three-phase overhead transmission line. The series impedance $\mathbf{Z}$ and shunt admittance $\mathbf{Y}$ parameters are computed using the cable and line constants available in EMTP [77]. These routines are based on [78]-[79]. Table 4.2 shows the fitting rms error obtained by fitting $\mathbf{H}$ with the VF, WFP, and WFP-MOR techniques. It is shown that the proposed WFP-MOR technique achieves a more accurate fitting than the VF for the same number of poles.
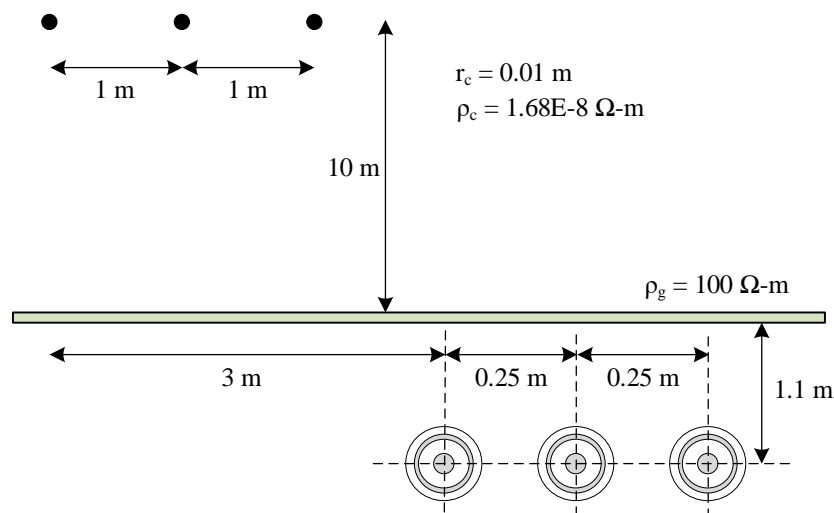
Figure 4.8 10-km transmission system layout for the case study 2

Table 4.2 Fitting errors of the modal groups of the system of Figure 4.8

Modal group	Rms fitting error		
	VF (14 poles)	WFP (45 poles)	WFP-MOR (14 poles)
1	$7.5041{\times}10^{-5}$	$1.6929{\times}10^{-5}$	$8.9846{\times}10^{-5}$
2	$7.9438{\times}10^{-4}$	$2.9702{\times}10^{-4}$	$4.5716{\times}10^{-4}$
3	$1.3000{\times}10^{-3}$	$9.0844{\times}10^{-5}$	$3.1303{\times}10^{-5}$
4	$4.6000{\times}10^{-3}$	$1.3000{\times}10^{-3}$	$1.3000{\times}10^{-3}$
5	$4.7000{\times}10^{-3}$	$8.3921{\times}10^{-4}$	$8.4135{\times}10^{-4}$
6	$1.2000{\times}10^{-3}$	$1.0713{\times}10^{-4}$	$7.7204{\times}10^{-4}$

For the evaluation of induced voltages, the test circuit of Figure 4.9 is considered. The source is a sinusoidal voltage source of 169 kV peak value and 60 Hz. Figure 4.10 shows the transient waveform of sheath voltage of phase-a at the receiving end considering the VF, WFP, and WFP-MOR techniques. These simulations are compared with the reference solution obtained using inverse numerical Laplace transform. It is observed that, some accuracy is lost when the number of poles is reduced to 14 with VF, whereas the proposed WFP-MOR method preserves precision. This becomes more evident in the induced voltage at the receiving end of the line, as shown in Figure 4.11.

Note that the proposed fitting WFP-MOR method allows modeling of challenging systems, such as the one of Figure 4.8, regardless of the integration technique. Figure 4.12 shows the core-voltage of phase-a at the receiving end of the cable in Figure 4.9 when **H** is fitted with the proposed WFP-MOR technique and the ULM approach. The time domain solution is obtained using a single-step integration scheme [27] considering a time-step of 10 μs. It is observed that the proposed WFP-MOR technique provides a stable solution whereas the simulation obtained by ULM method becomes unstable. The largest residue/pole ratio corresponding to WFP-MOR and ULM are 1.490 and $7.514{\times}10^{3}$, respectively.
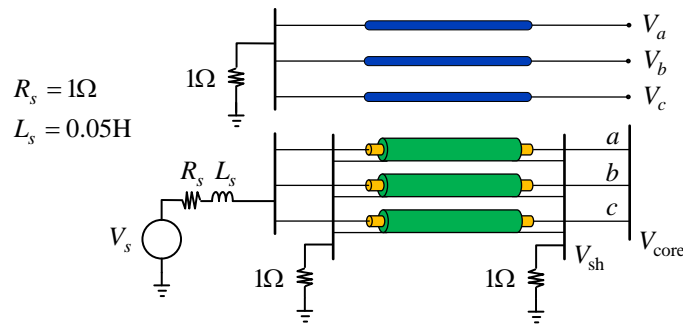
Figure 4.9 Test circuit for the case study 2
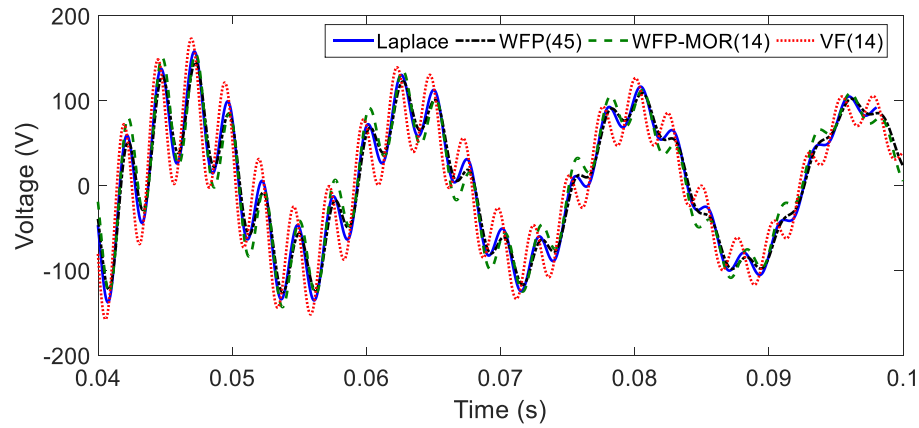
Figure 4.10 Sheath voltage on phase-a at the receiving end of the cable in Figure 4.9
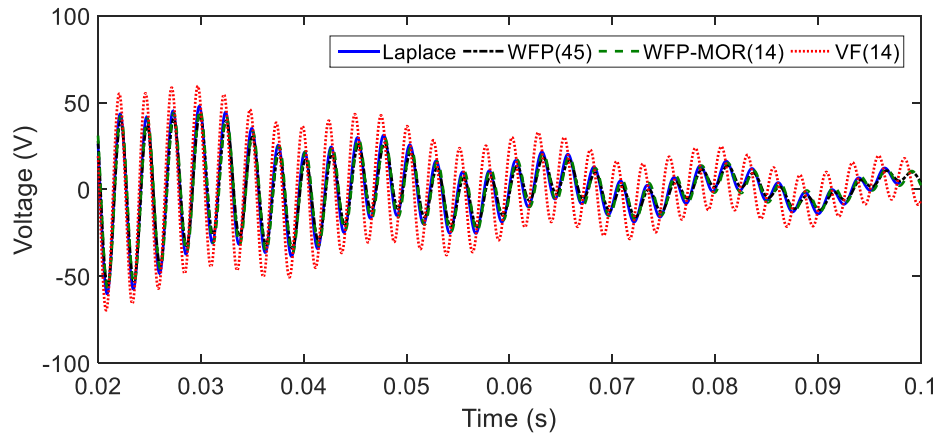
Figure 4.11 Induced-voltage on phase-a at the receiving end of the line in Figure 4.9
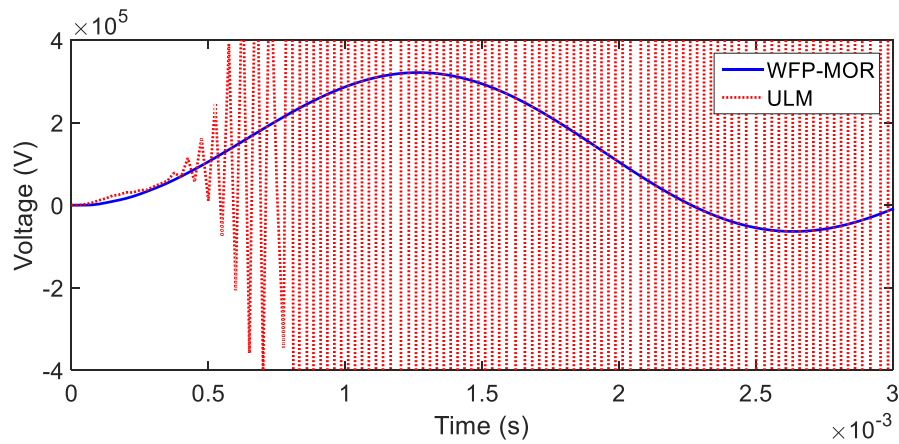
Figure 4.12 Core-voltage of phase-a at the receiving end of the cable in Figure 4.9

4.2.3 Case study 3: AC and DC lines in parallel

This case of study considers the numerical example shown in Section 3.2.2. The FDM/DC approach is verified in time domain simulations and compared against ULM using the classic single step integration scheme. The impact of improving the fitting of **H** at low frequencies in time-domain simulations is analyzed via transient studies.

The two circuit configurations of Figure 4.13 are used to test the system of Figure 3.6. In the first test (Figure 4.13a), a unit step current, with a ramping time of 0.5 s, is applied to the sending end of the positive conductor of the DC line, while the other conductors are grounded. Figure 4.14 shows the induced voltage at the receiving end of C2 considering four cases listed in Table 3.3. It is observed that the FDM/DC provides a stable and precise time-domain solution. On the other hand, and based on Table 3.3, two ULM cases using minimum frequency values of 0.1 Hz and 0.001 Hz deviate from the correct response. Hence, when using ULM, the computation of accurate DC response requires inclusion of very low frequencies in the fitting of **H**. Reducing the frequency range in ULM to 0.001 Hz results in large residue/pole ratios (see Table 3.3), leading to an unstable solution as shown in Figure 4.14. This problem is avoided in ULM by setting the minimum frequency for the fitting to 0.01 Hz. In this case, the time-domain response becomes stable and agrees with the solution obtained by the FDM/DC (Figure 4.14). However, the ULM requires five poles more than FDM/DC in the fitting of **H** (see Table 3.3).

Note that the maximum frequency needs to be adjusted in the ULM to provide accurate DC response. Such frequency is not known beforehand and implies a trial-and-error procedure for the common ULM user. On the contrary, the FDM/DC works well with either 10^5 Hz or 10^6 Hz as maximum fitting frequency.
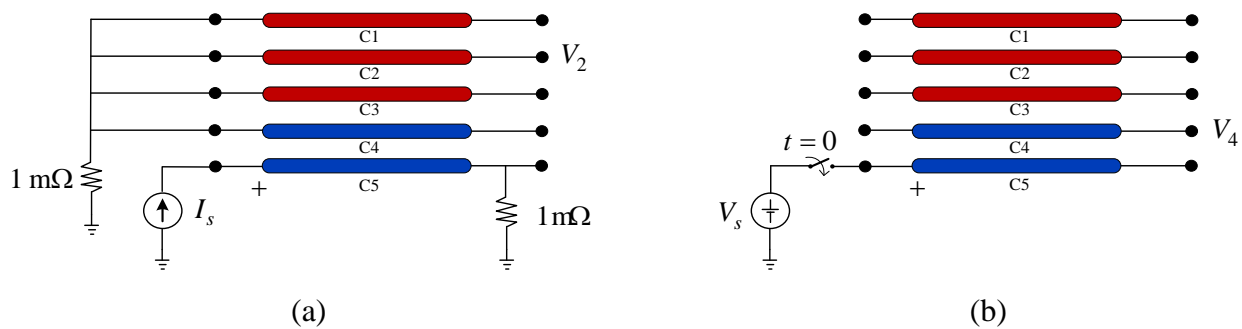
Figure 4.13 (a) short- and (b) open-circuit configuration for testing the AC/DC line
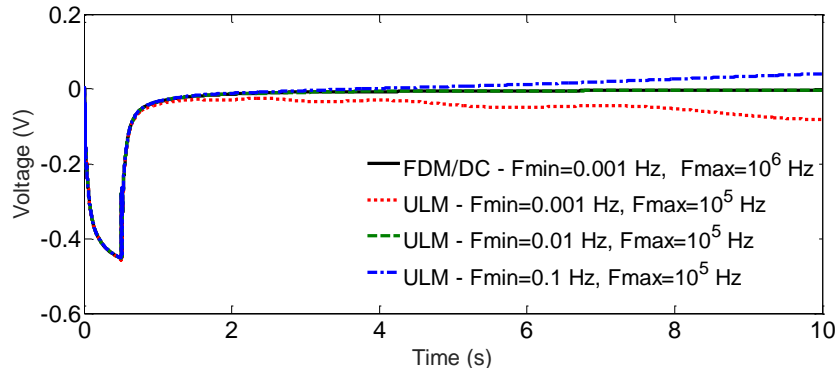
Figure 4.14 Time domain results of V_2 in Figure 4.13(a)

To analyze the performance of the proposed FDM/DC method under a fast front transient, the open-circuit configuration of Figure 4.13b is tested. In this second test, a step function is applied to the positive conductor (C5) at the sending end while the receiving end is open. Conductors C1-C4 are left open at both ends. Figure 4.15 shows the time-domain results of the induced voltage at the receiving end of C4, i.e. V_4. The minimum frequency for the fitting in FDM/DC and ULM is set to 0.001 Hz and 0.01 Hz, respectively. It is observed that FDM/DC provides accurate and stable solution regardless of the F_{max}, which confirms that the higher frequencies are also accurately simulated. It is noticed that ULM becomes unstable when the frequency range is extended to 1 MHz, despite the model in passive. The instability problem is due to the resulting very large residue/pole ratio in the fitting of $\mathbf{H}$ (see Table 3.3).
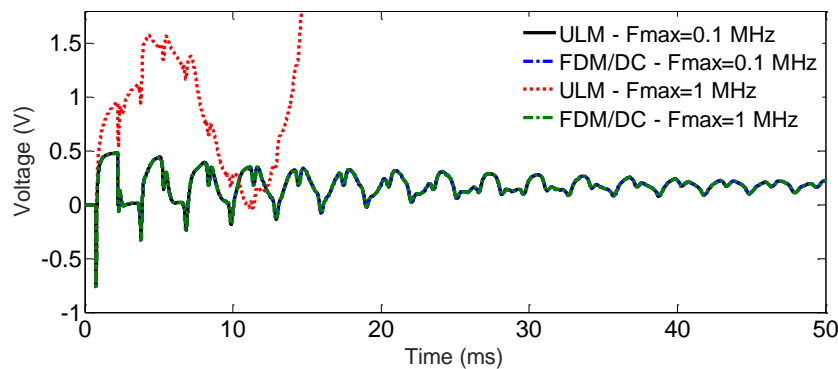
Figure 4.15 Time domain results of V_4 in Figure 4.13(b)

4.2.4 Case study 4: HVDC transmission system

This example aims at verifying the precision of FDM/DC and ULM models for computing DC steady-state waveforms via the time-domain simulation of a two-terminal HVDC transmission

system. Consider the system of Figure 4.16. The tower configuration and conductor details for both line segments are shown in Figure 4.17. The cable segment layout is shown in Figure 4.18 with data details in Table 4.3.

The HVDC system consists of a 27-km aerial line, 44-km cable, and 97-km aerial line segments. For the two aerial lines and the cable, $\mathbf{H}$ is fitted via the proposed FDM/DC approach. According to the first step of Section 3.2.1, $\mathbf{H}$ is fitted from 1 Hz to either 10^5 or 10^6 Hz using 12 poles per group. Then, the error function at the LF section is fitted using 8 poles from 0.001 Hz to 1 Hz.
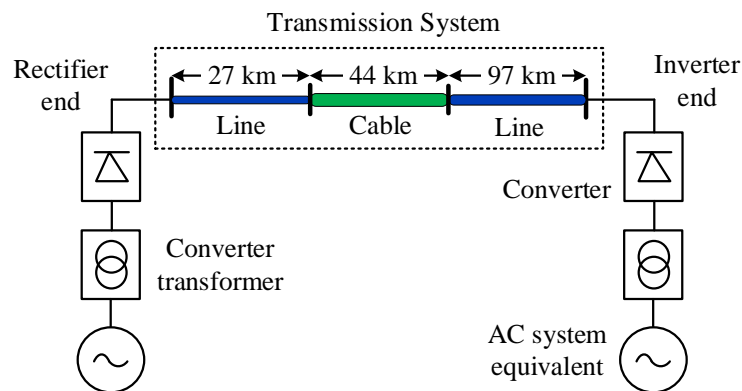
Figure 4.16 HVDC test system used for the case study 4
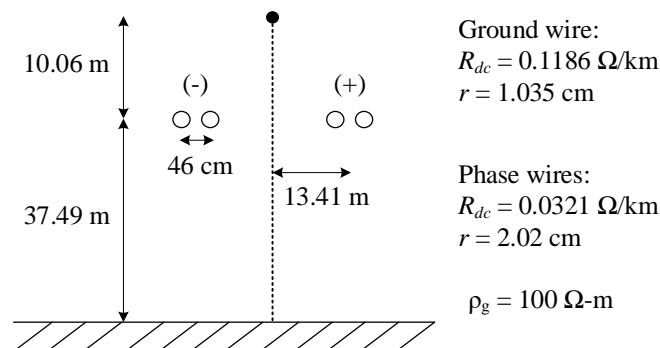
Figure 4.17 Layout of the line segments in Figure 4.16
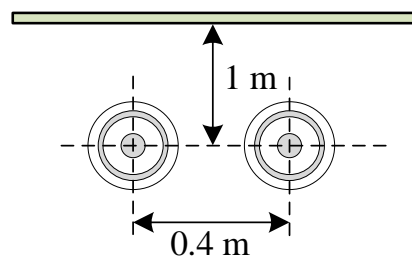
Figure 4.18 Layout of the cable segment in Figure 4.16

Table 4.3 Cable data for the system of Figure 4.18

Inner-Outer Radius of the Core	00.00-33.00 mm
Inner-Outer Radius of the Sheath	66.00-66.44 mm
Outer Insulation Radius	76.00 mm
Resistivity of Sheath	1.72×10^{-8} Ohm-m
Resistivity of Core	1.72×10^{-8} Ohm-m
Core Insulator Relative Permittivity	4.10
Shield Insulator Relative Permittivity	2.30
Insulation Loss Factor	0.001
Earth Resistivity	100 Ohm-m

A unit step voltage is applied to the sending end of the positive conductor (see Figure 4.19) while the receiving end is grounded by a resistance of 1Ω. The negative conductor is left open at both ends. The steady-state magnitudes of V_2 and I_4 in Figure 4.19 provided by the FDM/DC are shown in Table 4.4. These values are compared against the method of [70], and the exact solution. The simulation time-step is 10 µs. The smallest time delay in this system is 89.9 µs, corresponding to the 27-km line segment. According to Table 4.4, the steady-state value is the same regardless of the maximum frequency considered in the fitting of $\mathbf{H}$.
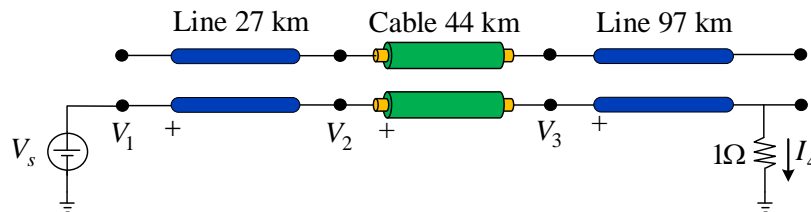
Figure 4.19 Circuit configuration of the case study 4

Table 4.4 Time-domain results (steady-state values)

F_{max}	V_2 (p.u.)			I_4 (p.u.)		
(Hz)	FDM/DC	Ref. [70]	Exact sol.	FDM/DC	Ref. [70]	Exact sol.
10^6	0.8650	0.8647	0.8649	0.3112	0.3112	0.3107
10^5	0.8650	0.8647		0.3112	0.3112	

Table 4.5 lists the steady-state results obtained with the ULM. The fitting is performed using three different minimum frequency values. It can be observed in Table 4.5 that, as the lower limit of the fitting frequency range approaches 0.001 Hz, the steady-state values seem to be closer to the ones obtained with FDM/DC. Figure 4.20 shows the time-domain waveforms for I_4 obtained

by using ULM and FDM/DC. The upper limit of the fitting frequency range for both models is 1 MHz. The ULM approach shows oscillations and its steady state response is not accurate even when the lower limit of the fitting frequency range is set to 0.001 Hz.

Table 4.5 Steady-state magnitude results obtained by ULM

F_{min} (Hz)	F_{max} (Hz)	Steady-State values (p.u.)	
		V_2	I_4
0.100		0.7783	0.2233
0.010	10^6	0.8665	0.3091
0.001		0.8691	0.3242
0.100		0.8761	0.2523
0.010	10^5	0.8659	0.3083
0.001		0.8663	0.3084
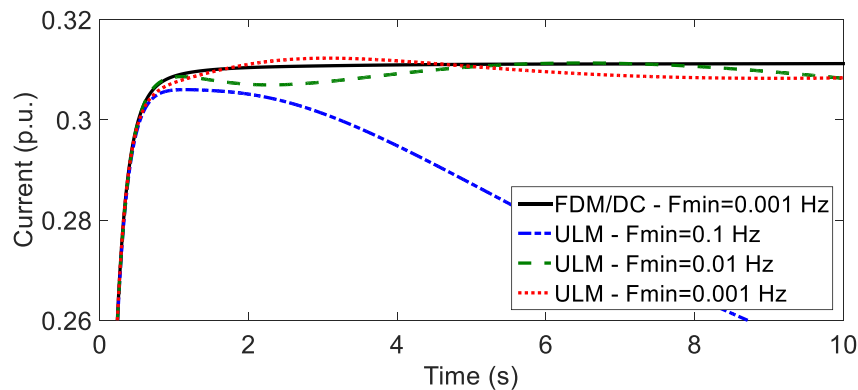
Figure 4.20 Time domain results for I_4 in Figure 4.19 with time-step of 10 µs.

4.2.5 Case study 5: Hybrid AC/DC transmission line

This example is aimed to further demonstrate numerical stability performances of FDM/DC and ULM techniques. Consider the 125-km hybrid AC/DC line configuration depicted in Figure 4.21. The transient scenario consists of applying a unit step voltage behind a resistance of 0.001 Ω to the sending end of conductor C5, while the receiving end is grounded by a resistance of 1 Ω. The rest of the conductors are left open at both ends. In ULM, the fitting range is set from 0.001 to 10^6 Hz.

The energization of the line results in unstable ULM simulation, as seen in Figure 4.22 despite the ULM model is passive. The numerical problems are due to the integration errors related to large residue/pole ratios explained before. If the frequency range is reduced to 0.01 to 10^5 Hz, the

fitting is relaxed, and the model becomes stable in the time domain. However, the steady-state DC solution becomes inaccurate this time (see Figure 4.23). The new partitioning and DC correction method either applied to FDCM or ULM allows achieving numerical stability in the time domain, as shown in Figure 4.22 and Figure 4.23.

The method of [70] is also tested for this case and applied to correct the DC response. Like ULM, it results in unstable simulations in the time domain due to large integration errors.
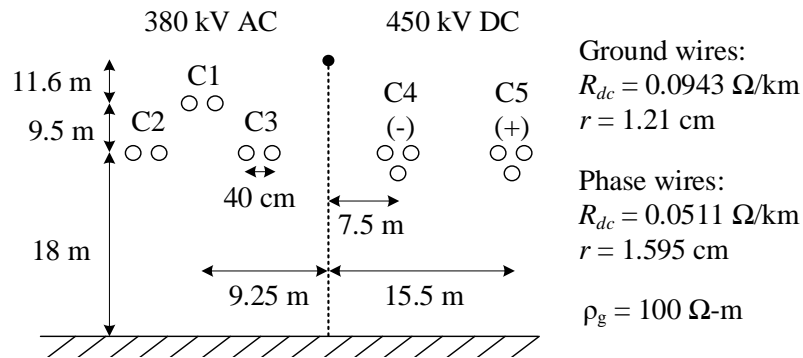
Figure 4.21 Hybrid AC/DC line geometry for the case study 5
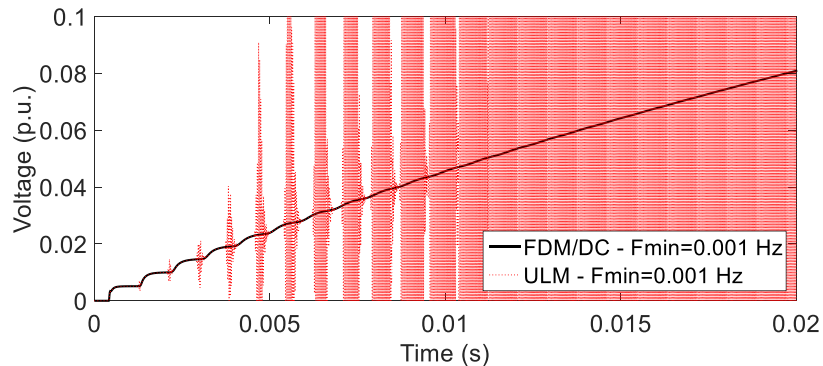
Figure 4.22 Voltage at the receiving end of C5 in Figure 4.21, time-step 10 µs
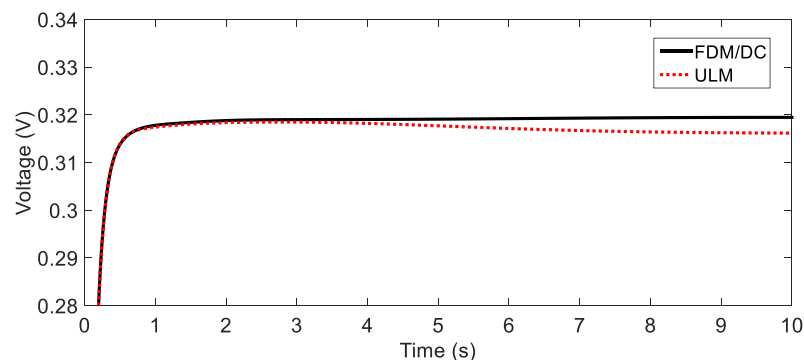
Figure 4.23 Voltage at the receiving end of C5 in Figure 4.21, time-step 10 µs

4.3 Conclusions

This chapter presents the time-domain implementation details of the frequency dependent line model used in this thesis. Then, the performance of the fitting procedures proposed in Chapter 3 is studied through various cases. The impact of improving the fitting of $\mathbf{H}$ in time-domain simulations is analyzed via transient studies.

Numerical results show that, when the proposed fitting approach is combined with a precise integration scheme, it leads to stable and accurate time-domain simulations. This is particularly the case for induced transient voltages. In addition, the proposed approaches complement the prevailing ULM by eliminating spurious oscillations or numerical instabilities due to opposing high residue pole pairs coming from different but close delay groups. Moreover, it is shown that the DC-correction fitting procedure allows improving the accuracy in the computation of DC steady-state waveforms.

CHAPTER 5   ADAPTIVE LINE MODEL

As mentioned in Chapter 1, several line and cable models have been developed during the last decades [5]-[39]. It has been observed that the more sophisticated models suffer from computational performance issues when they are used in long-term steady-state simulations, while the simplified models are not sufficiently accurate to simulate fast-front transients. To address these problems, this chapter proposes a unified model that can adapt itself to both steady- and transient-state studies by relaxing the line equations during the time-domain simulation, while maintaining appropriate accuracy and computational performance.

Simulation of EMT using relaxing models have been proposed through the shift frequency concept [71]-[74]. This chapter proposes to switch between WB and PI models during the simulation. The WB model is used during a transient where precise models are required, whereas the CP model is used during the steady state. Basically, the idea is relaxing the line equations during the steady state to increase the speed of the EMT-type computations. The switching between WB and CP models is performed by modifying the terms of the history current vectors and their corresponding elements in the nodal admittance matrix during the simulation. Although the WB model can also be switched to the PI model, the CP model is preferred since its topology is similar to that of the WB model, providing more flexibility in the numerical implementation. This flexibility becomes very attractive for multi-scale modeling applications [73] and real-time simulations [35]. The proposed model includes an algorithm that enables the automatic setting of the line model along the simulation. In every transition point, the required variables and states are initialized based on phasor analysis. The proposed model is verified via time-domain simulations.

5.1 Adaptive line model

This section presents an adaptive model used to increase the speed of time-domain simulations.

5.1.1 Relaxation scheme

Basically, the idea of the proposed relaxation scheme is switching between WB and CP models during the simulation. The time-domain implementation details of the WB and CP models are explained in Chapter 4 and Appendix A, respectively. The proposed method uses the WB model during a transient where precise models are required, and switches to the CP model when steady-

state is reached, see Figure 5.1. The objective is relaxing the line equations during the steady-state to increase the speed of EMT-type computations. It is mentioned that PI model can also be used during the steady state; however, the CP model is preferred since it provides more topological flexibility. The implementation of the PI model creates physical coupling between both line ends, which is a disadvantage for parallel computing. In the proposed adaptive line model, the history current terms of the CP and the WB models are initialized based on their steady-state phasor solution. In every transition point, the elements of the nodal admittance matrix of the network are modified accordingly.
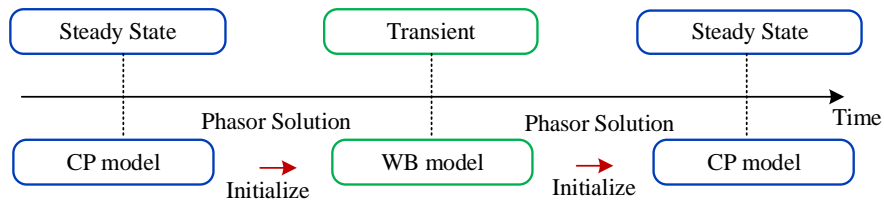
Figure 5.1 Transition steps in the proposed adaptive line model

5.1.2 Switching control algorithm

This section presents a control algorithm that enables the automatic setting of the line model during the simulation, see Figure 5.2. The control algorithm is explained as follows:

1) Simulation starts with the steady-state phasor solution. The first time-domain solution is found at $t = \Delta t$ with history term computed from the steady-state at $t = 0$.

2) If any discontinuity occurs, such as a switching event, simulation continues with the WB model connected in the network; otherwise, simulation continues with the CP model.

3) After finding the transient-state solution with the WB model, simulation continues to the next time step.

4) After each fundamental period, the algorithm tracks natural waveforms to find any steady state condition. If such condition is detected, then the simulation switches to the CP model.

5) After finding the steady-state solution with the CP model, simulation continues to the next time step.

6) Step 2 is repeated. Simulation switches to WB model if any other discontinuity is detected.

7) Simulation ends after the steps 3 and 5 when the simulation time T is met.
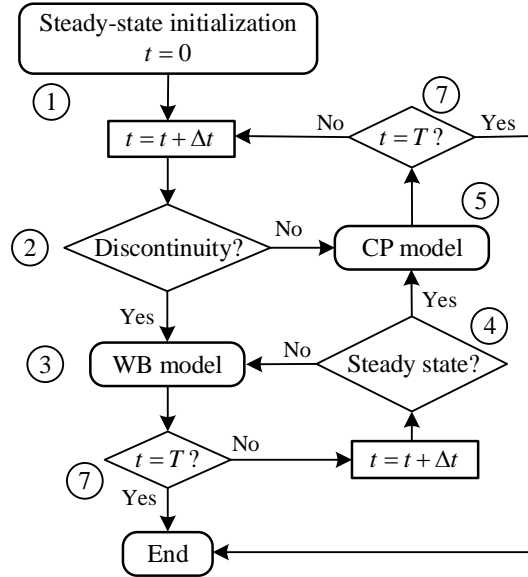
Figure 5.2 Proposed switching control algorithm

5.1.3 Model initialization

For initialization proposes, the network is solved based on phasor analysis. Initialization from steady-state phasor solution allows to start in an almost perfect steady state in the time domain. The first time-domain solution is found at $t = \Delta t$ with history term computed from the steady-state at $t = 0$. At every transition point, the variables of the line equations must be updated.

WB model equations

To initialize the variables and states of the discretized WB model equations, the network is solved in the phasor domain based on the use of the equivalent PI of the line (see Figure 5.3). The nodal solution in the phasor domain is expressed as

$$\begin{bmatrix} \mathbf{Y}_{sh} - \mathbf{Y}_{ser} & \mathbf{Y}_{ser} \\ \mathbf{Y}_{ser} & \mathbf{Y}_{sh} - \mathbf{Y}_{ser} \end{bmatrix} \begin{bmatrix} \mathbf{V}_k \\ \mathbf{V}_m \end{bmatrix} = \begin{bmatrix} \mathbf{I}_k \\ \mathbf{I}_m \end{bmatrix} \tag{5.1}$$
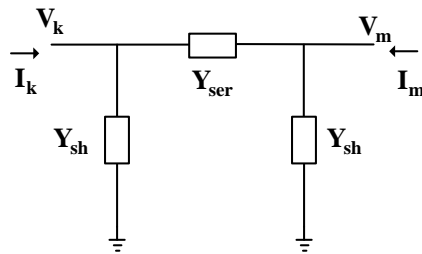
Figure 5.3 Equivalent PI model

Existing formulations for the steady-state initialization of a transmission line consider the exact PI model equations, where the shunt and series admittance matrices are given by:

$$\mathbf{Y_{sh}} = \mathbf{Y_c} \tanh\left(\sqrt{\mathbf{YZ}}l/2\right) \tag{5.2}$$

$$\mathbf{Y_{ser}} = \mathbf{Y_c} \Big/ \sinh\left(\sqrt{\mathbf{YZ}}l\right) \tag{5.3}$$

However, the use of the exact PI is prone to create mismatches between the steady-state values obtained in the phasor solution and the steady-state values calculated with the WB model. This is because the nodal admittance matrix calculated in the exact PI and WB models is not numerically identical. In the proposed formulation, the nodal admittance in (5.1) is calculated using the fitted propagation function $\mathbf{H}$ and characteristic admittance $\mathbf{Y_c}$. Then, (5.2) and (5.3) are found with

$$\mathbf{Y_{sh}} = \left(\mathbf{U} - \mathbf{H}^2\right)^{-1}\left(\mathbf{U} - \mathbf{H}^2\right)\mathbf{Y_c} - 2\left(\mathbf{U} - \mathbf{H}^2\right)^{-1}\mathbf{HY_c} \tag{5.4}$$

$$\mathbf{Y_{ser}} = 2\left(\mathbf{U} - \mathbf{H}^2\right)^{-1}\mathbf{HY_c} \tag{5.5}$$

where $\mathbf{U}$ is an identity matrix. Next, considering (4.27), the states of the discretized propagation function convolution at $t = 0$ are computed as

$$\mathbf{x_{k}}_{i,j}(0) = \frac{\mathbf{I_{mr}}}{2} \frac{e^{-j\omega\cdot\Delta t\cdot(n_i+1-\varepsilon_i)}\mu_{i,j}'' + e^{-j\omega\cdot\Delta t\cdot n_i}\lambda_{i,j}''}{1 - e^{-j\omega\cdot\Delta t\cdot(1-\varepsilon_i)}\alpha_{i,j}''} + \frac{\mathbf{I_{mr}^*}}{2} \frac{e^{j\omega\cdot\Delta t\cdot(n_i+1-\varepsilon_i)}\mu_{i,j}'' + e^{j\omega\cdot\Delta t\cdot n_i}\lambda_{i,j}''}{1 - e^{j\omega\cdot\Delta t\cdot(1-\varepsilon_i)}\alpha_{i,j}''} \tag{5.6}$$

where ω is the network frequency.

In a similar manner, the states of discretized convolution of characteristic admittance are initialized as follows

$$\mathbf{x_{Yc}}_{k,i}(0) = \frac{\mathbf{V_k}}{2} \frac{1}{1 - e^{-j\omega\cdot\Delta t}\alpha_i} + \frac{\mathbf{V_k^*}}{2} \frac{1}{1 - e^{j\omega\cdot\Delta t}\alpha_i} \tag{5.7}$$

Finally, the history current terms are found as

$$\mathbf{I_{hist_k}} = -\mathrm{Re}\left\{\mathbf{I_k} - \mathbf{G_{Y_c}}\mathbf{V_k}\right\} \tag{5.8}$$

$$\mathbf{I_{hist_m}} = -\mathrm{Re}\left\{\mathbf{I_m} - \mathbf{G_{Y_c}}\mathbf{V_m}\right\} \tag{5.9}$$

The traveling wave buffers are initialized by applying phase shift to the history current phasors. The phase shift is function of the number of time steps from the initial steady state.

CP model equations

For the CP model initialization of the subsequent time-domain solution, the two lossless sections of Figure A.1 are replaced by a lossless approximation of the model of Figure 5.3. Each lossless section is considered with a halved equal propagation time. The resulting series and shunt admittance matrices are used to calculate the phasor solution for each mode in the CP model. The terminal current phasors are given by:

$$\mathbf{I_k'} = \mathbf{Y_{sh}'} \mathbf{V_k'} + \mathbf{Y_{ser}'} \left(\mathbf{V_k'} - \mathbf{V_m'} \right) \tag{5.10}$$

$$\mathbf{I_m'} = \mathbf{Y_{sh}'} \mathbf{V_m'} + \mathbf{Y_{ser}'} \left(\mathbf{V_m'} - \mathbf{V_k'} \right) \tag{5.11}$$

and the history current terms are found as

$$\mathbf{I_{hist_k}'} = -\mathrm{Re}\left\{ \mathbf{I_k'} - \mathbf{G'}\mathbf{V_k'} \right\} \tag{5.12}$$

$$\mathbf{I_{hist_m}'} = -\mathrm{Re}\left\{ \mathbf{I_m'} - \mathbf{G'}\mathbf{V_m'} \right\} \tag{5.13}$$

The traveling wave history buffers are initialized by applying phase shift to the history current phasors. The buffer length depends on the propagation delay and the integration time-step. The propagation delay for each mode must be greater or equal to the integration time-step.

5.1.4 Tracking the steady state

To find the switching time t_{sw} when the steady state is reached during the simulation, the natural waveform of the voltage at the receiving end of the line is monitored. The proposed idea is explained as follows (see Figure 5.4). Starting at the beginning of a transient, a buffer of voltage samples of the length of the fundamental period T_n is created. Then, the fast Fourier transform (FFT) [80] is applied on the waveform of the voltage stored in the buffer. The resulting frequency spectrum F_s is analysed. The steady state is reached when the only frequency component found in F_s correspond to the fundamental frequency. It is noted that the buffer is updated throughout the simulation, maintaining the same length.
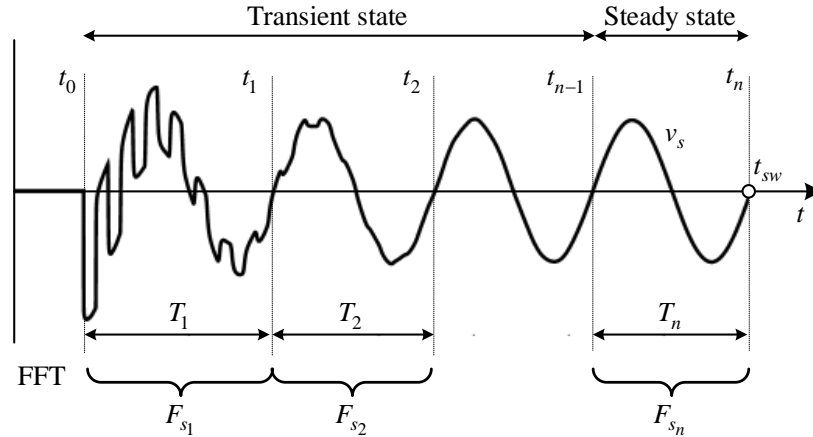
Figure 5.4 Tracking the steady state waveform

5.1.5 Phasor solution at the switching time

At each switching time t_{sw}, the variables and states corresponding to the subsequent model (WB or CP) must be initialized for the following time-domain solution. To initialize the subsequent model at t_{sw}, the steady-state phasor of the voltages at both line ends are required.

At the beginning of the simulation, the steady-state solution (nodal voltages) is calculated by solving the network using phasors. However, the steady state values obtained during the time-domain simulation may be different than the values obtained from the initial phasor solution. In this thesis, the steady-state phasors are obtained as follows.

Consider the instantaneous voltage values from the steady-state period T_n previous to t_{sw}, see Figure 5.5. The natural waveform depicted in Figure 5.5 is expressed as

$$v_s\left(t_{sw}-\Delta t\right)=V\cos\left(\omega_0\left(t_{sw}-\Delta t\right)+\theta\right) \tag{5.14}$$

$$v_s\left(t_{sw}\right)=V\cos\left(\omega_0 t_{sw}+\theta\right) \tag{5.15}$$
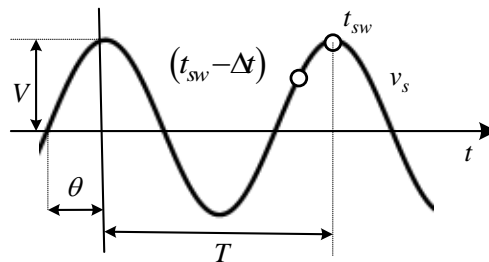
Figure 5.5 Finding the steady state phasor solution

Solving (5.14) and (5.15) gives the values for the magnitude V and phase θ of the corresponding phasor. Once the phasor voltages at both line ends are found, the variables of the next model are initialized according to Section 5.1.3.

5.2 Numerical results

The numerical example presented in this section considers the three-phase transmission line system of Figure 2.5. For a time-domain analysis, the line is modeled with the WB model and the proposed adaptive line model, which is named in this thesis as WB-CP. The implementation of both models and the entire network is performed in the Matlab platform.

5.2.1 Example 1: Single transition point

The voltage of phase A at the receiving end is shown in Figure 5.6 for a simulation time T of 0.16 s, when the three phases are simultaneously closed at $t_c = 0.0083$ s. In the WB-CP model (dashed line), simulation starts with the WB model being connected to the circuit; after 0.1 seconds, the simulation switches the line model to the CP model. This solution is compared with the solution obtained from the WB model only (solid line). It can be observed that the solution obtained by the WB-CP model agrees with the solution obtained with the WB model.
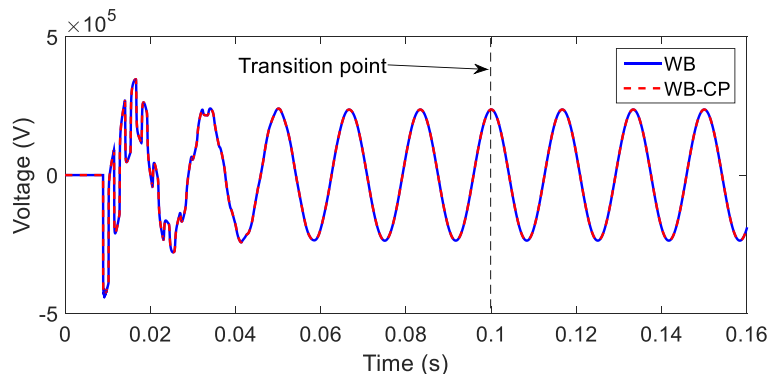
Figure 5.6 Voltage of phase A at the receiving end. Simulation time of 0.16 s

The CPU times of the simulation corresponding to the WB and WB-CP are 9.6 and 6.3 s, respectively. That is, the simulation obtained using the WB-CP model is 34.4 % faster than the simulation obtained by the WB. It should be noticed that the gain is only obtained during the last 3.5 cycles. If the WB-CP model is used for longer simulations, the CPU-time gain is increased. For instance, Figure 5.7 shows the simulation results for a long-term steady state simulation,

which may be followed by a fault. The CPU-time gain time is 68.8 %. Table 5.1 lists the CPU times for both simulations.
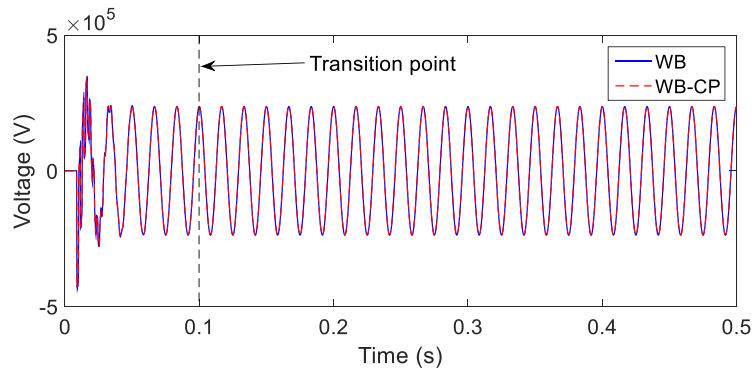
Figure 5.7 Voltage of phase A at the receiving end. Simulation time of 0.5 s

Table 5.1 Comparison of CPU times

Model	CPU time (s)	
	$T = 0.16$	$T = 0.5$
WB	9.6	28.5
WB-CP	6.3	8.9
Gain	34.4 %	68.8 %

5.2.2 Example 2: Three transition points

To observe the performance of the proposed WB-CP model in the transition from CP to WB, an additional switching event is applied in the simulation of Section 5.2.1. This new simulation includes grounding the phase B at the receiving end of the line from 0.16 s to 0.17 s. During this time, phases A and C remain open. The voltage of the three phases at the receiving end is presented in Figure 5.8. It is observed that the overvoltage on phase B after clearing the fault is influenced by the interphase coupling of the other phases, see Figure 5.9.
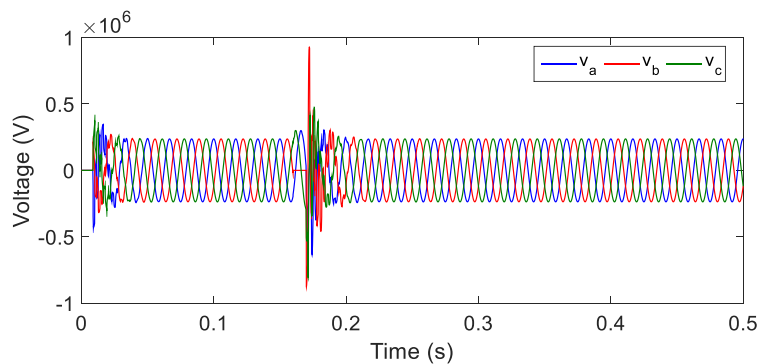
Figure 5.8 Voltage of the three phases at the receiving end obtained with WB-CP model
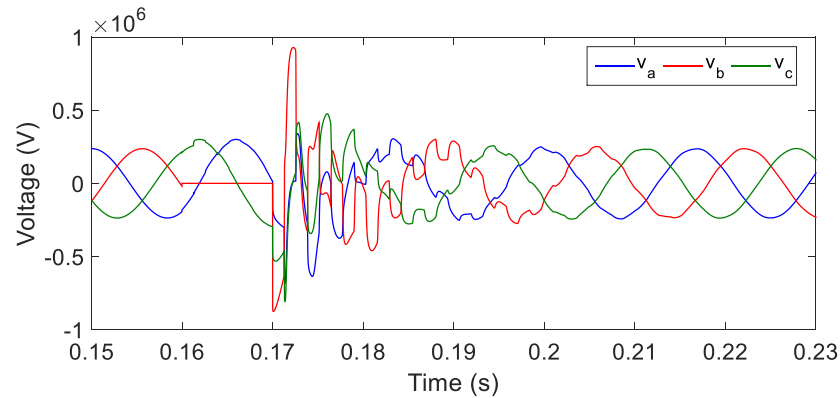
Figure 5.9 Voltage of the three phases at the receiving end obtained with WB-CP model, transient state

Figure 5.10 compares the solution of phase B with the solution obtained with the WB only. It is noticed that three transition points occur in the WB-CP model (dashed red lines). First, simulation starts with the WB model being connected to the circuit; after 0.1 seconds, the simulation reaches the steady-state condition and switches the line model to the CP model. Next, when the fault on phase B appears, i.e. at 0.16 s, simulation switches to WB. Finally, once the steady-state is again reached at 0.25 s, simulation switches back to CP. It can be observed from Figure 5.10 that the solution obtained by the WB-CP model agrees with the solution obtained with the WB. The CPU-time gain obtained with the WB-CP compared to that of the WB model is of 47.4 %.

It is noted that the CPU-time gain of the WB-CP in this example is obtained by simulating a simple network. The computational gain obtained with the proposed WB-CP may become more significant in multi-scale modeling applications.
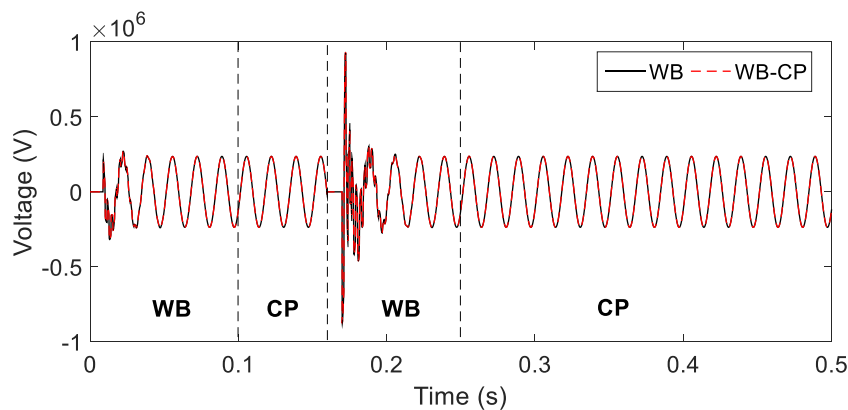
Figure 5.10 Voltage of phase B at the receiving end. Comparison between WB-CP and WB

5.3 Analysis of other switching schemes

This section discusses two alternative switching schemes for the proposed adaptive model. Switching from WB model to PI model is labeled as WB-PI model. Switching from WB model to a reduced-order WB model is labeled as WB-RWB model.

5.3.1 Switching from WB to PI model: WB-PI model

As an alternative switching scheme to the proposed adaptive model, the WB model is switched to the PI model during the steady state to accelerate the time domain simulation. The PI model is accurate, and its implementation is simple; however, there is no a substantial increase in the computational gain compared to that obtained with the WB-CP model, as will be demonstrated in the example of Section 5.3.3. Moreover, it should be remarked that the implementation of the PI model creates physical coupling between both line ends, which is a disadvantage for parallel computing.

5.3.2 Switching from WB to reduced WB: WB-RWB model

This section analyzes the use of a reduced-order WB model in the proposed adaptive model. In this approach, both $\mathbf{H}$ and $\mathbf{Y_c}$ are fitted in a low frequency range. Since the fitting is performed in a reduced frequency band, the required number of poles is relatively small. The reduced fitted model is then used during the steady state to increase the speed of simulation. The drawback of this approach is the fact that the line functions cannot be properly fitted for a reduced frequency band. Figure 5.11 presents the entry $(1,1)$ of $\mathbf{H}$ fitted from 0.001 Hz to 100 Hz. It is observed that $\mathbf{H}$ cannot be accurately fitted regardless of the number of poles. This problem can be addressed by increasing the fitting frequency range. For instance, Figure 5.12 presents the fitting results when the fitting range is increased to 100 kHz. It is observed that the fitting precision is significantly improved.

To evaluate the performance of the reduced-order WB (RWB) model in time-domain simulations, the system of Figure 2.5b is tested. Figure 5.13 shows the steady-state waveform of the phase A. The RWB model is fitted from 0.001 Hz to 100 kHz using 4 and 8 poles. It is observed that the steady state waveform is simulated with acceptable accuracy.
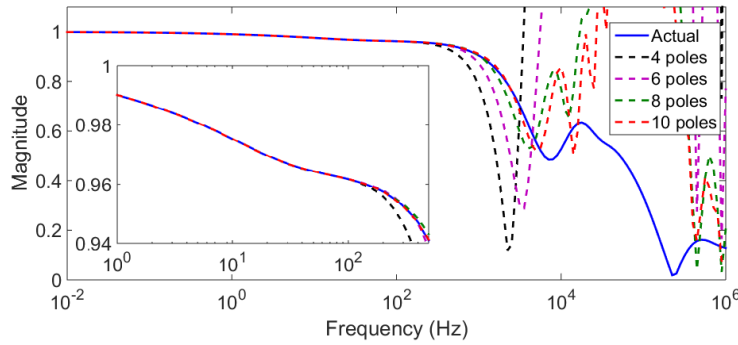
Figure 5.11 Element $\mathbf{H}(1,1)$ of the line of Figure 5.7 fitted from 0.01 Hz to 100 Hz
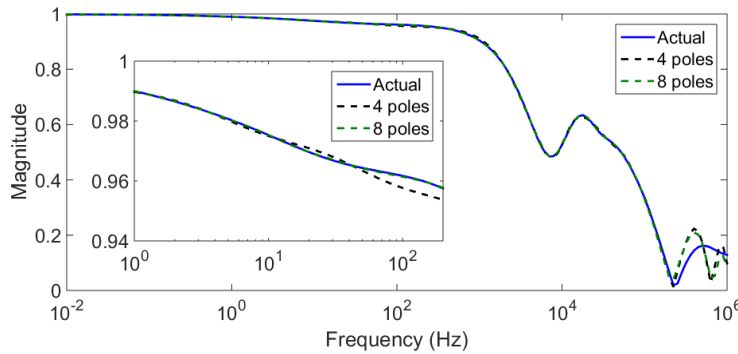
Figure 5.12 Element $\mathbf{H}(1,1)$ of the line of Figure 5.7 fitted from 0.01 Hz to 100 kHz
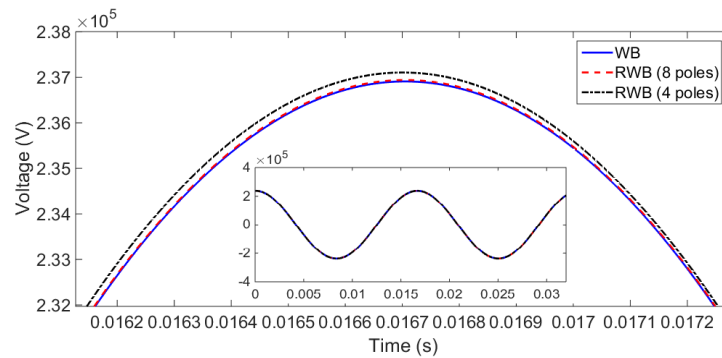
Figure 5.13 Steady-state simulation of phase A, $\mathbf{H}$ fitted from 0.01 Hz to 100 kHz

As another alternative, the order of the fitted functions can be reduced via the frequency-domain balance realization (FDBR) method [81]. This technique permits to reduce a state-space model, fitted from a wideband of frequency, to a specific frequency range. The downside of this approach is that is not always possible to greatly reduce order of approximation. Moreover, is not always possible to obtain stable poles. Figure 5.14 presents the entry $(1,1)$ of $\mathbf{H}$ fitted from 0.001 Hz to 100 Hz. It is observed that $\mathbf{H}$ cannot be accurately fitted regardless of the number of poles. It is mentioned that, some of the fitted functions of Figure 5.14 contain unstable poles.
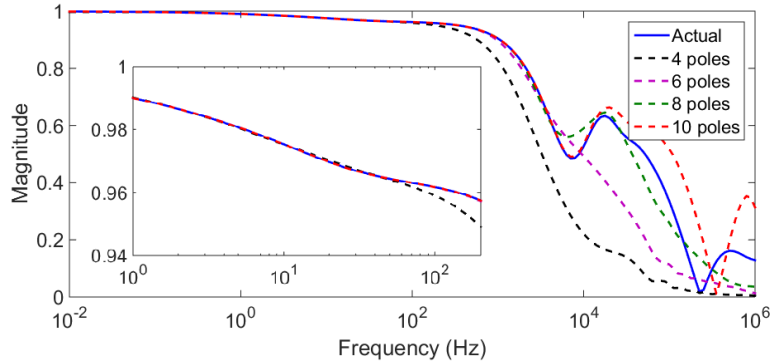
Figure 5.14 Element $\mathbf{H}(1,1)$ of the line of Figure 5.7 fitted with the FDBR technique

5.3.3 Numerical example

To evaluate the accuracy and computational performance of the WB-PI and WB-RWB models, the simulation of Figure 5.7 is repeated. The simulation results are compared with the ones obtained with the WB and the WB-CP models. Simulation results are presented in Figure 5.15. The CPU times are listed in Table 5.2. In the WB model, $\mathbf{H}$ and $\mathbf{Y_c}$ are fitted, from 0.01 Hz to 1 MHz, with 12 and 8 poles, respectively. In the RWB model, $\mathbf{H}$ and $\mathbf{Y_c}$ are fitted, from 0.01 Hz to 100 kHz, with 8 and 4 poles, respectively. It is observed from Figure 5.15 that the solution obtained by all models is in agreement. According to Table 5.2, the WB-RWB model does not significantly reduce the CPU time compared to the WB-CP model. On the other hand, there is not significant difference in the gain obtained with the WB-CP and WB-PI models. However, it is remarked that the WB-PI model creates physical coupling between the line ends.
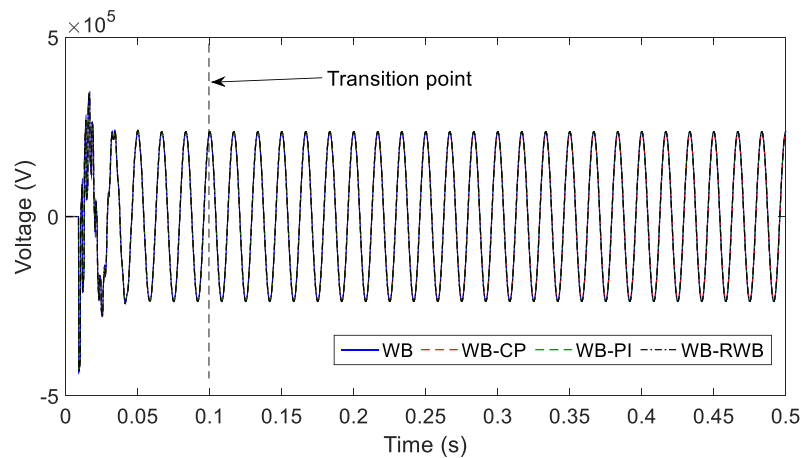
Figure 5.15 Voltage of phase A at the receiving end. Comparison between different models

Table 5.2 Comparison of CPU times for the simulation of Figure 5.15

Model	CPU time (s)	Gain
WB	28.5	-
WB-CP	8.9	68.8 %
WB-PI	8.1	71.58 %
WB-RWB	22.8	19.30 %

5.4 Conclusions

This chapter presents an adaptive transmission line model based on switching between WB and CP models. The WB model is used during a transient where precise models are required whereas the CP model is used in steady-state. The proposed idea is to relax the line equations during the steady state to increase the speed of the EMT-type computations. The switching between the two models is performed by modifying the terms of the history current vectors and their corresponding elements in the nodal admittance matrix during the simulation.

The proposed model includes an algorithm that enables the automatic setting of the line model during the simulation. At every transition point, the required variables and states are initialized based on phasor analysis. Numerical results show that the solution obtained with the adaptive approach (WB-CP model) matches that obtained from the WB only. The WB-CP model provides faster simulation than the WB model. Alternative switching schemes have not shown significant improvements in terms of computational performance compared to the proposed WB-CP model.

The proposed adaptive model has been tested in a simple network. However, the flexibility provided by the proposed WB-CP allows to cover diverse transients with only one set of models, which is very attractive for multi-scale modeling applications and real-time simulations.

CHAPTER 6   SIMULATION OF SWITCHING OVERVOLTAGES AND VALIDATION WITH FIELD TEST

On transmission lines where switching surges are not mitigated with closing resistors and/or surge arresters, high-speed reclosing on a line with trapped charge will produce high overvoltages. The research work presented in this chapter aims to identify the required simulation practices in reproducing field measured overvoltages in EMT simulations. Variations in line modeling and electrical parameters have been tested in an unsuccessful attempt to reproduce the field data. It is demonstrated that even though the pattern of the transient voltage waveforms can be reproduced very well using frequency-dependent line models, the magnitude of the maximum overvoltage is significantly overestimated unless the effect of corona is included. Two types of corona models are tested, and both demonstrate that corona is the primary factor that allows the simulations to correctly reproduce high peak overvoltage measurements.

6.1 Background

Switching of transmission lines results in electromagnetic transients that propagate along the lines as discussed in many references, including [82]-[84]. The switching overvoltages are more significant during high-speed reclosing due to the trapped charge on the line [85]. Switching overvoltages tend to be well controlled at the extra high voltage level with closing resistors and/or arresters, but below that level they have not historically been controlled. Although arresters are common today, older lines used rod gaps installed at the ends of the line to protect the substation equipment by flashing over during lightning overvoltages. However, below extra high voltage switching overvoltages may also be sufficiently high to flash over the rod gaps during high-speed line reclosing. Such an event occurred on the Bonneville Power Administration (BPA) Big Eddy-Chemawa 230 kV line and prompted an investigation and switching surge field test as describe in [64], [86].

The 1995 field test performed by BPA was intended to verify the modeling techniques in EMT-type programs and determine the highest overvoltages at the receiving end of a 230-kV line during high-speed reclosing with a trapped charge [64]. The resulting measurements included data taken at 1 MHz for 50 high-speed reclosing tests with a maximum measured overvoltage of 3.3 pu. Reference [86] provides a description of the BPA field test, including the purpose,

procedures and measurements along with a summary of the main results. The recorded field measurements provide a unique opportunity for the experimental validation of line models [3], [12], [27] at high overvoltage levels in EMT-type programs. Rather than validate the EMT studies, the field measurements showed that for the highest switching surge voltage levels, the EMT studies are not accurate and overestimate the overvoltages by about 1 pu, or 30%. The importance of this becomes clear when it is recalled that the highest 2% of overvoltage results of switching surge studies are normally used for line design and reliability purposes, while the maximum overvoltages are often used for safety-related purposes such as minimum approach distances.

The objectives of the research work presented in this chapter are to validate line models using the field test, to understand the major factors in the reproduction of field measurements using simulations and to investigate the sensitivity of simulations to various modeling and electrical parameters. For validation purposes, the waveforms recorded during the "Three-phase line switching test series" reported in [64] are used since they approximate high-speed reclosing and produced the highest switching-surge overvoltages. In principle, once a line model is validated, it is possible to proceed with statistical simulation phase to identify the worst-case overvoltage, which is of utmost importance for transmission line and substation related issues such as the evaluation of minimum approach distance and clearance practices [64].

According to the results presented in this chapter, refinements in ground resistivity, skin effect, phase-to-ground conductance and detailed source modeling are not sufficient to match maximum transient overvoltages. The peak of the transient voltage is significantly overestimated unless the effect of corona is included. On the other hand, the pattern of the transient overvoltage waveforms is matched when frequency dependent line models are employed, and multiple prestrike events are sequentially produced in the simulation environment.

The representation of corona involves a distributed nonlinear hysteresis behavior, and it is complex to combine it with the line model equations in EMT studies [57], [58], [87], [88]. Most of the methods proposed in the literature rely on subdividing the line into linear subsections and represent corona with non-linear shunt branches at each junction [14]. In this work, the Suliciu Model [63] and the corona model presented in [61] are used. Both models require subdividing the line into linear sections.

6.2 Big Eddy-Chemawa test system

The Big Eddy-Chemawa line is a 230-kV line of 116 miles long. It originates at the Big Eddy Substation near The Dalles, Oregon, and terminates at the Chemawa Substation near Salem, Oregon. Figure 6.1 shows the one-line diagram of the Big Eddy-Chemawa 230-kV line and the detailed test system. The results of the BPA field investigation are reported in [7]. The BPA report includes overvoltage and field data recorded during the switching surge field test on the Big Eddy-Chemawa line. The switching surge field tests consist of single-phase and three-phase line switching with and without trapped charge. The three-phase test is selected in this paper since it produced the highest overvoltages [64].
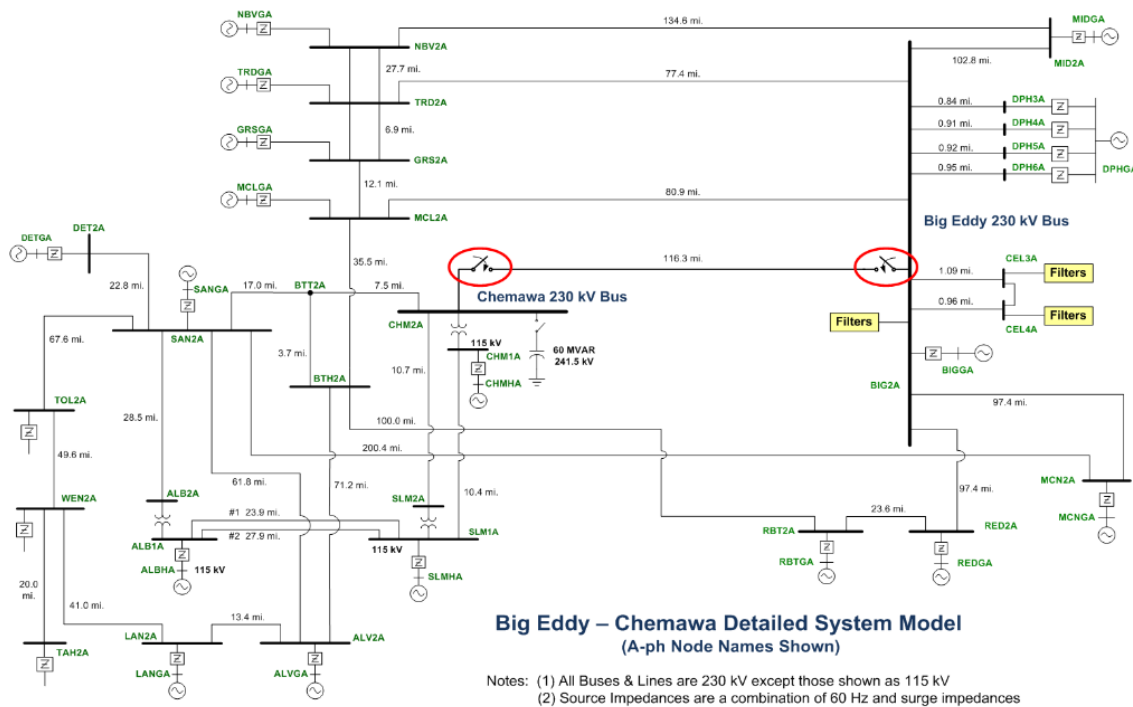
Figure 6.1 Big Eddy-Chemawa 230-kV detailed system model [64]

6.2.1 Three-phase line switching test

The purpose of the three-phase test is the collection of measurements for the verification of EMT models and statistical data on overvoltages that could be expected during high-speed reclosing [64]. The highest switching surge overvoltage occurs when reclosing a line with trapped charge. In tests reported in [64], switch opening is controlled and synchronized to generate the same polarity and magnitude of trapped charge on each phase for each of the reclosing tests. The

breaker closing times were varied uniformly over a complete 60 Hz cycle by increments of 18 electrical degrees (1/20 cycle). Closing from Big Eddy provided line switching measurements with a strong source, while closing from Chemawa provided measurements with a relatively weak source. The results shown in this chapter includes the switching transient analysis for the cases 5-02, 5-03, 5-05 (switching from Big Eddy side), and 5-53 (switching from Chemawa side) of [64] since they present the highest overvoltage levels. The overvoltages measured at each end of the line during these cases are listed in Table 6.1, whereas the trapped charge values are presented in Table 6.2. The steady-state peak line-to-ground bus voltage prior to switching is 197.6 kV at Big Eddy and 187.4 kV at Chemawa.

Table 6.1 Three-phase line switching, peak voltages (kV)

Case	Big Eddy end line voltage			Chemawa end line voltage		
	A-Ph	B-Ph	C-Ph	A-Ph	B-Ph	C-Ph
5-02	442.3	-284.1	-493.8	505.6	445.9	-643.2
5-03	452.1	409.9	-570.6	566.6	561.6	-638.9
5-05	459.7	-284.0	-541.9	536.9	529.2	-622.8
5-53	-587.0	-569.8	497.4	-394.4	332.5	288.9

Table 6.2 Trapped charge voltages (kV)

Case	Relative closing angle (degrees)	A-Ph	B-Ph	C-Ph
5-02	0	-235.4	-176.4	179.6
5-03	18	-230.9	-175.2	179.8
5-05	54	-234.3	-177.4	181.9
5-53	18	221.2	185.1	-184.14

6.2.2 Field test data

The critical line voltage measurements were made with laboratory-quality RCR dividers to ensure accurate measurements from DC to 1 MHz as described [86].

6.3 Test system modeling in EMTP

To reproduce the field measurements using simulations, the test system is modeled with varying level of details. Line parameters, conductor data and other relevant system details are given in [86] and [89]. A description of the various modeling approaches and details follows.

6.3.1 Big Eddy-Chemawa line model

As shown in the right-of-way drawing of Figure 6.2, there are two additional 230-kV lines parallel to the Big Eddy-Chemawa line for part of its length, along with a 525-kV line.
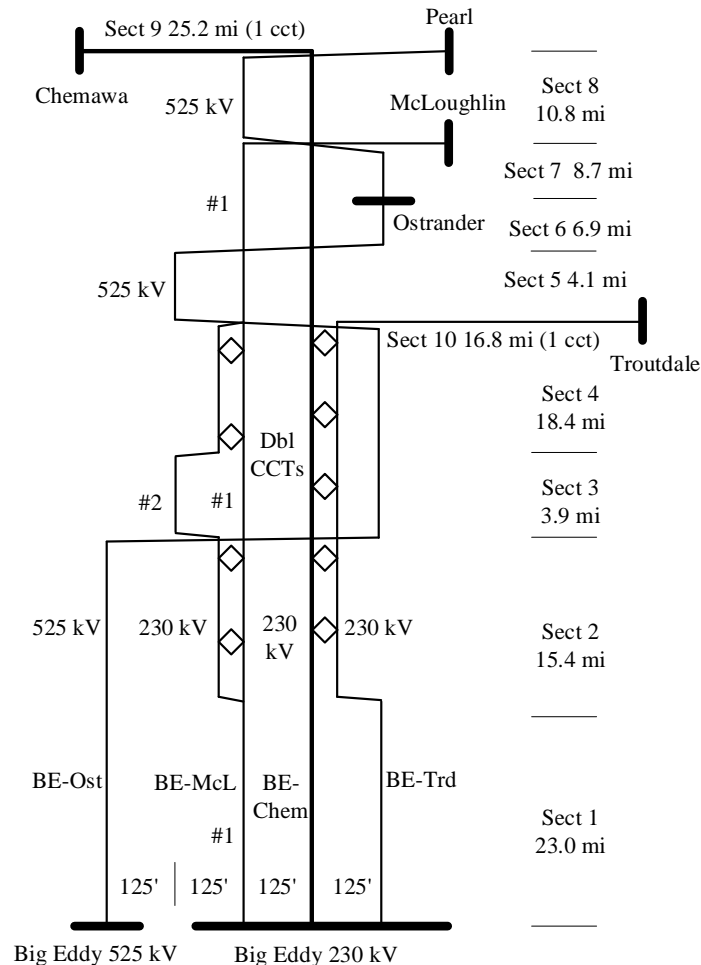
Figure 6.2 One-line diagram of Big Eddy-Chemawa and parallel lines, [89]

In this work, the Big Eddy-Chemawa line is modeled together with the three parallel lines due to their impact on transients as will be shown in Section 6.5.1. The configuration of this line system, consisting of 10 sections with different geometry, is illustrated in Figure 6.2. All the sections are modeled using either the wideband (WB) model which is the implementation of the Universal Line Model in EMTP [27], the frequency-dependent (FD) line model [12], and the constant parameters (CP) model [3]. The line parameters including conductor data and line geometries at different sections are available in [89]. The CP model parameters are evaluated at 1 and 10 kHz.

6.3.2 Trapped charge model

To account for the trapped charge on the line, a three-phase dc voltage source is connected to the line with magnitudes as given in Table 6.2. The source is disconnected at the instant when the switching transients are triggered.

6.3.3 Filter and capacitor bank models

Filters and capacitor banks seen in Figure 6.1 are modeled with equivalent circuits. The equivalent models connected at the Chemawa and Big Eddy buses are shown in Figure 6.3 with the numerical parameters of the components [89].
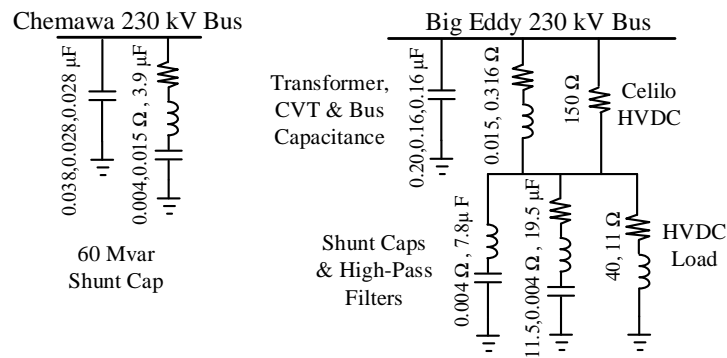
Figure 6.3 Equivalent model for filters and capacitor banks

6.3.4 Simplified and detailed source models

The surrounding system connected to the Big Eddy-Chemawa line and its parallel lines, is either represented by using simplified equivalent source models as shown in Figure 6.4 or the detailed source model, i.e. with surrounding system, as given in Figure 6.1. The source and surge impedance data are listed in Table 6.3 for the simplified source models (subscript 1 and 0 stand for positive and zero sequence, respectively). Table 6.4 shows the bus voltage levels used in the simulations. The angles are initialized through steady state solution.
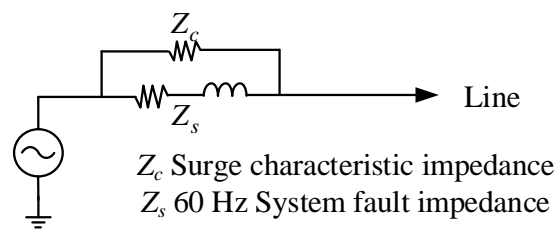
Figure 6.4 Simplified source model

Table 6.3 Source impedance data for buses along Big Eddy-Chemawa line

Bus	Z_s (Ω)				Z_c (Ω)	
	R_1	X_1	R_0	X_0	Z_{c_1}	Z_{c_0}
Big Eddy 230	0.12	3.1	0.06	2.0	42	81
Chemawa	1.60	12.6	1.30	16.0	190	365
McLoughlin	0.28	4.8	0.24	4.1	63	122
Troutdale	0.36	5.0	0.31	4.8	76	146
Big Eddy 525	0.70	14.0	0.60	12.0	56	130
Ostrander	1.80	21.0	2.20	25.0	93	217
Pearl	1.30	20.0	2.10	24.0	140	325

Table 6.4 Source voltage data for buses along Big Eddy-Chemawa line

Bus	Nominal voltage (kV)	Approximated bus Voltage (kV)	Voltage angle phase A (deg)
Big Eddy 230	230	240	0
Chemawa	230	237	0
McLoughlin	230	238	-11
Troutdale	230	238	-11.7
Big Eddy 525	525	542	0
Ostrander	525	539	-4.5
Pearl	525	539	-10

6.3.5 Prestrike modeling

There are multiple prestrikes during the closing events, as described in [64], and they are different for each phase. The switching times are very important for producing the exact waveform of transients [85]. The multiple prestrikes are modeled by a set of switches, which is connected at the sending end of the line. The switch closing times are determined from the voltage and current measurements. The opening time is the first instant when the current crosses zero during the transients. Forcing the interruption at an instant determined from the measurements alone generates current chopping phenomenon that mismatches the pattern of field measurements in simulations. The sequence of switching times is given in Table 6.5.

As an alternative to the modeling of prestrikes, a tabulated source using the measurements at the switching end is also tested. In this case the source is an ideal source that forces the measurements at the sending end of the line. This approach is supposed to account for the impact of prestrikes intrinsically.

Table 6.5 Sequence of switching times

Phase	Condition	Time (ms)			
		Case 5-02	Case 5-03	Case 5-05	Case 5-53
A	Closes	0.000	0.000	0.000	0.000
	Opens	1.262	0.856	1.264	1.270
	Closes	2.180	2.260	1.832	2.170
	Opens	-	-	3.081	4.990
	Closes	-	-	3.575	5.380
B	Closes	5.087	4.060	3.776	3.730
	Opens	-	4.936	-	-
	Closes	-	6.100	-	-
C	Closes	3.130	1.800	1.894	0.890
	Opens	4.370	2.596	3.159	3.560
	Closes	4.780	3.510	4.140	4.660
	Opens	7.020	7.616	-	-
	Closes	7.380	8.510	-	-

6.4 Preliminary switching transient studies

This section is the initial study step on the field test results of Case 5-03. The system of parallel lines in Figure 6.2 is built by considering the modeling approaches described in Section 6.3. Two cases are studied for the energization of the Big Eddy-Chemawa line system:

1) Tabulated source model using measurements

2) Simplified source using switches for prestrikes

To simplify the comparisons between waveforms, only one phase with substantial overvoltages will be shown.

6.4.1 Simulation results using a tabulated source model

In this case, the Big Eddy-Chemawa line model is energized at the Big Eddy end by a tabulated source. The voltage of phase A at the Chemawa end is shown in Figure 6.5. The different line models, including FD, WB, and CP are compared with the field data. Note the -231 kV initial trapped charge in the measurements and on the line models. Figure 6.5 shows that the WB and FD models yield similar results. However, they don't follow the pattern of the field data, there are unexpected spikes, and there is a mismatch of 0.23 pu in peak values compared to the measured value of 3.02 pu. Moreover, the damping in simulations seems to be slower than the one in

measurements, which may be due to the lack of surge impedance in the tabulated source. On the other hand, Figure 6.5 shows that the waveform associated with the CP model is not as accurate as the ones obtained with the FD or WB model. The performance of the CP model depends on the frequency at which the parameters are evaluated. In the cases of Figure 6.5 and Figure 6.6, 1 kHz provides better results than 10 kHz.

It is mentioned that adjustments in ground resistivity and phase to ground conductances did not improve the results significantly (not shown).
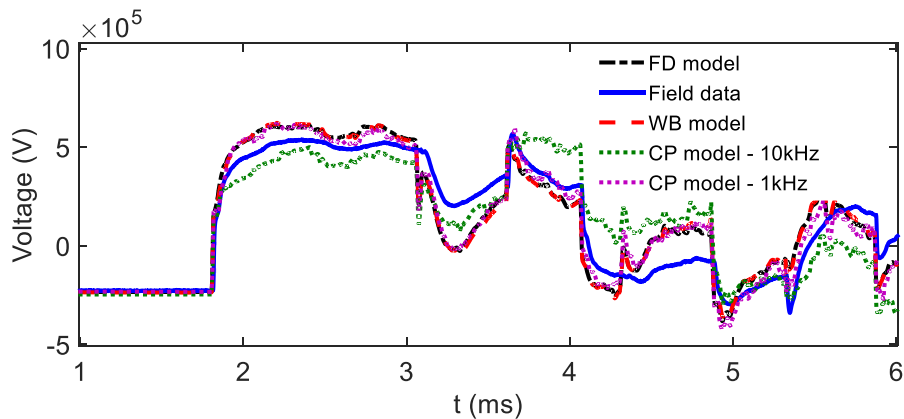
Figure 6.5 Voltage of phase A at Chemawa end, tabulated source model

6.4.2 Simplified source model with prestrike

In this test, the Big Eddy-Chemawa line is energized from the Big Eddy bus using a simplified source with prestrikes created with a set of switches as described in Section 6.3.5. The voltage of phase A at the Chemawa end for the simplified source model is shown in Figure 6.6. It can be observed in Fig. 6 that the WB and FD models produce simulation results that are very close to each other. However, although the voltage waveforms follow the pattern of the field measurements better compared to the previous test case, the peak voltages are overestimated by about 1.62 pu. On the other hand, as in the previous test case, the CP model does not follow the waveform pattern. It is noted that the frequency dependence of line parameters is important in this study.

Similar results are obtained with different ground resistivity and different phase to ground conductance values (not shown).
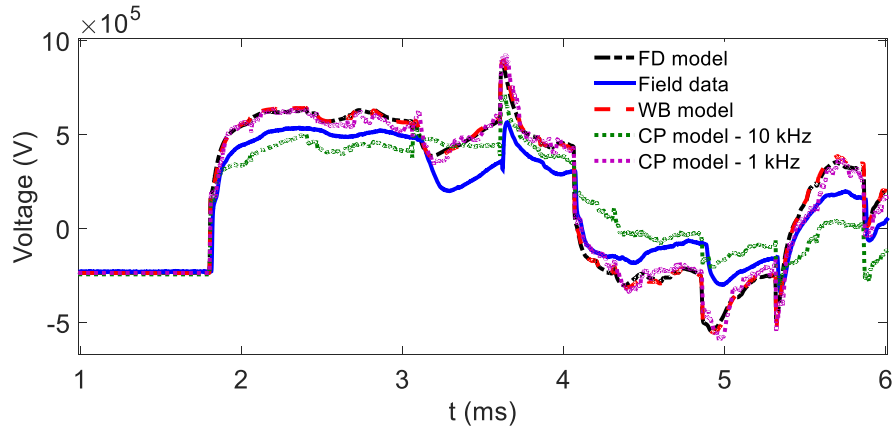
Figure 6.6 Voltage of phase A at Chemawa end, simplified source model

6.4.3 Comparison of tabulated and simplified source models

Modeling the Big Eddy-Chemawa line system by using the FD model only, a comparison between the results of tabulated and simplified source model is presented in Figure 6.7. The simplified source model produces waveforms that follow the field data better but overestimates the peak more than the tabulated source model does.

An analysis on the line parameters is presented next.

Figure 6.7 Voltage of phase A at the Chemawa end, comparison between tabulated and simplified source model with the FD model.

6.5 Analysis of line parameters

The simplified source model, and the FD model are used to produce the simulation results of this section.
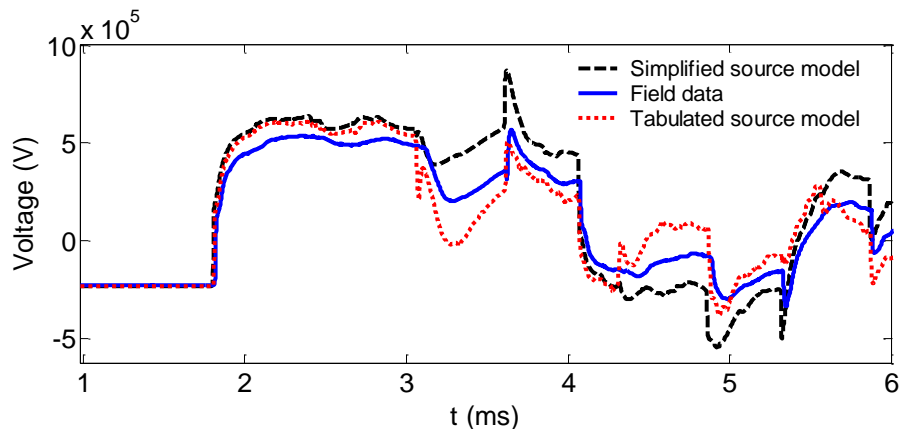
6.5.1 Effect of the parallel lines

The impact of parallel lines can be seen in Figure 6.8 where simulation results are provided for the voltage of phase A at the Chemawa end for Case 5-03 with and without parallel lines. Removing the parallel lines reduces the simulated peak overvoltage from 4.63 pu to 3.65 pu. The results are non-intuitive, where the parallel line modeling further increases the overvoltages. The impact is mainly due to the closely-coupled 230 kV line. The impact of parallel lines on switching transients is discussed in many references including [90].
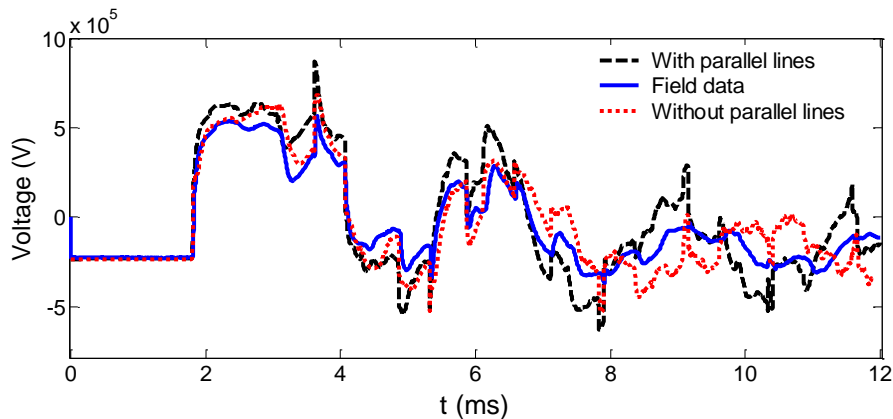
Figure 6.8 Voltage of phase A at Chemawa end, effect of the parallel lines

6.5.2 Refinements in ground resistivity, phase-to-ground conductance and skin effect correction

The BPA expert on transmission line ground resistivity estimated that the values would fall between 50 and 200 Ω-m, where the higher values might occur in mountainous regions [89]. Rather than using the default 100 Ω-m for the entire Big Eddy-Chemawa line, the following values are proposed [89]: i) 100 Ω-m for the first 23 miles (section 1), ii) 200 Ω-m for the next 38 miles (sections 2 to 4), and iii) 50 Ω-m for the remaining 55 miles (sections 5 to 9).

Considering possible additional losses in the line system, the assumed phase-to-ground conductance of 2×10^{-10} S per unit length, is modified to 1×10^{-8} S. Additionally, a correction on skin effect is considered by including the thickness-of-aluminum/outside diameter-of-conductor data [89]. The simulation results are shown in Figure 6.9. The peak overvoltage reduces from 4.63 pu to 4.53 pu with the additional considerations in the computation of line parameters, and it is not possible to match field measurements through these refinements.
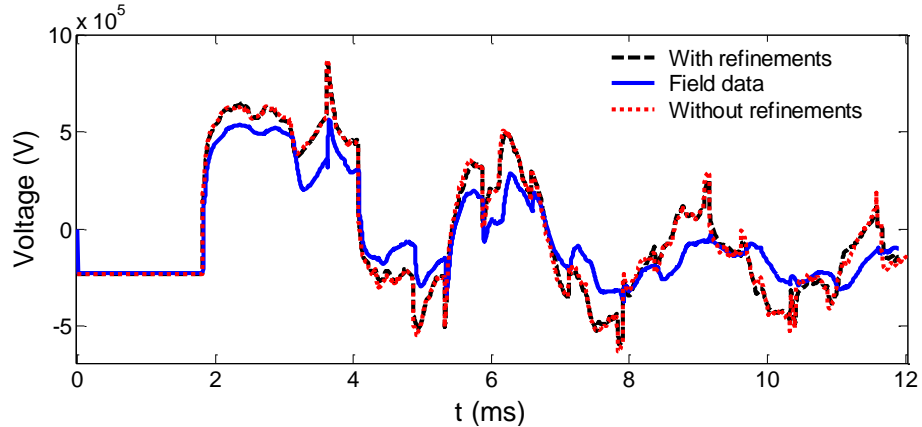
Figure 6.9 Voltage of phase A at the Chemawa end, effect of model refinements

6.5.3 Detailed source model

To obtain more precise results in the simulations, instead of the simplified source models described in Section 6.3.4, a detailed model is used to perform the switching transient analysis of Case 5-03. The detailed system model includes all the surrounding elements in Figure 6.1 with detailed parameters taken from [89].

The Big Eddy-Chemawa and the parallel lines are modeled as shown in Figure 6.2, using the FD model for all the 10 sections. The trapped charge and the prestrike conditions are the same as described in Section 6.3.2, and, 6.3.5, respectively. The simulated voltage of phase A at the Chemawa end is shown in Figure 6.10. It is noticed that there is not a significant difference between the simulation results obtained with detailed and simplified source models.
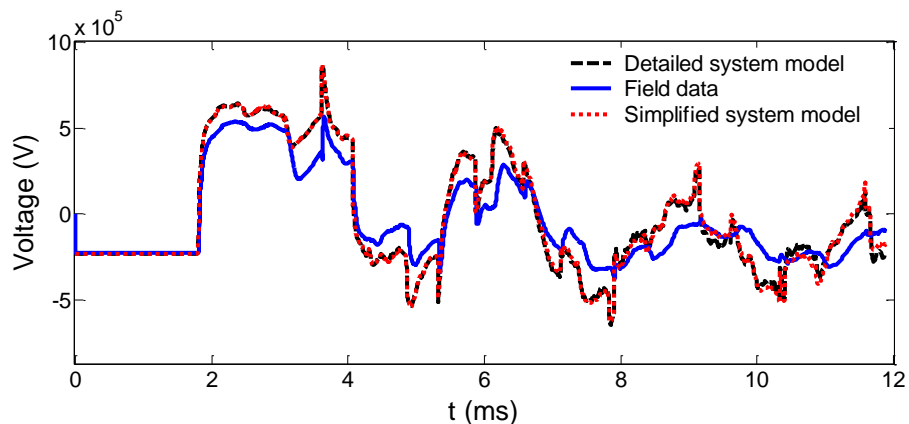
Figure 6.10 Voltage of phase A at the Chemawa end considering a detailed source model

6.5.4 Discussion on line parameters

Several different approaches have been considered to reproduce the field data for Case 5-03. Simulation results show that various improvements such as refinements in ground resistivity and phase-to-ground conductance, correction on skin effect and the use of detailed source model have little impact on the transient voltage waveform. This implies that a phenomenon is present on the line that acts to reduce the switching surge magnitudes that hasn't yet been included. Thus, the effect of corona is considered next.

6.6 Inclusion of the corona effect in the line model

Although considering the frequency dependence of line parameters without considering corona helped improve the simulation waveforms, it still overestimates the transients [57], [58], [87], [88]. Corona has a strong effect on wave propagation [58], [14].

In this paper, the Suliciu nonlinear corona model [63] and a linear model [61] are considered. The Suliciu model requires, in principle, the charge-voltage (Q-V) curve of the targeted transmission line, either obtained theoretically or by measurements. In addition, a specific EMT implementation is required for the solution of nonlinear equations and integration to the main solver of the EMT-type program [57].

The linear model is a piece-wise linear model of a nonlinear one and can be easily realized on any EMT-type simulation platform using basic components, i.e., resistors, capacitors and diodes. But the model produces spike-like voltages at the breaking points of the linear curves, like those of an arrester and a nonlinear inductor, as is well-known. The model components can be numerically evaluated by the user once the corona parameters specific to the targeted line are specified (corona onset voltage and corona loss constants) [61].

6.6.1 Suliciu corona model

For the inclusion of corona, the Big Eddy-Chemawa line, including the parallel lines, is divided into subsections of 0.6 miles long (approximately 1 km). The FD model is used for modeling each subsection. The Suliciu corona branch model [63] available in EMTP examples [57], is connected at each section as shown in Fig. 11. The corona branch model equations are described

in [63] and [57], and they are summarized in Appendix A to define the corona parameters. The numerical values of the parameters used in this paper are also given in the Appendix A.

For the analysis of Case 5-03, the Big Eddy-Chemawa line is energized by: a) the tabulated source model as input source, and b) the simplified source model considering the prestrike conditions. Figure 6.12 presents the voltage of phase A at the Chemawa end considering approaches a), and b). It can be observed in Figure 6.12 that the simulation results are clearly better with the inclusion of corona. With the modeling approach a), a "chopping" condition is observed. The simplified source with prestrike modeling provides accurate results with a mismatch less than 0.01 pu in peak overvoltage (Figure 6.12).
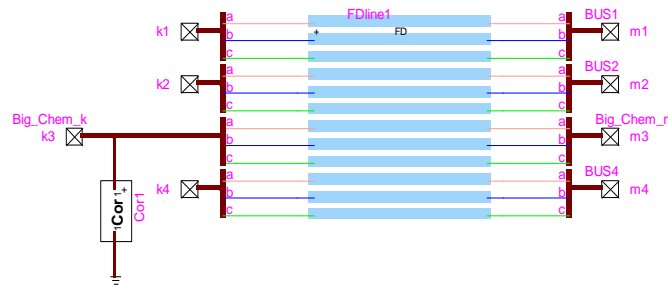
Figure 6.11 Suliciu corona model (shunt branch) with FD model for each section
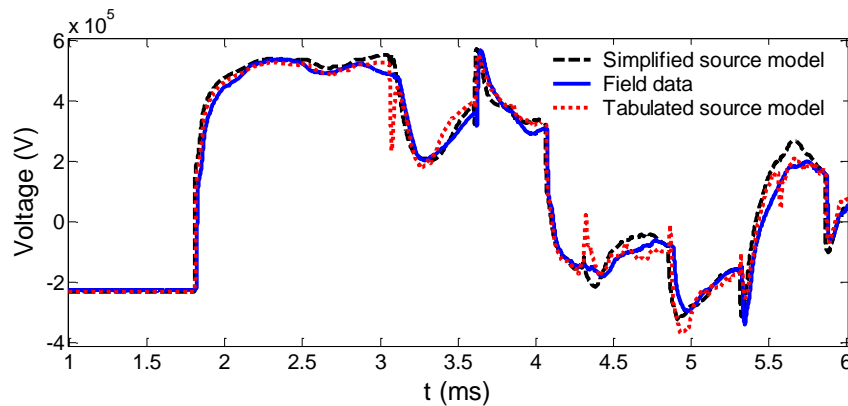
Figure 6.12 Voltage of phase A at the Chemawa end with the Suliciu corona model

6.6.2 Linear corona model

The corona model described in [61] is also considered in this work. This model consists of a piecewise linear approximation. According to [61], three straight lines are sufficient to approximate the nonlinear characteristic of a nonlinear corona model. Thus, the model used in this paper includes three linear RC parallel branches as detailed in the Appendix A.2. The

constants of the linear corona model used in this paper are defined in the Appendix A.2 together with the basic equations used to obtain them.

Considering that the Big Eddy-Chemawa line is energized by the simplified source model, the voltage of phase A at the Chemawa bus is shown in Figure 6.13. The lines are divided into 0.6 miles long sections in both models to model the corona effect. It can be observed in Figure 6.13 that there is no significant difference between the two corona models. But as the simulation time gets longer, the linear corona model presents spikes as seen in Figure 6.14. Moreover, it requires careful tuning of the model parameters (corona onset voltages and loss constants) to match the pattern and peak. However, the Suliciu model is less sensitive to its parameters and it was even possible to obtain close results by using the example parameters for the 230-kV line in EMTP corona example.

Figure 6.13 Voltage of phase A at Chemawa end. Comparison of Sulicio and linear corona model

Figure 6.14 Voltage of phase A at the Chemawa end. Comparison of the Suliciu and Linear Corona models. 12ms (high resolution field data).

6.6.3 Longer simulation time

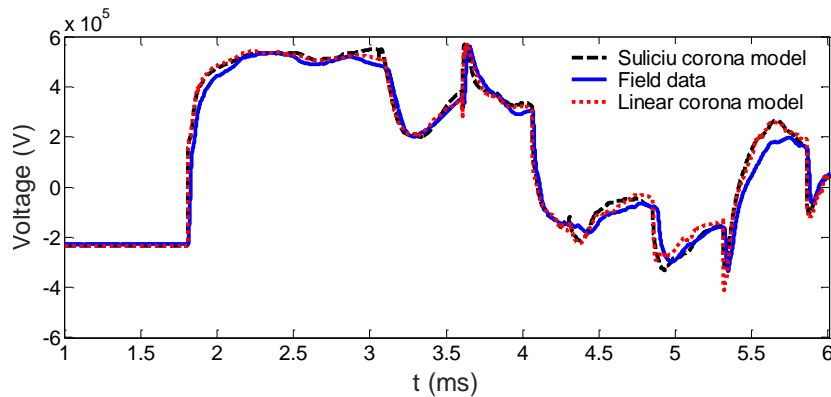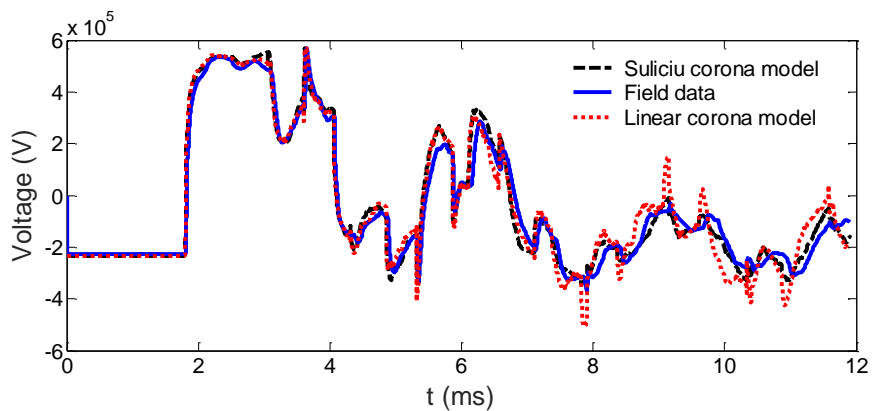Considering the simplified source model and the Suliciu corona model only, longer simulations were performed and compared with the field data. A 100 ms simulation is presented in Figure 6.15 to show the steady-state solution after the switching transients have damped out. Figure 6.15 shows that the simulation results match the field data with the inclusion of corona in the model and that the Suliciu corona model provides a stable steady-state result. The field data is available up to 66ms only.
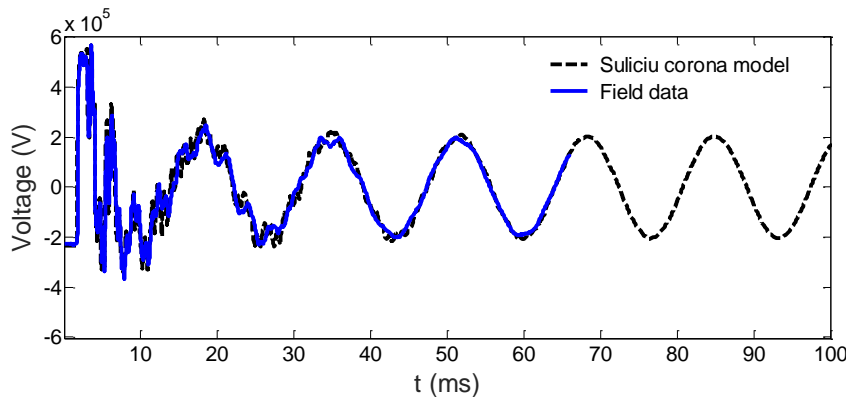
Figure 6.15 Voltage of phase A at the Chemawa end including the Suliciu corona model for a 100-ms simulation time

6.7 Switching transient studies: other cases

This section studies three additional cases, i.e., Case 5-02, Case 5-05, and Case 5-53. The relative energization angle, and the trapped charge values for these cases are already listed in Table 6.2.

For the switching transient analysis of Case 5-02, Case 5-05, and Case 5-53, the test system of Figure 6.1 is modeled as described in Section 6.3. The corona effect is included by dividing the Big Eddy-Chemawa line into sections of 0.6 mi, considering only the Suliciu model. The Big Eddy-Chemawa line is energized by a simplified source model including the multiple prestrike conditions. For Case 5-02 and Case 5-05, the Big Eddy-Chemawa line is energized from the Big Eddy end (strong source), while for Case 5-53, it is energized from the Chemawa end (weak source). The switching times for all cases are shown in Table 6.5. Figure 6.16, Figure 6.17, and Figure 6.18 present simulation results for the cases 5-02, 5-05, and 5-53, respectively. In Figure 6.16, the peak overvoltages are 2.69, 2.78 and 3.11 pu for measured, simulated with corona and

without corona waveforms, respectively. With the same order, the overvoltages in Figure 6.17 are 2.86, 2.97 and 3.41 pu while in Figure 6.18 they are 2.65, 2.65 and 3.45 pu. It is observed that the match between simulation results and field measurements greatly improves with the inclusion of corona. In Figure 6.18 the phase presenting the highest overvoltage, i.e. phase C, is shown.

Figure 6.16 Voltage of phase A at the Chemawa end. Case 5-02
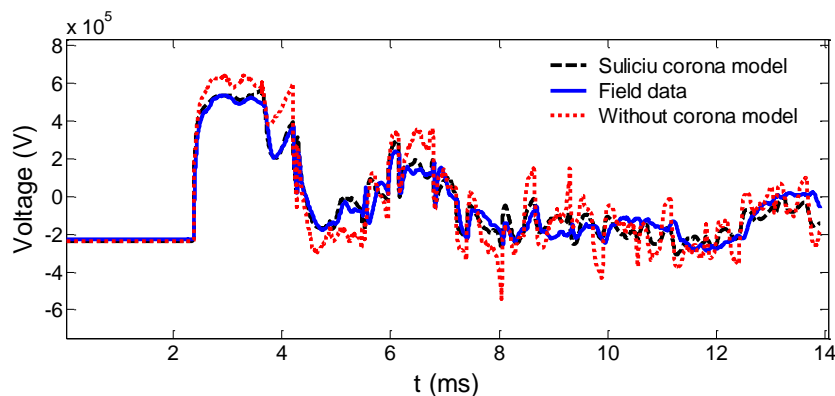
Figure 6.17 Voltage of phase A at the Chemawa end. Case 5-05
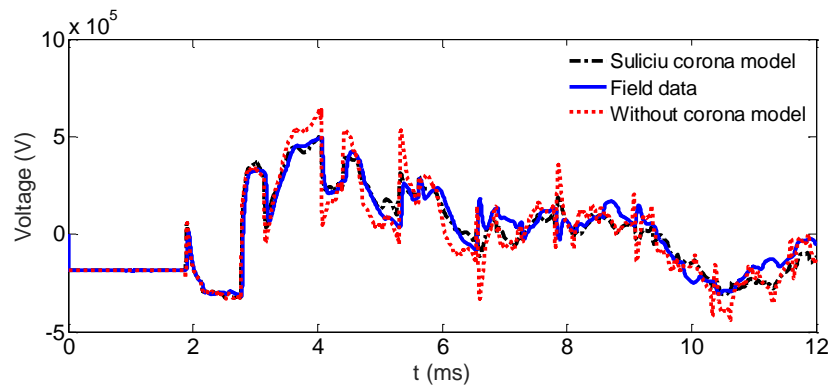
Figure 6.18 Voltage of phase C at the Big Eddy end, Case 5-53

To get simple results for comparison with transient models, an additional single-phase case is also studied, i.e., Case 1-04. The test is 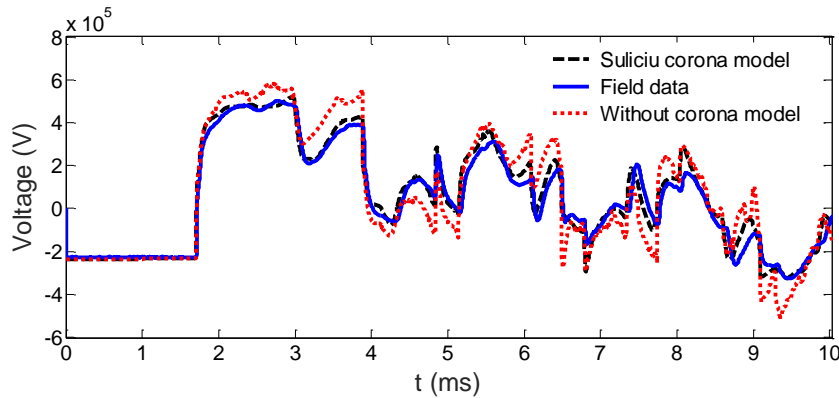performed on phase B. Trapped charge values for this test are: A-ph = -30.90 kV, B-ph = -171.9 kV and C-ph = -23.23 kV. For the switching transient analysis of Case 1-04, the test system of Figure 6.1 is modeled as described in Section 6.3. The Big Eddy-Chemawa line is energized by a simplified source model. The closing time is 18.86 ms. Figure 6.19 present simulation results for Case 1-04. In Figure 6.19, the peak overvoltages are 2.66, 2.65 and 2.97 pu for measured, simulated with corona, and without corona waveforms, respectively. Similar than other cases, it is observed that the match between simulation results and field measurements greatly improves with the inclusion of corona.
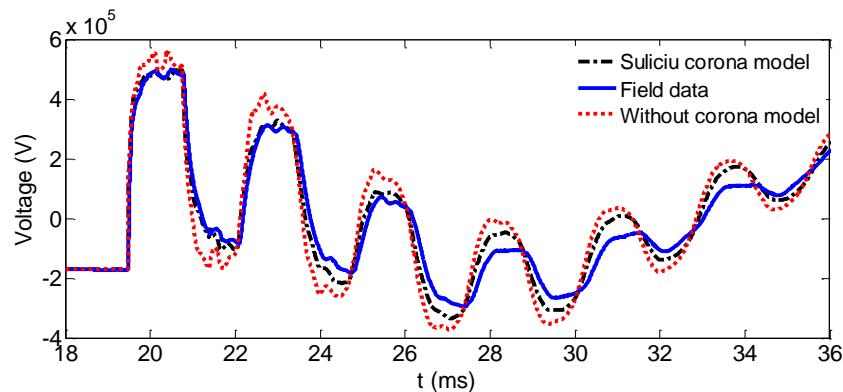
Figure 6.19 Voltage of phase B at the Chemawa end, Case 1-04

6.8 Conclusions

For transmission lines without switching surge mitigation, high-speed reclosing results in significant switching overvoltages due to trapped charge on the line. With frequency-dependent line models and standard simulation techniques, the shapes of measured waveforms are reproduced well, but the peak overvoltages are considerably overestimated compared to actual field measurements. Variations in the numerous typical modeling parameters have shown to not solve the problem of higher simulated voltages. However, modeling corona on the switched line has proven to be the key for simulations to match the measurements. Corona, frequency dependence of line parameters and prestrike have been shown to be the most important factors in matching simulations to the field measured transients, both in terms of waveform pattern and magnitude, as presented here for a 230-kV line.

This work provides the utility industry with a needed breakthrough in simulation techniques for performing switching surge studies and obtaining realistic results.

It is remarked that this work is not targeted toward the situations where switching surges are controlled to lower levels using surge arresters, closing resistors or where trapped charge is removed prior to closing. For those situations, the overvoltages are lower and EMT programs, using standard modeling techniques, are considerably more accurate. For the unique case of shunt-compensated lines, the high overvoltages can still occur where the reactor and accompanying surge arrester are on the same end of the line as the first breaker to reclose.

CHAPTER 7   STATISTICAL SIMULATIONS OF SWITCHING OVERVOLTAGES

As seen in Chapter 6, switching overvoltages along transmission lines are higher during high-speed reclosing due to trapped charge on the line. Chapter 6 is focused on highest measured overvoltages and what can be done to close the gap between measurements and simulations. It is demonstrated that even though the pattern of the transient voltage waveforms can be reproduced very well using frequency-dependent line models, the magnitude of the maximum overvoltage is significantly overestimated unless corona effect is included. In principle, once a line model is validated, it is possible to proceed with statistical simulation phase to identify the worst-case overvoltage, which is of utmost importance for transmission line and substation related issues such as the evaluation of minimum approach distance and clearance practices [89], [64].

The objective of the research work presented in this chapter is to perform statistical simulations to determine the worst-overvoltage scenario at the receiving end of a line with a trapped charge during high-speed reclosing. There are multiple prestrikes during the tests reported in [64], and they are different for each phase. In Chapter 6, the prestrike times are determined from the voltage and current measurements and modeled by a set of ideal switches. Nevertheless, for statistical studies, the switching times must be calculated in a such way that the prestrike conditions are automatically reproduced in the simulation model. The recorded waveforms of voltages and currents in [64] provide a significant amount of prestrike data, which allows to determine the voltage versus time characteristic (dielectric slope) for the breaker. The breaker model used in this chapter includes the dielectric slope characteristic given in [64] to enable the breaker conduction when its voltage withstand is reached. When the breaker is closing, if the voltage at the terminal of the breaker reaches the envelope of the voltage withstand, the gap is closed and opened again when the current crosses zero.

The simulation strategy used in this chapter is explained as follows. First, the breaker closing times of the three phases are systematically varied over a complete 60 Hz cycle to obtain a uniform distribution of overvoltage. The dielectric slope characteristic is used to represent the typical prestrike conditions at each simulation. Once the mean time with the highest overvoltage is found, i.e., the switching time that produces the highest overvoltage, a statistical study is followed. In the subsequent set of simulations, the switching (closing) times for the three phases

are calculated by a Gaussian law, using the previously found mean time value as reference. It is noted that, although the dielectric slope characteristic of the breaker contacts can be used to represent the prestrike conditions, the actual prestrike events may occur very randomly. To represent the highly statistical nature of this phenomenon, an additional set of simulations is performed where the prestrikes times are also estimated by the Gaussian law.

The modeling guidelines presented in Chapter 6 are used in this chapter; however, for running the statistical simulations, the corona model is not included to save CPU time. The simulation with the highest overvoltage is compared afterwards with the one obtained by including corona.

7.1 Simulation model

7.1.1 Big Eddy-Chemawa system model

For the statistical studies performed in this chapter, the test system of Figure 6.1 is modeled considering the following conditions (see modeling guidelines outlined in Chapter 6):

 ➢ The Big Eddy-Chemawa line is modeled together with the three parallel lines (see Figure 6.2) using the FD line model.

 ➢ The surrounding system connected to the Big Eddy-Chemawa line and its parallel lines is represented by simplified equivalent source models (see Figure 6.4).

 ➢ Filters and capacitor banks are modeled with equivalent circuits (see Figure 6.3).

 ➢ A DC voltage source is connected to the line to account for the trapped charge. The source is disconnected at the instant when the switching transients are triggered.

7.1.2 Prestrike model

A significant amount of prestrike data has been obtained from the recorded waveforms of voltages and currents in [64]. The prestrike voltage versus relative prestrike time for each phase of the Big Eddy breaker is shown in Figure 7.1. Linear regression is used to determine the voltage versus time characteristic. It is observed in Figure 7.1 the decreasing dielectric strength of the breaker contacts, as they are closing.

It is reported in [64] that the Big Eddy breaker is constructed with each phase in its own tank, and the maximum closing time difference between the phases (or "pole span") is approximately 3.7

ms. This pole span is determined by taking the difference in time in which the prestrike characteristic of each phase crosses zero voltage [64]. The zero-voltage point is where the breaker contacts are connected metal-to-metal [64].

To represent the dielectric strength of the breaker contacts of Figure 7.1, the model of Figure 7.2 is used. This model enables the breaker conduction when its voltage withstand is reached. When the breaker is closing, if the voltage at the terminal of the breaker reaches the envelope of the voltage withstand (see closing part in Figure 7.2), the gap is closed and opened again when the current goes below zero. In Figure 7.2, u_c represents the maximum value of the withstand voltage of the circuit breaker reached at t_3.
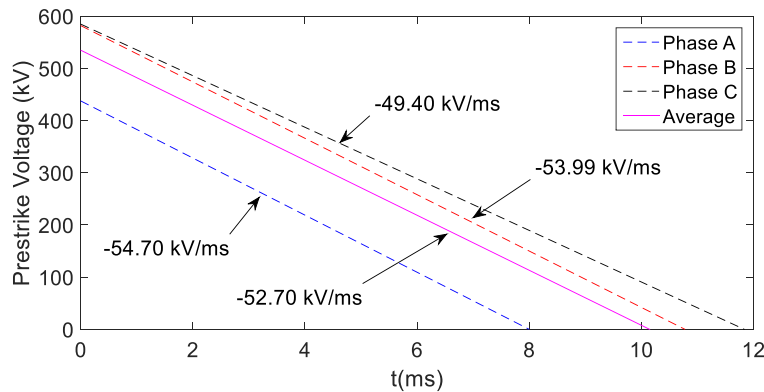

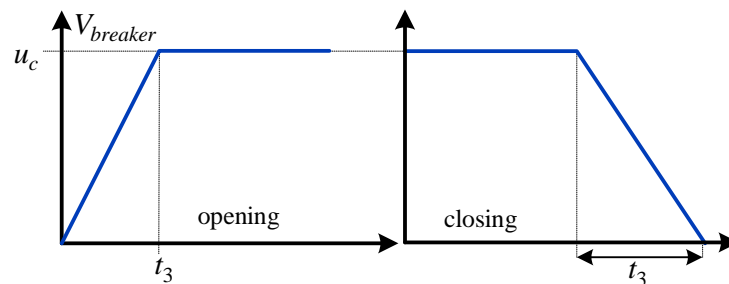Figure 7.1 Big Eddy breaker dielectric slopes based on prestrike data during closing

Figure 7.2 Prestrike modeling in EMTP

7.2 Simulation results

7.2.1 Single simulation with fixed closing times

For the initial switching transient analysis, the three phases of the Big Eddy-Chemawa line are energized from the Big Eddy bus at 1.18 ms (see the Case 5-03 in Chapter 6). The Big Eddy Chemawa system is modeled considering the guidelines listed in section 7.1, and the prestrike conditions are represented using the model of Figure 7.2. In the following simulations, the linear slope of phase A in Figure 7.1 is considered, where $t_3 = 8$ ms and $u_c = 437$ kV. Figure 7.3 shows the 2-parameter envelope obtained in the EMTP simulation. It is observed the decreasing dielectric strength of the breaker contacts, as they are closing, i.e. from 1.18 ms to 9.18 ms.
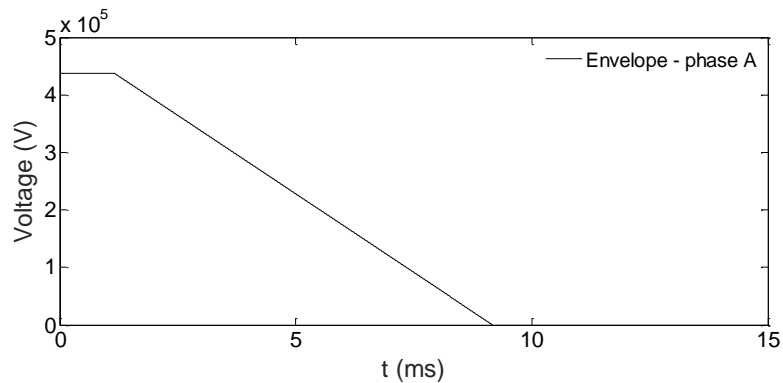
Figure 7.3 Big Eddy breaker dielectric slope of phase A

Figure 7.4 shows the voltages at the Big Eddy. It is observed that several prestrikes appear over the three phases. The maximum overvoltage, i.e., 514.618 kV or 2.73 pu, occurs during the first one. Figure 7.5 shows the voltage at the receiving end of the line, i.e. Chemawa end. It is observed that the maximum overvoltage occurs on phase A, i.e. 852.126 kV or 4.53 pu.

It is demonstrated in Chapter 6 that even though the pattern of the transient voltage waveforms is reproduced very well using frequency-dependent line models, the magnitude of the maximum overvoltage is significantly overestimated unless the effect of corona is considered. Therefore, the simulation of Figure 7.5 is repeated considering the corona effect included in the line model. Figure 7.6 shows the simulation results of voltage of phase A at Chemawa end obtained including the Suliciu corona model. It is observed that the magnitude of the results is effectively reduced

compared with the simulation obtained without corona. The maximum overvoltage obtained with corona is of 3.05 pu, only 0.02 pu greater than the one calculated in Chapter 6, i.e. 3.03 pu.
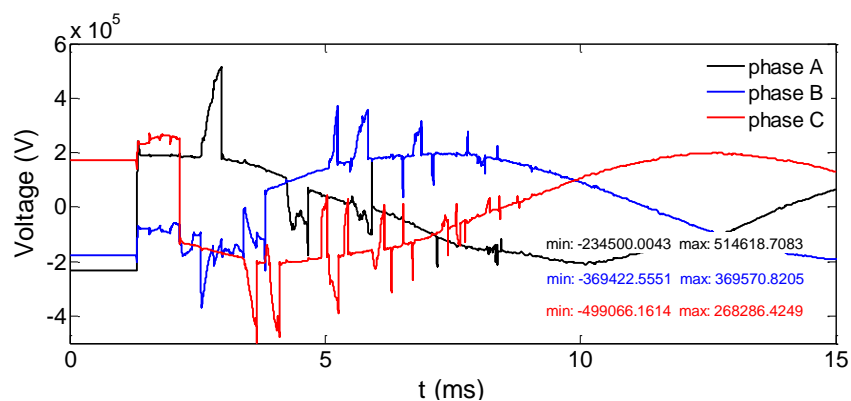
Figure 7.4 Voltages at Big Eddy end
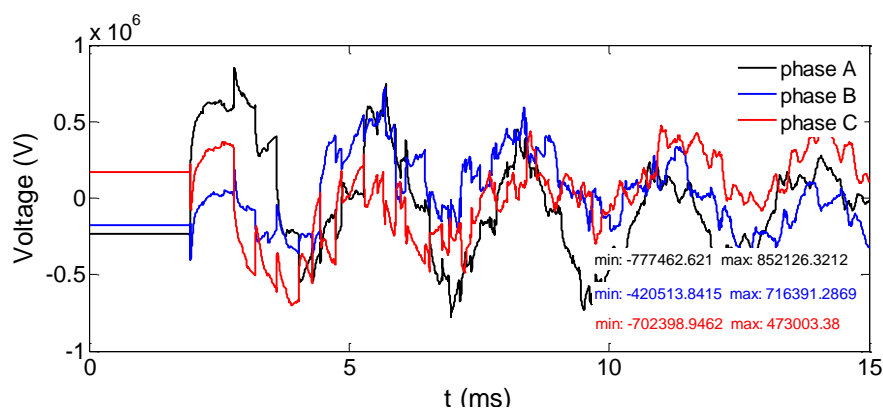
Figure 7.5 Voltages at Chemawa end
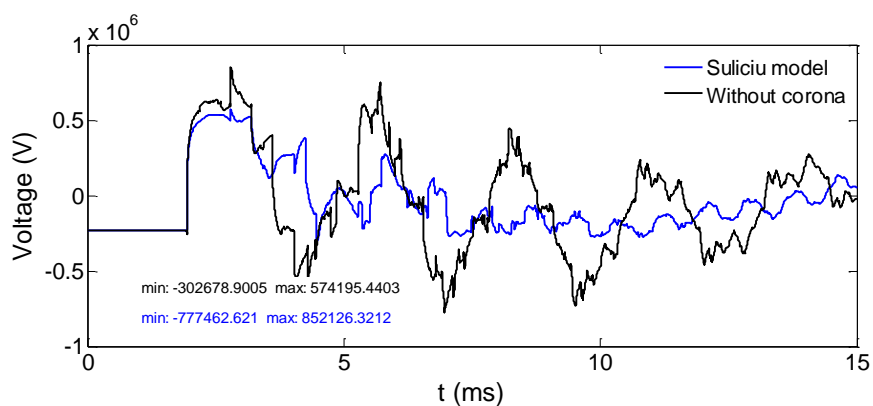
Figure 7.6 Voltage of phase A at Chemawa end

7.2.2 Simulations with systematic closing times over a complete cycle

In this test, the Big Eddy breaker closing times of the three phases are uniformly varied over a complete 60 Hz cycle by increments of 1 electrical degree, i.e. 1/360 cycles. The prestrike conditions are represented using the model of Figure 7.2 at each simulation. Figure 7.7 shows the closing times. The purpose of this test is to obtain a statistical distribution of overvoltage and to determine the instant when the highest overvoltage occurs. Figure 7.8 and Figure 7.9 show respectively the maximum and minimum overvoltage values obtained at Chemawa end. The maximum overvoltage, 4.79 pu, is obtained in the simulation 5 (after 5/360 cycle), i.e. at 1.585 ms, while the minimum values, -4.2 pu, is obtained in the simulation 2 (after 2/360 cycle), i.e. at 1.446 ms. Figure 7.10 shows the time domain results of the voltage at Chemawa of the simulation 5. Figure 7.11 compares the waveform of phase A with the results obtained by including corona in the model. It is observed that the maximum overvoltage value in the simulation with corona is 2.99 pu. It is noted that the maximum overvoltage recorded in the tests of [64] is of 3.01 pu.
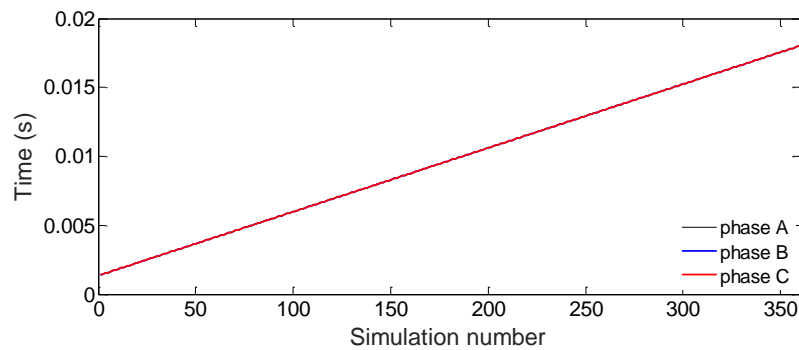
Figure 7.7 Systematic switching times
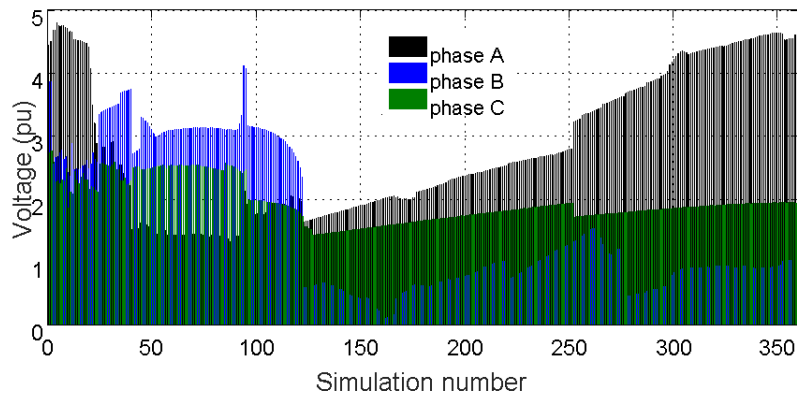
Figure 7.8 Maximum overvoltages from 360 simulations

Figure 7.9 Minimum overvoltages from 360 simulations
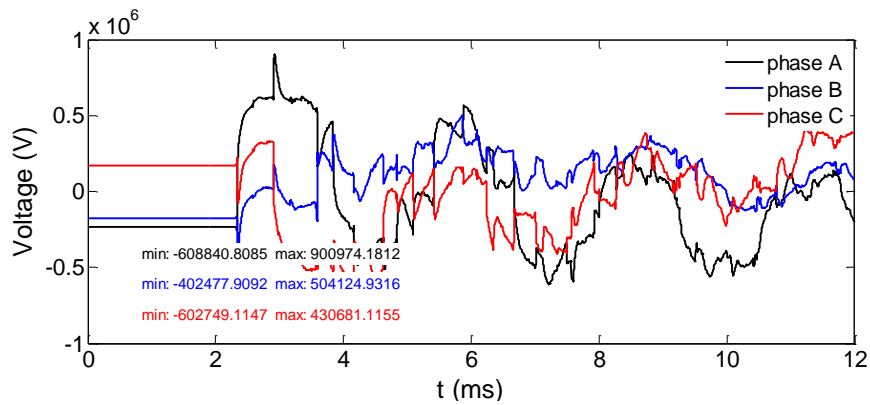
Figure 7.10 Voltages at Chemawa end, simulation 5
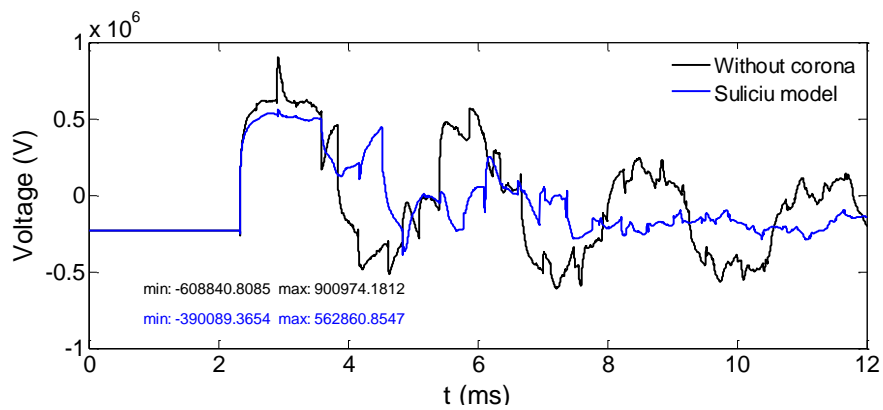
Figure 7.11 Voltage of phase A at Chemawa end, simulation 5

7.2.3 Simulations with random closing times

The simulation results of the previous section provide the switching time value for obtaining the highest overvoltage over a complete 60 Hz cycle, i.e., 1.585 ms. This switching time is used as a

mean time value μ in the following statistical study. In the new set of simulations, the three phases are not closed simultaneously. The closing times for the three phases are found by a Gaussian law considering the mean time μ as reference (see Figure 7.12). It is reported in [64] that the maximum closing time difference between the phases in the Big Eddy breaker is approximately 3.7 ms, i.e. the pole span. Thus, the standard deviation σ used in the simulations of this section is set to 0.6 ms. For this test, the total number of simulations is 300. The prestrike conditions are represented using the model of Figure 7.2 at each simulation. The cumulative distribution of random switching data is presented in Figure 7.13 (phase A). The calculated mean and standard deviation are shown on the top of the graph (see Figure 7.13).
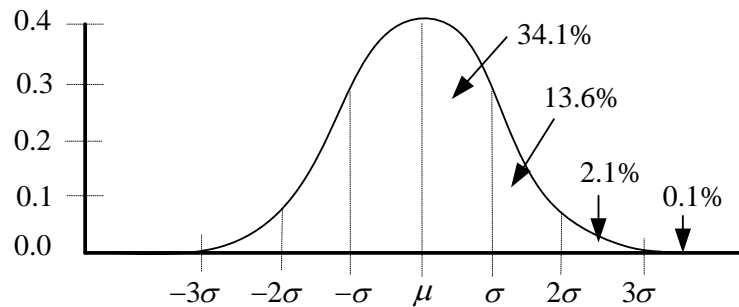
Figure 7.12 Gaussian distribution
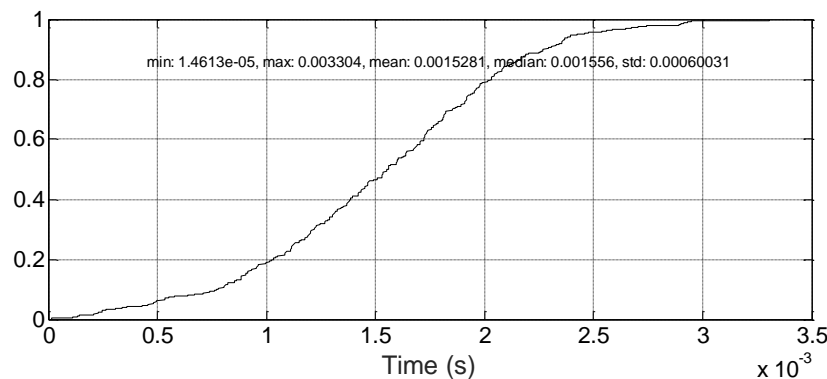
Figure 7.13 Cumulative distribution function

Figure 7.14 shows the results of the maximum overvoltage values obtained at Chemawa end. The maximum overvoltage is obtained in the simulation 146, i.e. 4.79 pu. The switching times of the three phases in the simulation are: $t_a = 1.446$ ms, $t_b = 2.286$ ms and $t_c = 1.311$ ms. Figure 7.15 shows the corresponding waveforms of the voltage at Chemawa end. Figure 7.16 compares the waveform of phase A with the results obtained by including corona in the model. The maximum overvoltage value in the simulation with corona is of 2.99 pu.
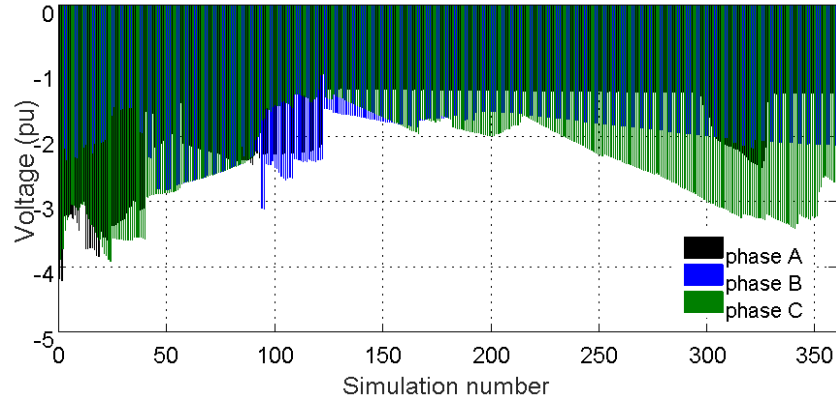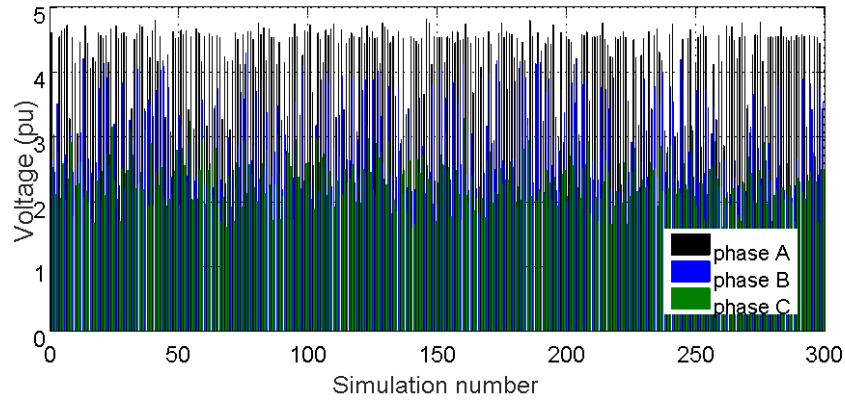
Figure 7.14 Maximum overvoltages from 300 simulations
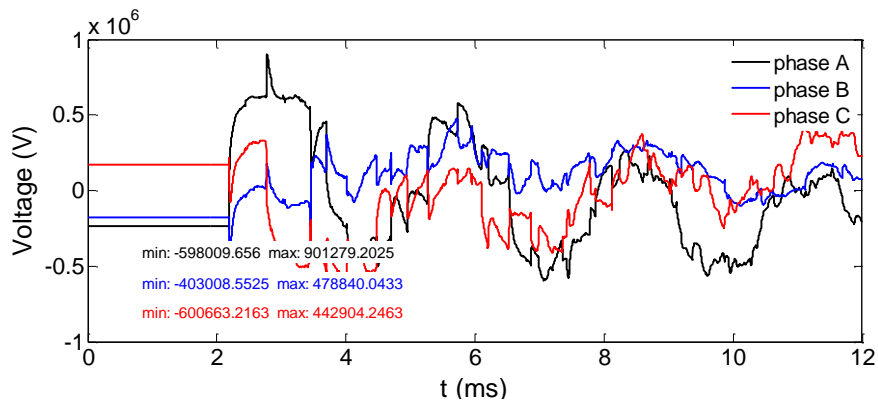
Figure 7.15 Voltages at Chemawa end, simulation 146
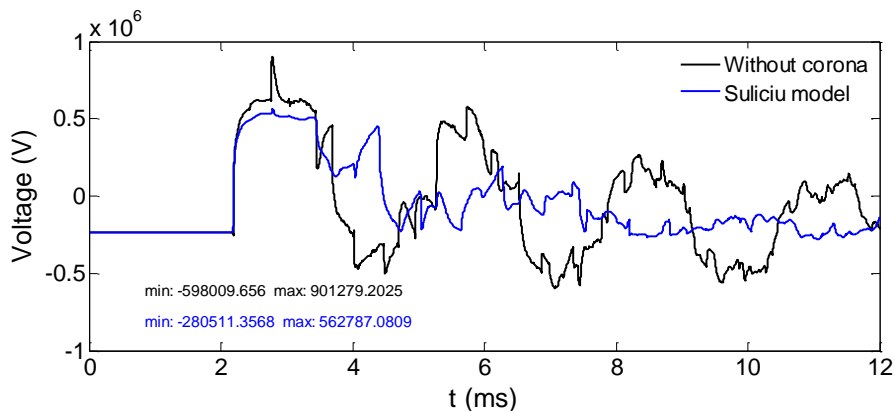
Figure 7.16 Voltage of phase A at Chemawa end, simulation 146

Although the maximum overvoltage occurs in simulation 146 (Figure 7.14), it is observed that there are other values that are frequently repeated. Figure 7.17 shows the maximum values observed in Figure 7.14. Figure 7.18 presents the histogram of Figure 7.14. It is observed in Figure 7.18 that the value 4.52 appears 25 times (e.g. in simulation 66), while the maximum

value, i.e. 4.79 pu, appears only once. The switching times of the three phases in simulation 66 are: $t_a = 1.446$ ms, $t_b = 2.286$ ms and $t_c = 1.311$ ms. Figure 7.19 shows the waveforms of voltage at Chemawa end. Figure 7.20 compares the waveform of phase A with the results obtained by including corona in the model. The maximum overvoltage in the simulation with corona is of 2.99 pu.
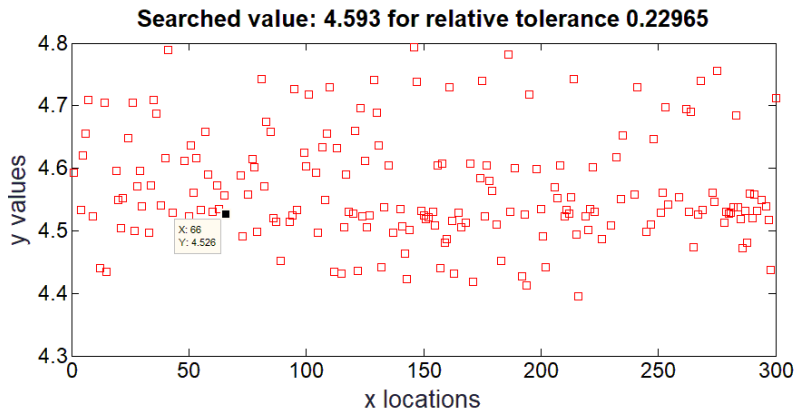
Figure 7.17 Maximum values obtained in Figure 7.14
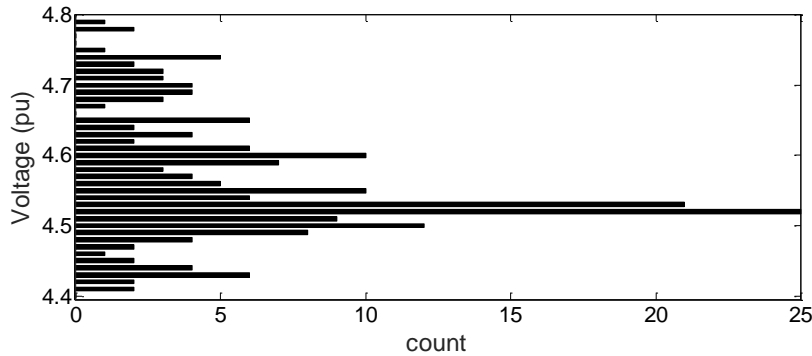
Figure 7.18 Histogram of Figure 7.17
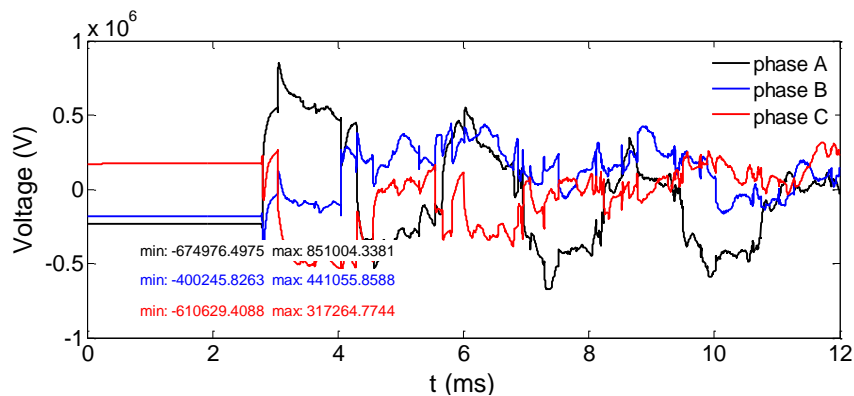
Figure 7.19 Voltages at Chemawa end, simulation 66

Figure 7.20 Voltage of phase A at Chemawa end, simulation 66

Finally, Figure 7.21 shows the results of the minimum overvoltage values obtained at Chemawa end. The minimum overvoltage is found on phase C in the simulation 32, i.e. -4.53 pu. The switching times of the three phases are: $t_a = 0.1443$ ms, $t_b = 0.8577$ ms and $t_c = 2.705$ ms. Figure 7.22 shows the time domain results of the voltage at Chemawa end. Figure 7.23 compares the waveform of phase C with the results obtained by including corona in the model. The minimum overvoltage value in the simulation with corona is of -2.89 pu.

Figure 7.21 Minimum overvoltages values from 300 simulations
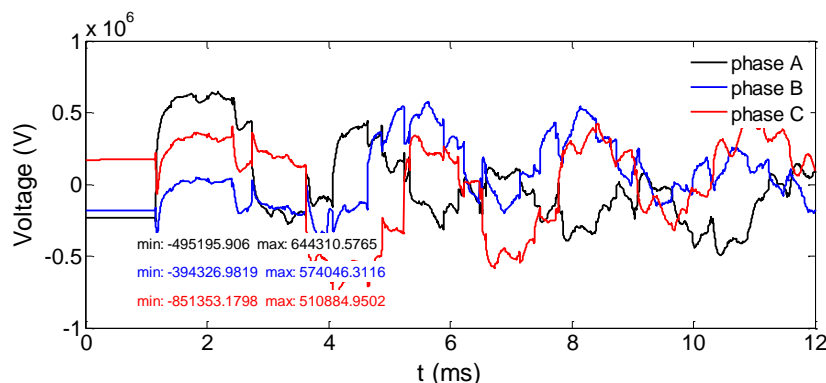
Figure 7.22 Voltages at Chemawa end, simulation 32
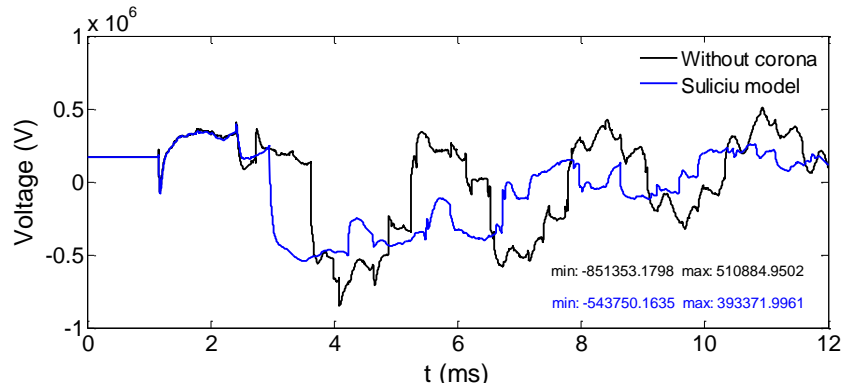
Figure 7.23 Voltage of phase C at Chemawa end, simulation 32

7.2.4 Simulations with random prestrike times

Although the dielectric slope characteristic of the breaker contacts can be used to represent the prestrike conditions, the actual prestrike times may be very random. To represent the highly statistical nature of this phenomenon, a new set of 300 simulations is performed, where the prestrike times are determined by the Gaussian law. Since the maximum overvoltage occurs during the first prestrike, only one prestrike event is modeled in this test. Figure 7.24 shows the selections in the switching model used in EMTP. Following the sequence of the switching events, SW4 stands for the first closing time, SW5 stands for opening time, and SW6 stands for the final closing time. The mean and standard deviation values are selected based on the analysis of prestrike data available from [64].

Switch	Condition	Dependency	Mean value μ (ms)	Standard deviation σ (ms)
SW4	Closing	Master	1.585	0.60
SW5	Opening	Slave SW4	0.450	0.10
SW6	Closing	Slave SW5	0.700	0.23
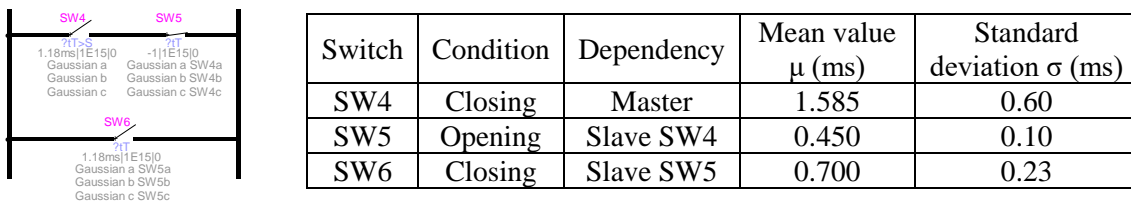
Figure 7.24 Prestrike model with random times

Figure 7.25 shows the cumulative distribution for the switches SW4, SW5 and SW6. The calculated mean and standard deviation values are shown on the top of the graph. Figure 7.26 shows the calculated times (t_{stat}) and the actual event times ($t_{stat-real}$) of phase B in SW5. It is observed that some timings do not coincide since the actual (real) opening is occurring on current crossing zero. This means that there are some of the simulations where the switch does not open within the simulation interval, i.e. there is no prestrike on phase B in those simulations.
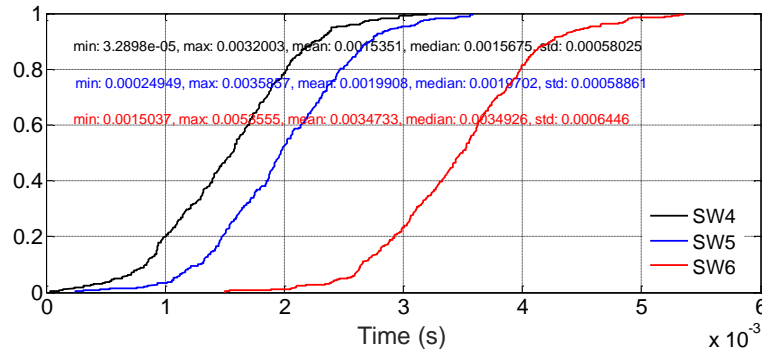
Figure 7.25 Cumulative distribution function
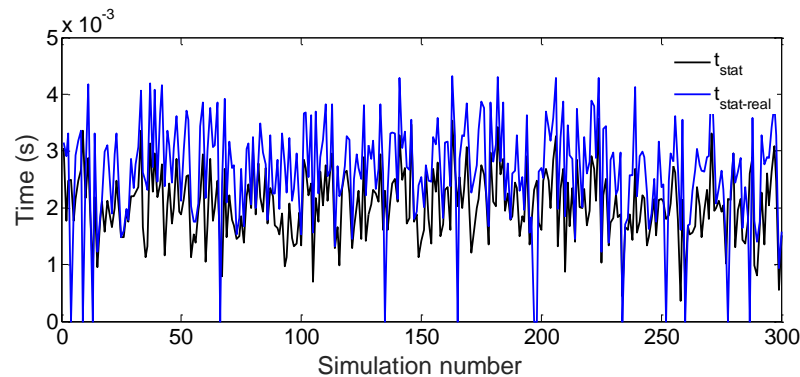

Figure 7.26 Comparison of the statistical and real switching times of phase B

Figure 7.27 shows the results of the maximum overvoltage values obtained at Chemawa end. Figure 7.28 shows the maximum values obtained in Figure 7.27. It is observed that the maximum value, 4.78 pu, occurs in simulation 246. The sequence of switching times is listed in Table 7.1. Figure 7.29 shows the time-domain results of the voltage at Chemawa of simulation 246. Figure 7.30 compares the waveform of phase A with the results obtained by including corona in the model. The maximum overvoltage value in the simulation with corona is 2.98 pu.
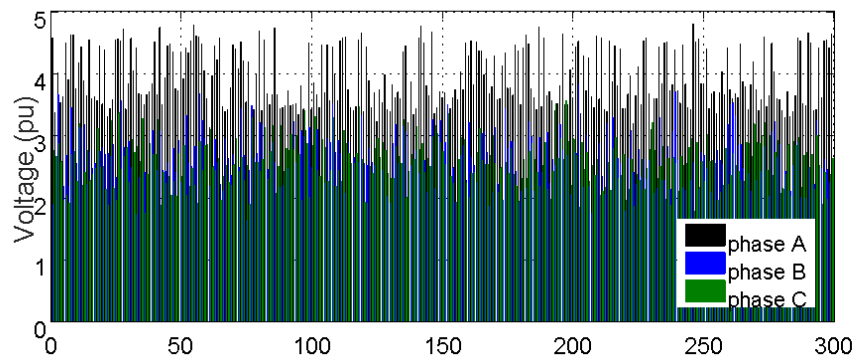

Figure 7.27 Maximum overvoltages values from 300 simulations
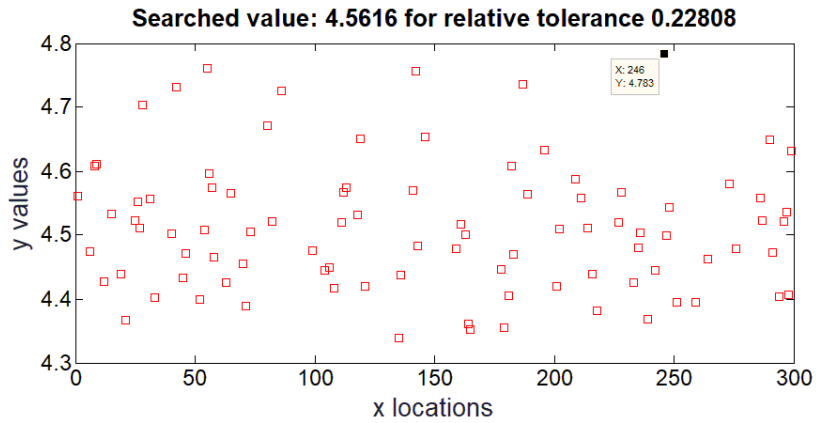
Figure 7.28 Maximum values obtained in Figure 7.27

Table 7.1 Sequence of switching events in simulation 246

| Phase	Closes (ms)	Opens (ms)	Closes (ms)
A	1.442	2.711	3.466
B	1.555	1.897	3.551
C	2.017	3.383	3.906
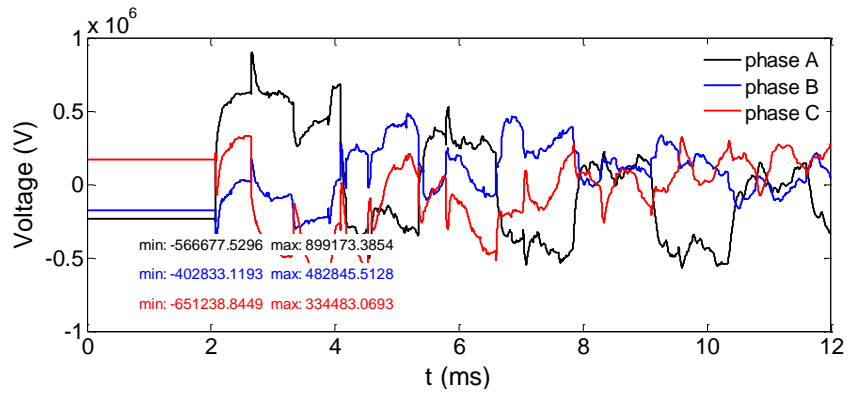
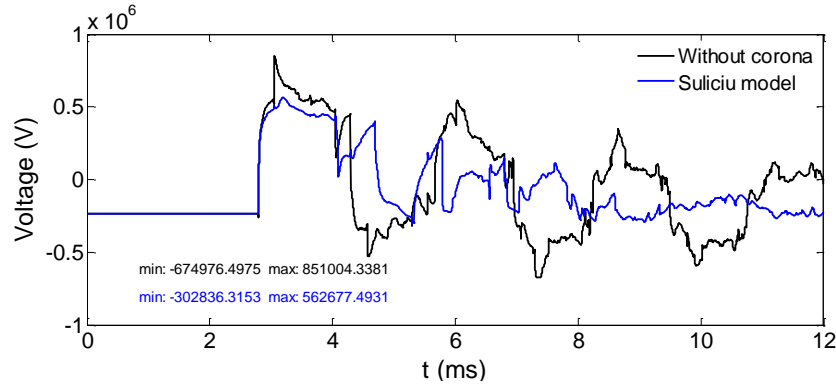Figure 7.29 Voltages at Chemawa end, simulation 246
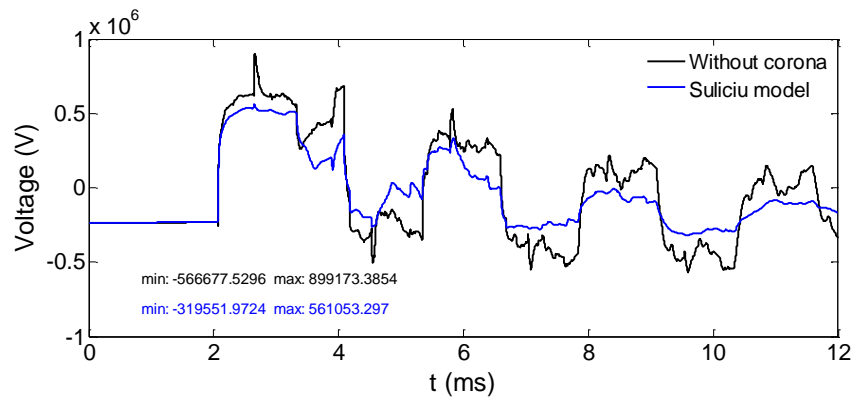
Figure 7.30 Voltage of phase A at Chemawa end, simulation 246

Finally, Figure 7.31 shows the results of the minimum overvoltage values obtained at Chemawa end. The minimum overvoltage is obtained on phase C in the simulation 152, i.e. -4.75 pu. The sequence of switching times is listed in Table 7.2. Figure 7.32 shows the time-domain results of the voltage at Chemawa end. Figure 7.33 compares the waveform of phase C with the results obtained by including corona in the model. The minimum overvoltage value in the simulation with corona is of -3.12 pu.
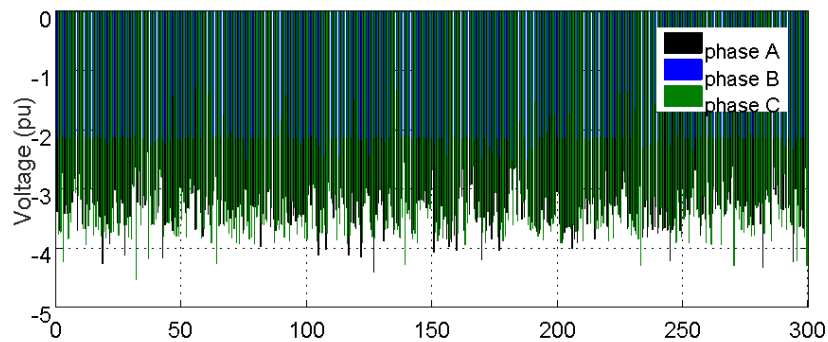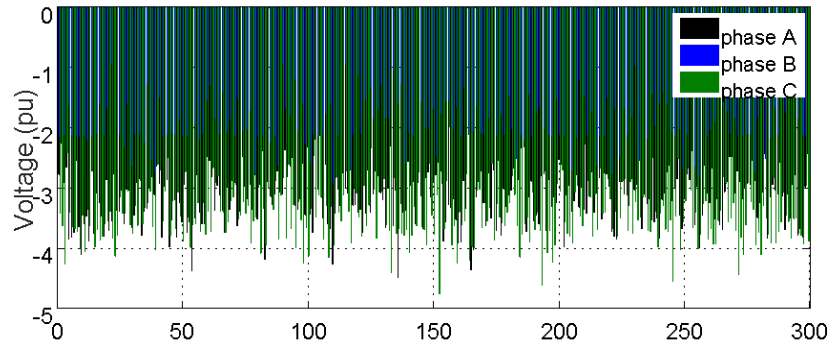

Figure 7.31 Minimum overvoltages values from 300 simulations

Table 7.2 Sequence of switching events in simulation 152

Phase	Closes (ms)	Opens (ms)	Closes (ms)
A	1.100	2.362	2.790
B	2.082	2.743	4.299
C	2.825	4.167	4.851
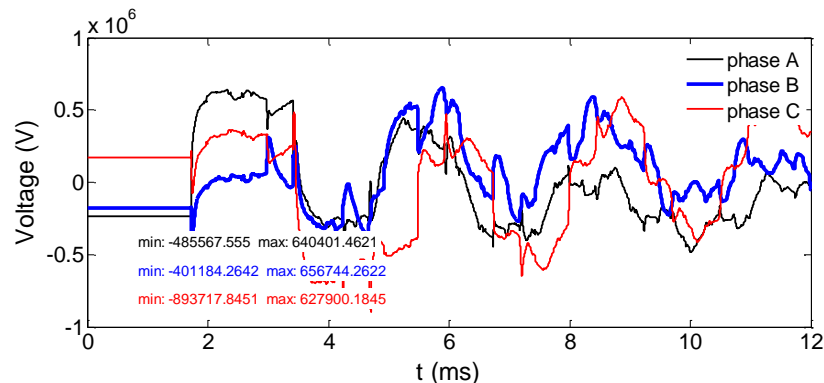
Figure 7.32 Voltages at Chemawa end, simulation 152
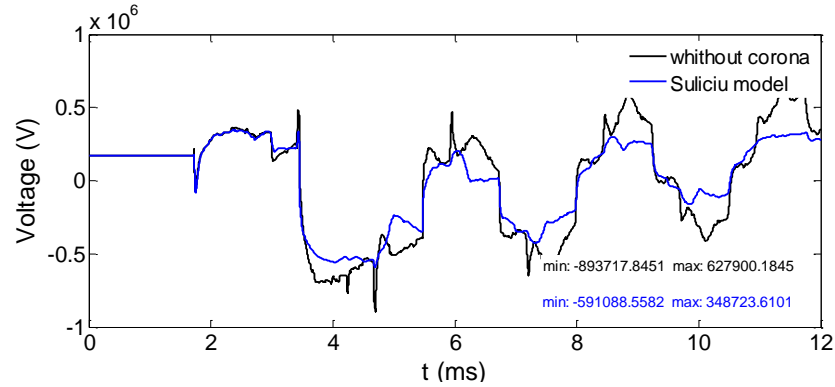
Figure 7.33 Voltage of phase C at Chemawa end, simulation 152

7.2.5 Summary of results

Table 7.3 shows the summary of results obtained in this chapter. For comparison purposes, Test 3 is repeated using 500 simulations. It is observed that identical values are obtained in all the tests. It is noted that the maximum overvoltage recorded in the field data in [64] is of 3.01 pu.

Table 7.3 Summary of results

Test	Closing times	Prestrike model	Number of simulations	Maximum overvoltage (pu)	
				Without corona	With corona
1	Varied uniformly over a complete cycle	Deterministic (linear slope)	360	4.79	2.99
2	Varied randomly (Gaussian law)	Deterministic (linear slope)	300	4.79	2.99
3	Varied randomly (Gaussian law)	Random (Gaussian law)	300	4.78	2.98
4	Varied randomly (Gaussian law)	Random (Gaussian law)	500	4.78	2.98

7.3 Conclusions

This chapter presents a statistical study to determine the worst overvoltage at the receiving end of a line with a trapped charge during high-speed reclosing. For the statistical simulations, the voltage versus time characteristic (dielectric slope) for the breaker is automatically represented. The utilized model enables the breaker conduction when its voltage withstand is reached. When the breaker is closing, if the voltage at the terminal of the breaker reaches the envelope of the voltage withstand, the gap is closed and opened again when the current crosses zero.

The simulation tests performed in this chapter are summarized as follows. First, the breaker closing times of the three phases are systematically varied over a complete 60 Hz cycle to obtain a uniform distribution of overvoltage. Once the simulation with the highest overvoltage is found, a subsequent set of simulations is performed, where the closing times for the three phases are calculated by a Gaussian law. Moreover, to represent the highly statistical nature of prestrike phenomenon, an additional set of simulations is performed where the prestrike times are also determined by the Gaussian law.

For running the statistical simulations, the corona model is not included. However, the simulation with the highest overvoltage is compared afterwards with the one obtained by including corona. Simulations results demonstrate that the estimated maximum overvoltage shows a good agreement with the one recorded in the field tests.

CHAPTER 8   CONCLUSION

8.1 Summary of thesis

The main objective of this thesis is to investigate the modeling practice required to obtain more accurate and faster time-domain simulations using frequency-dependent line and cable models. The most important contributions of this PhD project are summarized as follows.

Review of current models

Various cases of study have been used to evaluate the performance of the most common line models in time-domain simulations. It is verified that phase-domain based models provide highly accurate results for the simulation of coupling effects between parallel conductors, compared to modal-domain based models. The drawbacks of phase-domain models are numerical instability issues due to the presence of high residue pole ratios and inaccurate phase-domain fitting procedures, and they have been demonstrated through the simulation of practical cases.

Improved identification procedure for the propagation function in cables

This thesis proposes an improved fitting procedure for the accurate identification of the propagation function of cables while maintaining reduced order of approximation. In the proposed method, frequency-domain partitioning and adaptive weighting techniques are directly applied in the phase domain for the identification of poles and residues simultaneously. This procedure ensures the fitting precision of all entries including the low-magnitude off-diagonal elements. The order of approximation is reduced by post-processing the fitting using the balanced realization technique. It is demonstrated that when the proposed methodology is combined with more precise integration schemes allows obtaining more accurate time-domain simulations, especially for induced voltages. In addition, the proposed method complements the prevailing ULM by eliminating spurious oscillations or numerical instabilities due to opposing high residue pole pairs coming from different but close delay groups regardless of the integration scheme.

Improved DC response

To improve the DC response in transmission lines, this thesis proposes a two-stage fitting method in which low frequency samples are given priority. The fitting is performed in a two-stage fashion ensuring precise fitting primarily at frequencies near DC. This method also complements

the prevailing universal line model by avoiding pairs with large residue pole ratios, and by improving the computation of DC steady-state waveforms when necessary.

Adaptive line model

To increase the speed of simulations, this thesis presents an adaptive transmission line model based on switching between WB and CP models. The WB model is used during a transient where detailed models are required whereas the CP model is used in steady-state. The switching between the two models is performed by modifying the terms of the history current vectors and their corresponding elements in the nodal admittance matrix during the simulation. The proposed model includes an algorithm that enables the automatic setting of the line model throughout the simulation. Numerical results have shown that the proposed adaptive model provides faster simulations than the one from the WB model without significant loss of accuracy.

Validation of line models with field test

One more contribution of this thesis is to validate transmission line model with field test and to understand the major factors implied in reproducing field measurements using simulations. It is demonstrated that even though the pattern of the transient voltage waveforms is reproduced very well using frequency-dependent line models, simulations results are significantly overestimated unless the effect of corona is included. Two types of corona models have been tested and both models have demonstrated that corona is the primary factor that allows the simulations to correctly reproduce field measurements, as presented in this thesis for a 230-kV line. It is remarked that for the conventional situations where switching surges are controlled to lower levels using surge arresters, closing resistors or where trapped charge is removed prior to closing, EMT-type programs using standard modeling techniques, are considerably more accurate.

Statistical switching overvoltages

Once a line model is validated it is possible to proceed with statistical simulation phase to identify the worst-case overvoltage. For the statistical simulations, the voltage versus time characteristic (dielectric slope) for the breaker has been represented either by a linear slope or by random switching times calculated by the Gaussian law. For running the statistical simulations, the corona model is not included. However, the simulation results are compared afterwards with the ones obtained by including corona. Numerical results have shown that the difference between the calculated maximum overvoltage and the one from measurements is 0.02 pu.

8.2 List of publications

The following is a list of journal and conference articles that originated from this Ph.D. project.

Journal publications

1) **M. Cervantes**, I. Kocar, J. Mahseredjian and A. Ramirez "**Accurate and Reduced Order Identification of Propagation Function for Electromagnetic Transient Analysis of Cables**," IEEE Trans. on Power Del., (Early Access Article), 2019.

2) **M. Cervantes**, I. Kocar, J. Mahseredjian and A. Ramirez "**Partitioned Fitting and DC Correction for the Simulation of Electromagnetic Transients in Transmission Lines/Cables**," IEEE Trans. on Power Del., vol. 33, pp. 3246-3248, 2018.

3) **M. Cervantes**, I. Kocar, A. Montenegro, D. Goldsworthy, T. Tobin, J. Mahseredjian, R. Ramos, J. Marti, T. Noda, A. Ametani, and C. Martin, "**Simulation of Switching Overvoltages and Validation with Field Tests**," IEEE Trans. on Power Del., vol. 33, pp. 2884-2893, Dec 2018.

Conference publications

1) **M. Cervantes**, I. Kocar, J. Mahseredjian and A. Ramirez "**Partitioned Fitting and DC Correction in Transmission Line/Cable Models**", International Conference on Power Systems Transients (IPST'2019), June 2019, Perpignan, France.

2) **M. Cervantes**, I. Kocar, A. Ramirez "**Review of Transmission Line Models for Electromagnetic Transients Analysis**", The papers of technical meeting on high voltage engineering, IEE Japan (IEEJ-HV), paper HV-18-92, August 2018, Montreal, Canada.

3) A. Ametani, H. Xue, **M. Cervantes**, I. Kocar, T. Noda "**A Study on the Effect of a Source Circuit on Switching Surges**", The papers of technical meeting on high voltage engineering, IEE Japan (IEEJ-HV), paper HV-18-7, January 2018, Japan.

4) **M. Cervantes**, "**Adaptive Transmission Line/Cable Models for the Simulation of Electromagnetic Transients**", 11th International Symposium on EMC and Transients in Infrastructures and 13th International Student Session (ISET-ISS'2017), paper ISET-04, Kyoto, Japan.

8.3 Future work

Considering the general scope of this thesis, which is based on electromagnetics transient simulations using frequency-dependent line/cable models, possible developments are as follows.

Further improvements of fitting procedures

The two fitting procedures proposed in Chapter 3 have been applied separately, i.e. to improve either transient simulations (applying WFP-MOR) or DC response (applying FDM/DC). Therefore, a further investigation would be the application of both techniques together to achieve better performance and to further improve fitting precision.

Improvements of the adaptive line model

The proposed adaptive method enables the automatic setting of the line model, i.e. switching between WB and CP models, along the simulation. However, the proposed techniques have been implemented to simulate a simple network. Therefore, further implementation improvements are required to apply the proposed adaptive model in multi-scale networks. In addition, initialisation with harmonics could be also investigated.

REFERENCES

[1] N. Nagaoka and A. Ametani, "A development of a generalized frequency-domain transient program-FTP," IEEE Trans. Power Delivery, vol. 3, pp. 1996-2004, 10/ 1988.

[2] P. Moreno and A. Ramirez, "Implementation of the numerical Laplace transform: A review," IEEE Trans. Power Delivery, vol. 23, pp. 2599-2609, 2008.

[3] H. W. Dommel, Electromagnetic Transients Program: Reference Manual: (EMTP Theory Book): Bonneville Power Administration, 1986.

[4] N. Watson, J. Arrillaga, and I. o. E. Engineers, Power Systems Electromagnetic Transients Simulation: Institution of Engineering and Technology, 2003.

[5] H. W. Dommel, "Digital computer solution of electromagnetic transients in single and multiphase networks," IEEE Trans. Power App. and Syst., vol. pas-88, pp. 388-99, 1969.

[6] A. Budner, "Introduction of frequency-dependent line parameters into an electromagnetic transients program," IEEE Trans. Power App. and Syst., vol. PAS-89, pp. 88-97, 1970.

[7] J. K. Snelson, "Propagation of travelling waves on transmission lines - frequency dependent parameters," IEEE Trans. Power Apparatus and Systems, vol. PAS-91, pp. 85-91, 1972.

[8] W. S. Meyer and H. W. Dommel, "Numerical modeling of frequency–dependent Transmission–Line parameters in an electromagnetic transients program," IEEE Trans. Power Apparatus and Systems, vol. PAS-93, pp. 1401-1409, 1974.

[9] A. Semlyen and A. Dabuleanu, "Fast and accurate switching transient calculations on transmission lines with ground return using recursive convolutions," IEEE Trans. Power Apparatus and Systems, vol. PAS-94, pp. 561-571, 1975.

[10] A. Semlyen, "Contributions to the theory of calculation of electromagnetic transients on transmission lines with frequency dependent parameters," IEEE Trans. Power Apparatus and Systems, vol. PAS-100, pp. 848-856, 1981.

[11] A. Ametani, "A highly efficient method for calculating transmission line transients," IEEE Trans. Power Apparatus and Systems, vol. PAS-95, pp. 1545-51, 1976.

[12] J. R. Marti, "Accurate modelling of frequency-dependent transmission lines in electromagnetic transient simulations," IEEE Trans. Power Apparatus and Systems, vol. PAS-101, pp. 147-55, 1982.

[13] A. Semlyen and M. H. Abdel-Rahman, "Transmission line modeling by rational transfer functions," IEEE Trans. Power Apparatus and Systems, vol. PAS-101, 1982.

[14] L. Marti, "Simulation of transients in underground cables with frequency-dependent modal transformation matrices," IEEE Trans. Power Delivery, vol. 3, pp. 1099-1110, 1988.

[15] B. Gustavsen and A. Semlyen, "Simulation of transmission line transients using vector fitting and modal decomposition," IEEE Trans. Power Delivery, vol. 13, pp. 605-614, 1998.

[16] H. Nakanishi and A. Ametani, "Transient calculation of a transmission line using superposition law," IEE Proceedings C - Generation, Transmission and Distribution, vol. 133, pp. 263-269, 1986.

[17] B. Gustavsen, J. Sletbak, and T. Henriksen, "Calculation of electromagnetic transients in transmission cables and lines taking frequency dependent effects accurately into account," IEEE Trans. Power Delivery, vol. 10, pp. 1076-84, 1995.

[18] H. V. Nguyen, H. W. Dommel, and J. R. Marti, "Direct phase-domain modelling of frequency-dependent overhead transmission lines," IEEE Trans. Power Delivery, vol. 12, pp. 1335-1342, 1997.

[19] B. Gustavsen and A. Semlyen, "Combined phase and modal domain calculation of transmission line transients based on vector fitting," IEEE Trans. Power Delivery, vol. 13, pp. 596-604, 1998.

[20] G. Angelidis and A. Semlyen, "Direct phase-domain calculation of transmission line transients using two-sided recursions," IEEE Trans. Power Delivery, vol. 10, pp. 941-949, 1995.

[21] T. Noda, N. Nagaoka, and A. Ametani, "Phase domain modeling of frequency-dependent transmission lines by means of an ARMA model," IEEE Trans. Power Delivery, vol. 11, pp. 401-411, 1996.

[22] T. Noda, N. Nagaoka, and A. Ametani, "Further improvements to a phase-domain ARMA line model in terms of convolution, steady-state initialization, and stability," IEEE Trans. Power Delivery, vol. 12, pp. 1327-1334, 1997.

[23] F. Castellanos, J. R. Martí, and F. Marcano, "Phase-domain multiphase transmission line models," Int. Journal of Electrical Power & Energy Systems, vol. 19, pp. 241-248, 1997.

[24] F. J. Marcano and J. R. Marti, "Idempotent line model: Case studies." International Conference on Power Systems Transients (IPST), Seattle, USA. 1997.

[25] B. Gustavsen and A. Semlyen, "Calculation of transmission line transients using polar decomposition," IEEE Trans. Power Delivery, vol. 13, pp. 855-862, 1998.

[26] F. Castellanos and J. R. Marti, "Full frequency-dependent phase-domain transmission line model," IEEE Trans. Power Systems, vol. 12, pp. 1331-1336, Aug 1997.

[27] A. Morched, B. Gustavsen, and M. Tartibi, "A universal model for accurate calculation of electromagnetic transients on overhead lines and underground cables," IEEE Trans. Power Delivery, vol. 14, pp. 1032-1038, 1999.

[28] B. Gustavsen, "Time delay identification for transmission line modeling," Signal Propagation on Interconnects, Proceedings, pp. 103-106, 2004.

[29] L. De Tommasi and B. Gustavsen, "Accurate transmission line modeling through optimal time delay identification," International Conference on Power Systems Transients (IPST), Lyon, France, 2007.

[30] I. Kocar and J. Mahseredjian, "New procedure for computation of time delays in propagation function fitting for transient modeling of cables," IEEE Trans. Power Delivery, vol. 31, pp. 613-621, 2016.

[31] B. Gustavsen and J. Nordstrom, "Pole identification for the universal line model based on trace fitting," IEEE Trans. Power Delivery, vol. 23, pp. 472-479, 2008.

[32] B. Gustavsen, "Passivity enforcement for transmission line models based on the method of characteristics," IEEE Trans. Power Delivery, vol. 23, pp. 2286-2293, 2008.

[33] H. M. J. D. Silva, A. M. Gole, J. E. Nordstrom, and L. M. Wedepohl, "Robust passivity enforcement scheme for time-domain simulation of multi-conductor transmission lines and cables," IEEE Trans. Power Delivery, vol. 25, pp. 930-938, 2010.

[34] A. Semlyen and B. Gustavsen, "Phase-domain transmission-line modeling with enforcement of symmetry via the propagated characteristic admittance matrix," IEEE Trans. Power Delivery, vol. 27, pp. 626-631, 2012.

[35] O. Ramos-Leanos, J. L. Naredo, J. Mahseredjian, C. Dufour, J. A. Gutierrez-Robles, and I. Kocar, "A wideband line/cable model for real-time simulations of power system transients," IEEE Trans. Power Delivery, vol. 27, pp. 2211-2218, 2012.

[36] I. Kocar, J. Mahseredjian, and G. Olivier, "Improvement of numerical stability for the computation of transients in lines and cables," IEEE Trans. Power Delivery, vol. 25, pp. 1104-1111, 2010.

[37] B. Gustavsen, "Avoiding numerical instabilities in the universal line model by a two-segment interpolation scheme," IEEE Trans. Power Delivery, vol. 28, pp. 1643-1651, 2013.

[38] O. Ramos-Leanos, J. Mahseredjian, J. L. Naredo, I. Kocar, J. A. Gutierrez-Robles, and J. A. Martinez, "Phase-domain line/cable model through second-order blocks," IEEE Trans. Power Delivery, vol. 30, pp. 2460-2467, 2015.

[39] I. Kocar and J. Mahseredjian, "Accurate frequency dependent cable model for electromagnetic transients," IEEE Trans. Power Delivery, vol. 31, pp. 1281-1288, 2016.

[40] B. Gustavsen and A. Semlyen, "Rational aproximations of frequency domain responses by vector fitting," IEEE Trans. Power Delivery, vol. 14, pp. 1052–1061, 1999.

[41] B. Gustavsen, "Computer code for rational approximation of frequency dependent admittance matrices," IEEE Trans. Power Delivery, vol. 17, pp. 1093-1098, 2002.

[42] B. Gustavsen, "Improving the pole relocating properties of vector fitting," IEEE Trans. Power Delivery, vol. 21, pp. 1587-1592, 2006.

[43] D. Deschrijver, M. Mrozowski, T. Dhaene, and D. De Zutter, "Macromodeling of multiport systems using a fast implementation of the vector fitting method," IEEE Microwave and Wireless Components Letters, vol. 18, pp. 383-385, 2008.

[44] D. Deschrijver and T. Dhaene, "Broadband macromodelling of passive components using orthonormal vector fitting," Electronics Letters, vol. 41, pp. 1160-1161, 2005.

[45] I. Kocar, J. Mahseredjian, and G. Olivier, "Weighting method for transient analysis of underground cables," IEEE Trans. Power Delivery, vol. 23, pp. 1629-1635, 2008.

[46] T. K. Sarkar and O. Pereira, "Using the matrix pencil method to estimate the parameters of a sum of complex exponentials," IEEE Antennas and Propagation Magazine, vol. 37, pp. 48-55, 1995.

[47] K. Sheshyekani, H. R. Karami, P. Dehkhoda, M. Paolone, and F. Rachidi, "Application of the matrix pencil method to rational fitting of frequency-domain responses," IEEE Trans. Power Delivery, vol. 27, pp. 2399-2408, 2012.

[48] K. Sheshyekani and B. Tabei, "Multiport frequency-dependent network equivalent using a modified matrix pencil method," IEEE Trans. Power Delivery, vol. 29, pp. 2340-2348, 2014.

[49] H. Shi, "A closed-form approach to the inverse fourier transform and its applications," IEEE Trans. Electromagnetic Compatibility, vol. 50, pp. 669-677, 2008.

[50] T. Noda, "Identification of a multiphase network equivalent for electromagnetic transient calculations using partitioned frequency response," IEEE Trans. Power Delivery, vol. 20, pp. 1134-1142, 2005.

[51] T. Noda, "A binary frequency-region partitioning algorithm for the identification of a multiphase network equivalent for EMT studies," IEEE Trans. Power Delivery, vol. 22, pp. 1257-1258, 2007.

[52] A. Ramirez, "Vector fitting-based calculation of frequency-dependent network equivalents by frequency partitioning and model-order reduction," IEEE Trans. Power Delivery, vol. 24, pp. 410-415, 2009.

[53] T. Noda, "Application of frequency-partitioning fitting to the phase-domain frequency-dependent modeling of overhead transmission lines," IEEE Trans. Power Delivery, vol. 30, pp. 174-183, 2015.

[54] T. Noda, "Application of frequency-partitioning fitting to the phase-domain frequency-dependent modeling of underground cables," IEEE Trans. Power Delivery, vol. 31, pp. 1776-1777, 2016.

[55] B. Moore, "Principal component analysis in linear systems: Controllability, Observability, and Model Reduction," IEEE Trans. Autom. Control, vol. AC-26, no. 1, pp. 17–32, 1981.

[56] A. Ramirez, A. Mehrizi-Sani, D. Hussein, M. Matar, M. Abdel-rahman, J. d. J. Chavez, et al., "Application of balanced realizations for model order reduction of dynamic power system equivalents," IEEE Trans. Power Delivery, pp. 1-1, 2015.

[57] J. Mahseredjian, Support Routine for the EMTP Dynamic Corona Model. Rapport (IREQ-4534), décembre 1989.

[58] A. Semlyen and H. Wei-Gang, "Corona modelling for the calculation of transients on transmission lines," IEEE Power Engineering Review, vol. PER-6, pp. 57-57, 1986.

[59] P. S. Maruvada, H. Menemenlis, and R. Malewski, "Corona characteristics of conductor bundles under impulse voltages," IEEE Trans. Power Apparatus and Systems, vol. 96, pp. 102-115, 1977.

[60] J. L. Naredo, A. C. Soudack, and J. R. Marti, "Simulation of transients on transmission lines with corona via the method of characteristics," IEE Proceedings - Generation, Transmission and Distribution, vol. 142, pp. 81-87, 1995.

[61] N. Nagaoka, H. Motoyama, and A. Ametani, "Lightning surge calculations including corona effects using a two-conductor model," Electric Power Systems Research, vol. 13, pp. 31-41, 1987.

[62] A. Ramirez, "Transitorios electromagneticos en lineas de transmision considerando parameteros dependientes de la frecuencia y efecto corona," University of Guadalajara, 1998.

[63] M. Mihailescu-Suliciu and I. Suliciu, "A rate type constitutive equation for the description of the corona effect," IEEE Trans. Power App. and Syst., vol. PAS-100, pp. 3681-5, 1981.

[64] S. M. Lowder, J. L. Randall, and D. Goldsworthy, "Big Eddy-Chemawa 230-kV line switching and transformer saturation test," Bonneville Power Administration, Report TTL(E) 96-11, June 7-8, 1995.

[65] E. V. Larsen, R. A. Walling, and C. J. Bridenbaugh, "Parallel AC/DC transmission lines steady-state induction issues," IEEE Trans. Power Delivery, vol. 4, no. 1, pp. 667–674, 1989.

[66] R. Verdolin, A. M. Gole, E. Kuffel, N. Diseko, and B. Bisewski, "Induced overvoltages on an AC-DC hybrid transmission system," IEEE Trans. Power Delivery, vol. 10, no. 3, pp. 1514–1524, 1995.

[67] B. Gustavsen, G. Irwin, R. Mangerlod, D. Brandt, and K. Kent, "Transmission line models for the simulation of interaction phenomena between parallel AC and DC overhead lines," International Conference on Power Systems Transients (IPST), Budapest, Hungary, 1999.

[68] O. M. K. K. Nanayakkara, A. D. Rajapakse, and R. Wachal, "Location of DC line faults in conventional HVDC systems with segments of cables and overhead lines using terminal measurements," IEEE Trans. Power Delivery, vol. 27, pp. 279-288, 2012.

[69] H. M. J. De Silva, A. M. Gole, and L. M. Wedepohl, "Accurate electromagnetic transient simulations of HVDC cables and overhead transmission lines," International Conference on Power System Transients (IPST), Lyon, France, 2007.

[70] A. Ramirez and R. Iravani, "Enhanced fitting to obtain an accurate DC response of transmission lines in the analysis of electromagnetic transients," IEEE Trans. Power Delivery, vol. 29, no. 6, pp. 2614–2621, Dec. 2014.

[71] K. Strunz, R. Shintaku, and F. Gao, "Frequency-adaptive network modeling for integrative simulation of natural and envelope waveforms in power systems and circuits," IEEE Trans. Circuits and Systems I: Regular Papers, vol. 53, pp. 2788-2803, 2006.

[72] P. Zhang, J. R. Marti, and H. W. Dommel, "Shifted-frequency analysis for EMTP simulation of power-system dynamics," IEEE Trans. Circuits and Systems I: Regular Papers, vol. 57, pp. 2564-2574, 2010.

[73] F. Gao and K. Strunz, "Frequency-adaptive power system modeling for multiscale simulation of transients," IEEE Trans. on Power Systems, vol. 24, pp. 561-571, 2009.

[74] H, Ye and K. Strunz, "Multi-scale and frequency-dependent modeling of electric power transmission lines," IEEE Trans. Power Delivery, vol. 33, pp. 32-41, 2018.

[75] J.A. Martinez, Power system transients: Parameter determination, CRC Press, Taylor & Francis Group, 2010.

[76] L. O. Chua and P. M. Lin, Computer-Aided Analysis of Electronic Circuits: Algorithms and Computational Techniques. Englewood Cliffs, NJ, USA: Prentice-Hall, 1975.

[77] J. Mahseredjian, S. Dennetière, L. Dubé, B. Khodabakhchian and L. Gérin-Lajoie, "On a new approach for the simulation of transients in power systems". Electric Power Systems Research, Volume 77, Issue 11, September 2007, pp. 1514-1520.

[78] A. Ametani, "A general formulation of impedance and admittance of cables," IEEE Trans. Power Apparatus and Systems, vol. PAS-99, pp. 902-910, 1980.

[79] F. Pollaczek, "Uber das feld einer unendlich langen wechselstrom durchlossenen einfachleitung," E.N.T, vol. 3, pp. 339-359, 1926.

[80] J. G. Proakis and D. G. Manolakis, Digital Signal Processing Principles, Algorithms and Applications, 4th ed. Upper Saddle River, NJ, USA: Prentice-Hall, 2007.

[81] A. J. Laub, M. T. Heath, C. C. Paige and R. C. Ward "Computation of system balancing transformations and other applications of simultaneous diagonalization algorithms," IEEE Trans. Autom. Control, vol. AC-32, no. 2, pp. 115–122, Feb. 1987.

[82] IEEE guide for the application of insulation coordination, IEEE Standard 1313.2–1999, 1999.

[83] A. Greenwood, Electrical Transients in Power Systems, 2 ed. New York, USA: Wiley, 1991.

[84] A. R. Hileman, P. R. Leblanc, and G. W. Brown, "Estimating the switching-surge performance of transmission lines," IEEE Trans. Power Apparatus and Systems, vol. PAS-89, no. 7, pp. 1455–1469, Sep. 1970.

[85] D. A. Woodford and L. M. Wedepohl, "Impact of circuit breaker prestrike on transmission line energization transients," International Conference on Power System Transients (IPST), Seattle, USA, 1997.

[86] J. A. Martinez, D. Goldsworthy and R. Horton, "Switching overvoltage measurements and simulations—Part I: Field test overvoltage measurements," IEEE Trans. Power Delivery, vol. 29, no. 6, pp. 2502-2509, 2014.

[87] C. Gary, G. Dragan and D. Critescu, "Attenuation of travelling waves caused by corona". CIGRE Report 33-13, 1978.

[88] C. Gary, A. Timotin and D. Critescu, "Prediction of surge propagation influenced by corona and skin effect". Proc. IEE, 130-A, pp. 264-272, July 1983.

[89] D. Goldsworthy, "Big Eddy - Chemawa line & source modeling data," IEEE Working Group on Field Measured Overvoltages and Their Analysis, Report, 2016.

[90] T. Ono, "Study on switching overvoltages in power systems," CRIEPI Report No. 121, Jan. 1985.

[91] K. C. Lee, "Non-linear corona models in an electromagnetic transient program," IEEE Trans. Power Apparatus and Systems, vol. PAS-102, no. 9, pp. 2936–2942, 1983.

APPENDIX A   CONSTANT PARAMETER LINE MODEL DETAILS

The CP model neglects the frequency dependence of line parameters, i.e. $\mathbf{Z}$ and $\mathbf{Y}$, and assumes a lossless line. The lumped resistances can be inserted throughout the line by dividing its total length into several sections [3]. In this thesis, the losses are modeled by dividing the line into two separate lossless lines of halved equal propagation time and distributing the total line resistance $\mathbf{R}$ [3], see Figure A.1.
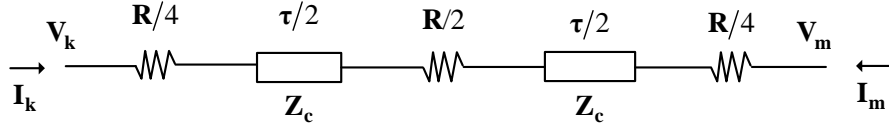

Figure A.1 Inclusion of losses in the CP line model

A.1   Single-phase line

Considering the CP model of Figure A.1 for a single-phase line, the line equations are expressed in the time domain as [3]:

$$i_k(t) = Gv_k(t) - i_{hist_k} \tag{A.1}$$

$$i_m(t) = Gv_m(t) - i_{hist_m} \tag{A.2}$$

where $G = 1/(Z_c + R/4)$, and the history current sources are given by

$$i_{hist_k} = K_1 \left[v_m(t-\tau) + K_2 i_m(t-\tau) \right] + K_3 \left[v_k(t-\tau) + K_2 i_k(t-\tau) \right] \tag{A.3}$$

$$i_{hist_m} = K_1 \left[v_k(t-\tau) + K_2 i_k(t-\tau) \right] + K_3 \left[v_m(t-\tau) + K_2 i_m(t-\tau) \right] \tag{A.4}$$

where $K_1 = Z_c/(Z_c + R/4)^2$, $K_2 = (Z_c - R/4)$, and $K_3 = (R/4)/(Z_c + R/4)^2$, and the time delay τ and characteristic impedance Z_c are give by:

$$\tau = l\sqrt{LC} \tag{A.5}$$

$$Z_c = \sqrt{L/C} \tag{A.6}$$

where l is the length of the line, and L and C are the per unit length series inductance and shunt capacitance of the line, respectively.

A.2 Multiphase line

For the multiphase case, the line equations are solved through a modal transformation, i.e. the multiphase line is transformed into a decoupled set of modal circuits. Any given mode has its own time delay and characteristic impedance. For an untransposed line there are as many distinct modes as phases. The model of (A.1) and (A.2) is now expressed in the modal domain as:

$$\mathbf{i}'_{\mathbf{k}}(t) = \mathbf{G}'\mathbf{v}'_{\mathbf{k}}(t) - \mathbf{i}'_{\mathbf{hist_k}} \tag{A.7}$$

$$\mathbf{i}'_{\mathbf{m}}(t) = \mathbf{G}'\mathbf{v}'_{\mathbf{m}}(t) - \mathbf{i}'_{\mathbf{hist_m}} \tag{A.8}$$

where primed variables denote modal quantities. Once the system of (A.7) and (A.8) is solved for every mode, the modal solution is transformed back to the phase domain. The CP model uses a real and constant transformation matrix $\mathbf{T_i}$ calculated at high frequencies. The time-domain CP model is depicted in Figure A.2, with

$$\mathbf{G_{CP}} = \mathbf{T_i}\mathbf{G}'\mathbf{T_i^t} \tag{A.9}$$

$$\mathbf{i}_{\mathbf{hist_k}} = \mathbf{T_i}\left\{\mathbf{K}'_1\left[\mathbf{v}'_{\mathbf{m}}(t-\tau') + \mathbf{K}'_2\mathbf{i}'_{\mathbf{m}}(t-\tau')\right] + \mathbf{K}'_3\left[\mathbf{v}'_{\mathbf{k}}(t-\tau') + \mathbf{K}'_2\mathbf{i}'_{\mathbf{k}}(t-\tau')\right]\right\} \tag{A.10}$$

$$\mathbf{i}_{\mathbf{hist_m}} = \mathbf{T_i}\left\{\mathbf{K}'_1\left[\mathbf{v}'_{\mathbf{k}}(t-\tau') + \mathbf{K}'_2\mathbf{i}'_{\mathbf{k}}(t-\tau')\right] + \mathbf{K}'_3\left[\mathbf{v}'_{\mathbf{m}}(t-\tau') + \mathbf{K}'_2\mathbf{i}'_{\mathbf{m}}(t-\tau')\right]\right\} \tag{A.11}$$

$$\mathbf{K}'_1 = \frac{\mathbf{Z}'_{\mathbf{c}}}{\left(\mathbf{Z}'_{\mathbf{c}} + \mathbf{R}'/4\right)^2} \tag{A.12}$$

$$\mathbf{K}'_2 = \left(\mathbf{Z}'_{\mathbf{c}} - \mathbf{R}'/4\right) \tag{A.13}$$

$$\mathbf{K}'_3 = \frac{\mathbf{R}'/4}{\left(\mathbf{Z}'_{\mathbf{c}} + \mathbf{R}'/4\right)^2} \tag{A.14}$$
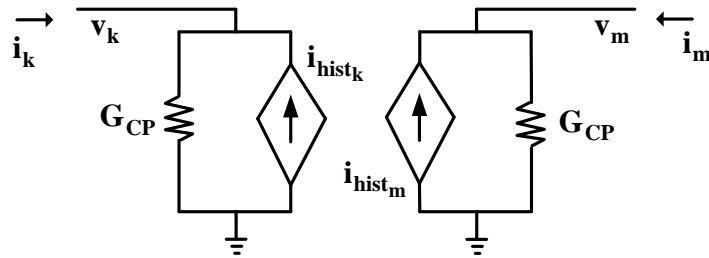

Figure A.2 CP equivalent circuit

APPENDIX B   CORONA MODEL DETAILS

B.1   Suliciu corona model

Considering that x is the radius of a cylinder on which space charge is concentrated when conductor voltage falls to zero, then for a multiphase system:

$$\mathbf{V} = \mathbf{C_0^{-1} C_x V_x} + \mathbf{C_r^{-1} Q_c} \tag{B.1}$$

$$\mathbf{Q} = \mathbf{C_0 V} + \mathbf{C_0 C_x^{-1} Q_c} \tag{B.2}$$

where $\mathbf{V}$ is the line end (or section end) voltage, $\mathbf{V_x}$ is the voltage inside the cylinder, $\mathbf{Q}$ is the total line charge, $\mathbf{C_r}$ is the capacitance of the cylinder to ground, $\mathbf{C_x}$ is the capacitance of the line conductor to cylinder boundary, $\mathbf{Q_c}$ is the corona charge inside the cylinder and $\mathbf{C_0}$ is the geometric capacitance of the line [63]. Next, the corona charge is given by:

$$\mathbf{Q_{cor}} = \mathbf{C_0 C_x^{-1} Q_c} \tag{B.3}$$

and the corona branch current is found from:

$$\mathbf{I_{cor}} = \mathbf{C_0 C_x^{-1} I_c} \tag{B.4}$$

where $\mathbf{I_c}$ is the corona current vector inside the cylinder and its members can be found from the Suliciu equation [63]:

$$i_c = \frac{d}{dt} q_c = \begin{cases} 0 & \text{if} & g_2 \leq 0 & \text{state 6} \\ g_2 & \text{if} & g_1 \leq 0 < g_2 & \text{state 2} \\ g_1 + g_2 & \text{if} & g_1 > 0 & \text{state 1} \end{cases} \Big\} V_x > 0 \\ \begin{cases} 0 & \text{if} & g_4 \geq 0 & \text{state 5} \\ g_4 & \text{if} & g_4 < 0 \leq g_3 & \text{state 4} \\ g_3 + g_4 & \text{if} & g_3 < 0 & \text{state 3} \end{cases} \Big\} V_x \leq 0 \tag{B.5}$$

$$g_j = k_j \Big[\big(c_j - c_x \big) \big(v_x - v_j \big) - q_c \Big] \quad j = 1 \cdots 4 \tag{B.6}$$

where k_j, c_j and v_j are model parameters, $c_x \in \mathbf{C_x}$, and $v_x \in \mathbf{V_x}$. The Suliciu model parameters used in this thesis are given in Table B.1. They are tuned by using the field measurements.

Negative and positive sides of the Q-V curve are taken symmetrical and phase-to-phase corona is not considered.

Table B.1 Suliciu model parameters

Sections	1 - 4				5 - 9			
Cx (pF/m)	8.4				8			
	1	2	3	4	1	2	3	4
k (Hz)	1e5	0.1	1e5	0.1	1e5	0.1	1e5	0.1
c (pF/m)	22	35	22	35	30	35	30	35
v (kV)	400	230	-400	-230	380	230	-380	-230

B.2   Linear corona model

The linear corona model used in this paper includes three linear RC parallel branches as shown in Figure B.1. The parameters are computed as follows [61]:

$$V_1 = V_{co}, \qquad V_2 = 2V_{co}, \qquad V_3 = 3V_{co} \tag{B.7}$$

where V_{co} is the corona onset voltage in kV defined by

$$V_{co} = \frac{5nr}{3C}\left[1 + \frac{2r}{s}(n-1)\sin\left(\frac{\pi}{n}\right)\right] \tag{B.8}$$

where C is the line charging capacitance in µF/km, n the number of bundles of a conductor, r the bundle radius in cm, and s the separation distance of the bundles in cm,

$$G_k = k_g\left[1 - \frac{V_{co}}{V_{co} + V_k}\right]^2 \Delta x \tag{B.9}$$

$$C_k = 2k_c\left[1 - \frac{V_{co}}{V_{co} + V_k}\right]\Delta x \tag{B.10}$$

where G_k is a linear conductance in S, C_k is a linear capacitance in F, V_k represents the DC voltage source ($k = 1,2,3$), Δx is the separation distance of the corona models in m and,

$$k_g = \sigma_g\sqrt{\frac{a}{2h}}\times 10^{-11} \tag{B.11}$$

$$k_c = \sigma_c \sqrt{\frac{a}{2h}} \times 10^{-11} \tag{B.12}$$

where a is the conductor radius in m, h is the conductor height in m, σ_g and σ_c are the corona loss constants in S/m and F/m. The corona loss constants and onset voltages used in this thesis are given in Table B.2. They are obtained by using the field measurements. Only the positive side of the Q-V curve is considered as the overvoltages in this work are on that side.

One of the drawbacks of this model is the fact that the parameters σ_g and σ_c are empirically established, and they cannot be easily applied to situations for which experimental results are not available [91]. However, it should be remarked that corona phenomena itself is highly statistical.
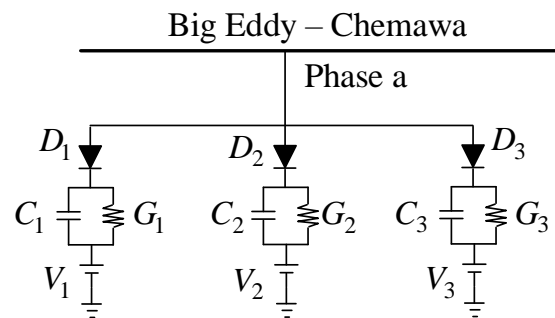

Figure B.1 Linear corona model of phase A inserted after each section

Table B.2 Linear corona model parameters

Section	V_{co} (kV)	σ_g (10^6 S/m)	σ_c (F/m)
1	405	0.13	20.6
2-4	402	0.13	23
5-9	375	0.13	33